Development of a new plasmonic transducer for the detection of biological species

Emilie Laffont

N°d'ordre NNT : 2023STET032

THÈSE de DOCTORAT
DE L'UNIVERSITÉ JEAN MONNET SAINT-ÉTIENNE

Membre de l'Université de LYON

École Doctorale N° 488
Sciences, Ingénierie, Santé

Spécialité / discipline de doctorat :
Optique, Photonique, Hyperfréquences

Soutenue publiquement le 10/10/2023, par :
Emilie Laffont

Development of a New Plasmonic Transducer for the Detection of Biological Species

---

Devant le jury composé de :

Garrelie, Florence	Professeur des universités, Laboratoire Hubert Curien, Saint-Etienne	Présidente
Charrette, Paul	Professeur des universités, University of Sherbrook, Sherbrook, Canada	Rapporteur
Livache, Thierry	Directeur de recherche EPST, CEA Grenoble, Grenoble	Rapporteur
Prakash, Ravi	Professeur des universités, Carleton University, Ottawa, Canada	Examinateur
Royer, François	Professeur des universités, Laboratoire Hubert Curien, Saint-Etienne	Examinateur
Jourlin, Yves	Professeur des universités, Laboratoire Hubert Curien, Saint-Etienne	Directeur de thèse
Berini, Pierre	Professeur des universités, Université d'Ottawa, Ottawa, Canada	Directeur de thèse
Crespo-Monteiro, Nicolas	Maître de conférences, Laboratoire Hubert Curien, Saint-Etienne	Co-encadrant de thèse

Contents

Abstract

During the COVID-19 outbreak, PCR tests were widely used for large-scale testing and screening. Yet, this technique requires bulky and time-consuming procedures to prepare the samples collected from the patients before their analysis by well-trained experts with expensive and specific equipment. PCR is therefore not competitive as a technique of detection for a widespread and rapid use in point-of-care sites. Thus, the COVID-19 pandemic highlighted the need for cheap and easy-to-implement biosensors. Surface plasmon resonance based sensors were suggested as a promising alternative in recent years. Indeed, they enable real-time and label-free detection of a wide range of analytes. That explains their widespread use in various fields of applications such as pharmacology, toxicology, food safety, and diagnosis.

This thesis proposes and demonstrates a new plasmonic configuration of detection, which can address challenges posed by point-of-care settings. The gratings used as transducers in this configuration were fabricated based on laser interference lithography combined with a nanoimprinting process. The responses of these nanostructures interrogated by a p-polarized light beam result in a transfer of energy between two diffracted orders over an angular scan. This optical phenomenon termed as "optical switch", was theoretically and experimentally investigated and optimized.

The principle of detection based on this specific configuration was demonstrated for the detection of small variations in the bulk refractive index with solutions comprised of different ratios

of de-ionized water and glycerol. A limit of detection in the range of 10^{-6} RIU was achieved. In addition, preliminary bio-assays obtained by combining this configuration with a functionalization are presented and demonstrate the selectivity and the potential of this new plasmonic configuration for biosensing applications.

This thesis work paves the way for the use of the optical switch configuration as a biosensor aligned with low-cost manufacturing and relevant for diagnosing in point-of-care sites.

Résumé

Durant la pandémie de COVID-19, les tests PCR ont été largement utilisés pour du dépistage et du suivi à grande échelle. Cependant, ces biocapteurs nécessitent de longues et complexes procédures de préparation des échantillons prélevés de patients avant leur analyse par des experts avec des technologies coûteuses et spécifiques. Les tests PCR ne sont donc pas des outils de détection appropriés à une utilisation étendue et rapide dans des centres de soins de proximité. En effet, la pandémie de COVID-19 a mis en évidence le besoin de biocapteurs peu coûteux et facile à mettre en oeuvre. Ces dernières années, les capteurs basés sur la résonance de plasmon de surface ont été suggérés comme une alternative prometteuse à ces tests. En effet, ils permettent une détection en temps réel et sans labellisation préalable d'un grand panel d'analytes. Cela explique leur utilisation répandue dans divers champs d'applications incluant la pharmacologie, la toxycologie, l'agroalimentaire et le diagnostic de maladies.

Cette thèse propose et démontre une nouvelle configuration de détection plasmonique avec le potentiel pour répondre aux défis d'une implémentation en centre de soins de proximité. Les réseaux utilisés ont été fabriqués à partir de lithographie interférentielle par laser combinée à un procédé de nanoimpression. Les réponses de ces nanostructures interrogées par un faisceau p-polarisé résultent en un transfert d'énergie entre deux ordres diffractés induit par un balayage angulaire. Ce phénomène optique qualifié de "switch optique" a été théoriquement et expérimentalement étudié et optimisé.

Résumé

Le principe de détection basé sur cette configuration spécifique a été démontrée pour la détection de petites variations d'indice de réfraction avec des solutions d'eau déionisée mélangée avec différentes concentrations de glycérol. Une limite de détection de l'ordre de 10^{-6} RIU a été atteinte. De plus, des tests préliminaires de biodétection résultant de la combinaison d'une fonctionnalisation avec la configuration de switch optique sont présentés et démontrent la sélectivité et le potentiel de cette configuration plasmonique pour des applications en biodétection.

Cette thèse ouvre la voie à l'utilisation de la configuration switch comme biocapteur approprié pour la production en masse à faible coût et du diagnostic en centre de soins de proximité.

Acronyms

16-MHA	16-mercaptohexadecanoic acid
AFM	Atomic force microscope
BSA	Bovine serum albumin
DI	De-ionized water
EDC	N-(3-Dimethylaminopropyl)-N'-ethylcarbodiimide hydrochloride
ELISA	Enzyme-linked immunosorbent assay
HSA	Human serum albumin
IPA	2-isopropanol
IR	Infrared
LIL	Laser interference lithography
LOD	Limit of detection
MZI	Mach-Zehnder interferometer
NA	Non-applicable
NHS	N-Hydroxysuccinimide
PBS	Phosphate buffer saline
PCR	Polymerase chain reaction
PDMS	Polydimethylsiloxane
PEEK	Polyetheretherketone
PETG	Polyethylene terephthalate glycol
RI	Refractive index
SAM	Self-assembled monolayer

SDS	Sulfate dodecyl sodium
SNR	Signal/noise ratio
SP	Surface plasmon
SPR	Surface plasmon resonance
UV	Ultraviolet

List of Figures

List of Tables

Chapter 1

General introduction

1.1 Context

Surface plasmons (SPs) were reported for the first time as a method of detection in 1982 by Nylander and Liedberg for gas detection [1]. Since then, their use for biosensing was demonstrated broadly by numerous applications leveraging their high sensitivity to the local environment near the interface along which they propagate [2–4] and their potential integration in point-of-care (POC) devices for real-time analysis without labelling [5–7].

In recent years, the COVID-19 pandemic demonstrated the need for fast, cost-effective and high-performance sensors to diagnose and mitigate the progression of such infections. Indeed, battling such an outbreak requires mass testing and large-scale screening, for which biosensors make a compelling case. Yet, the current devices used in the clinical and the industrial fields such as enzyme-linked immunosorbent assay (ELISA) [8, 9] and reverse-transcription polymerase chain reaction (RT-PCR) [10, 11] require cumbersome procedures, are time-consuming to use and are rather expensive. Plasmonic biosensors could be a promising alternative to these gold standards.

1.2 Enzyme-linked immunosorbent assay (ELISA)

ELISA is an approach of detection routinely used for numerous applications, such as the diagnostics of various diseases [12–14] including HIV [15] and Hepatitis B [16], the detection of allergens in food products and the control of food safety [17–19]. It is also used in toxicology to screen specific classes of drugs [20, 21].

This method of detection involves a succession of washing, separation, and incubation steps. The number and the order of these steps depend on the strategy of functionalization used during the assay. Figure 1.1 summarizes one of the most commonly used assays, termed a sandwich assay. The first step consists in the immobilization of primary antibodies (blue Y) by adsorption on the wall of microwells. These antibodies are used as biorecognition agents to selectively immobilize the targeted analyte. This step is followed by a wash to remove the antibodies not immobilized onto the surface of the wells.

Then, the physiological sample (*i.e*, blood, saliva, ...) is diluted and deposited in these wells. If this sample comprises the targeted analyte (antigen, protein) by the antibodies previously

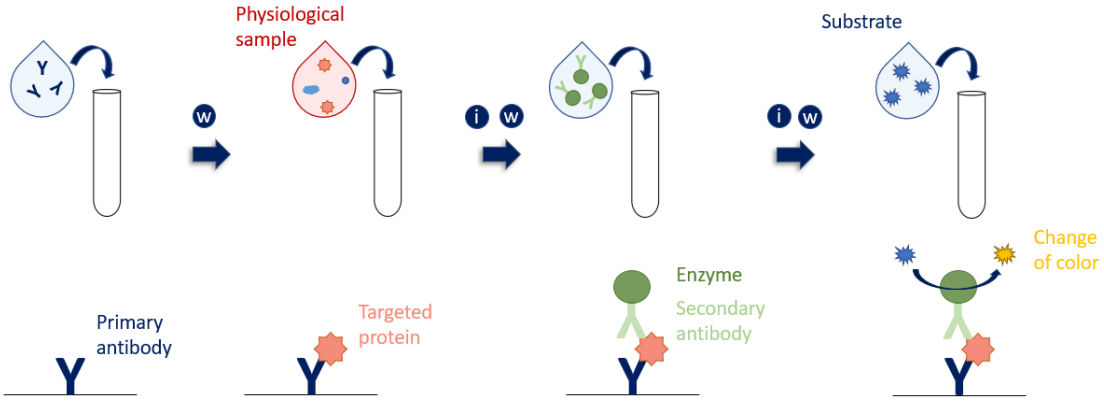

Figure 1.1: Sequential steps for a sandwich ELISA. The letters i and w stand for the incubation and the washing steps carried out after the main steps of the protocol illustrated on the sketch. The sketches are not to scale.

deposited in the wells, they selectively bind. Incubation of the sample promotes binding between the biorecognition layer and the targeted analytes. Then, the wells are washed to remove all non-bound elements. A solution comprising a secondary antibody (green Y) conjugated with an enzyme (green circles) is then deposited into the well, incubated and washed. If the physiological sample comprises the targeted antigen (now immobilised in the well) then binding also occurs with the secondary antibodies.

Finally, molecules termed as "substrates" are introduced into the wells. By reacting with the enzymes linked to the secondary antibodies, these substrates change colour, resulting in a change of colour of the solution correlated to the amount of the analyte immobilized from the physiological sample, as shown in Figures 1.2(a) and (b). Thus, the concentration of the targeted molecule immobilized on the microwell walls is quantified with a spectrometer based on the variation in the absorbance spectrum associated with the solutions in the dot at a specific wavelength, λ_A.

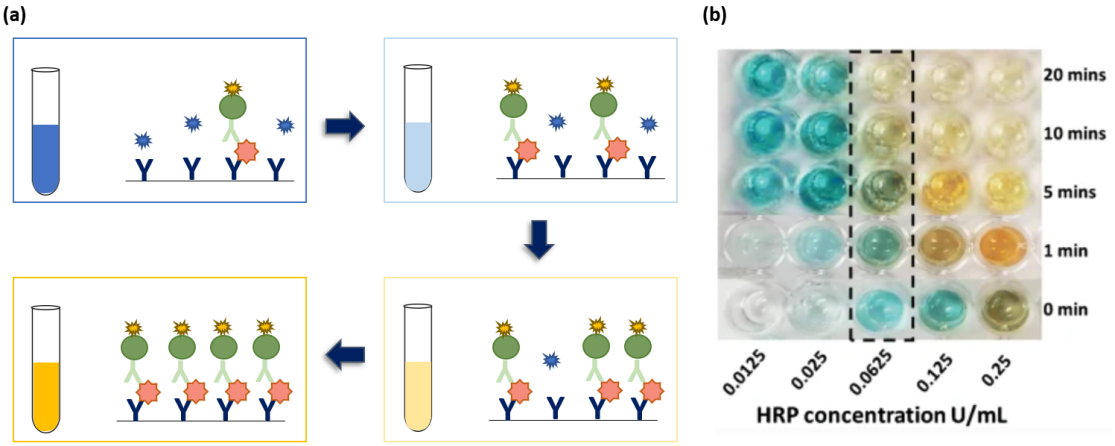

Figure 1.2: (a) Four sketches showing the correlation between the concentration of targeted analytes immobilized on the well walls and the change of coloration of the solution in the microwells. These sketches are not to scale. (b) Picture of an ELISA assay extracted from [22] showing the change of coloration observed at different reaction times depending on the concentration of the targeted analytes immobilized on the well walls. Reproduced with permission from Springer Nature, https://doi.org/10.1007/s00216-021-03359-8. Copyright © 2021, Springer-Verlag GmbH Germany, part of Springer Nature.

Figure 1.3(a) presents the measurements of absorbance at $\lambda_A = 450$ nm extracted from a study [23] consisting of a competitive ELISA assay for the detection of two different antibiotics (gentamicin and vancomycin) in protein-containing samples. These measurements were performed with low and high concentrations of each antibiotic, as sketched in Figures 1.3(b) and (c), by applying the protocol sketched in Figure 1.4.

The measurements of absorbance are represented by black circles and white squares for solutions with different concentrations of gentamicin and vancomycin. In the case of a selective detection of gentamicin, the absorbance at λ_A= 450 nm (given in Figure 1.3(a)) decreases (black circles) with the increase in the gentamicin concentration, while it remains steady (white squares) with the increase in the vancomycin concentration. That demonstrates that the biorecognition agents selectively immobilized the gentamicin. Thus, the concentration of gentamicin can be quantified based on absorbance measurements at λ_A= 450 nm with a spectrometer.

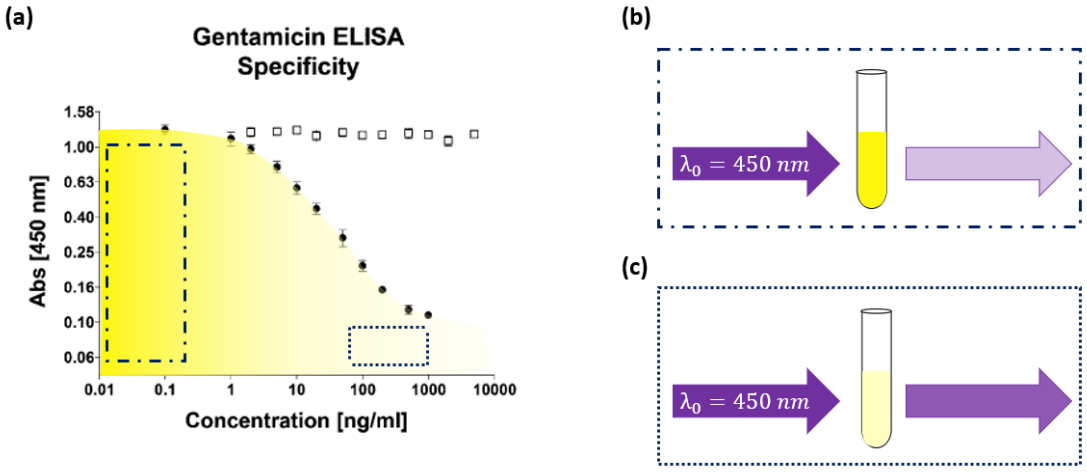

Figure 1.3: (a) Graph of the absorbance at $\lambda_A = 450$ nm depending on the ELISA's concentration of gentamicin (black circles) and vancomycin (white squares). Sketches of absorbance measurements with a spectrometer for (b) low and (c) high concentration of gentamicin. The graph presented in (a) is extracted from [23]. Reprinted in part with permission from https://doi.org/10.1186/s40064-015-1411-y. Copyright 2015 The Authors, licensed under a Creative Commons Attribution (CC BY) license. The graduated yellow background and both boxes were added to the original figure.

This approach of detection showed very high selectivity and low limit-of-detection (LOD). Indeed, LODs such as 10^{-18} moles/assay for a target protein [15], or in the range of ng/mL for the detection of antibiotic in protein-containing samples [23], or even in the range of pg/mL for the detection of a specific protein (nucleocapsid) related to the SARS-CoV-2 virus [24] were achieved with ELISA assays.

Yet, similar and enhanced performances were achieved with surface plasmon resonance (SPR) based sensors. Indeed, several studies [25–27] highlighted ELISA's drawbacks compared to SPR approaches for various applications. First, the time-consuming and cumbersome protocol of the sample preparation detailed above makes ELISA methods sensitive to the dissociation rates between target molecules and antibodies toward these molecules used to perform their detection. This issue was overcome with an SPR approach, which offers real-time measurements.

Secondly, simultaneous detection of drug and anti-drug antibodies [27] as well as multianalyte antibiotic in milk samples [28] were performed on the same SPR chips. A single ELISA kit cannot perform multisensing in the same well.

Thirdly, contrary to SPR measurements, ELISA assays require labeled secondary antibodies for the most widespread strategies of functionalization (sandwich, competitive, ...) as well as substrates to induce a change of coloration, as previously explained. This results in more expensive assays and increases the consumption of the products compared to an SPR approach.

Fourthly, ELISA measurements are based on a change of colour. The functionalization of the well walls cannot be monitored in real-time to ensure saturation of their surface or to assess non-specific binding, contrary to the SPR approach, which offers label-free and real-time measurements of biomolecular interactions from functionalization of the detection surface with biorecognition agents to the immobilization of the targeted analyte.

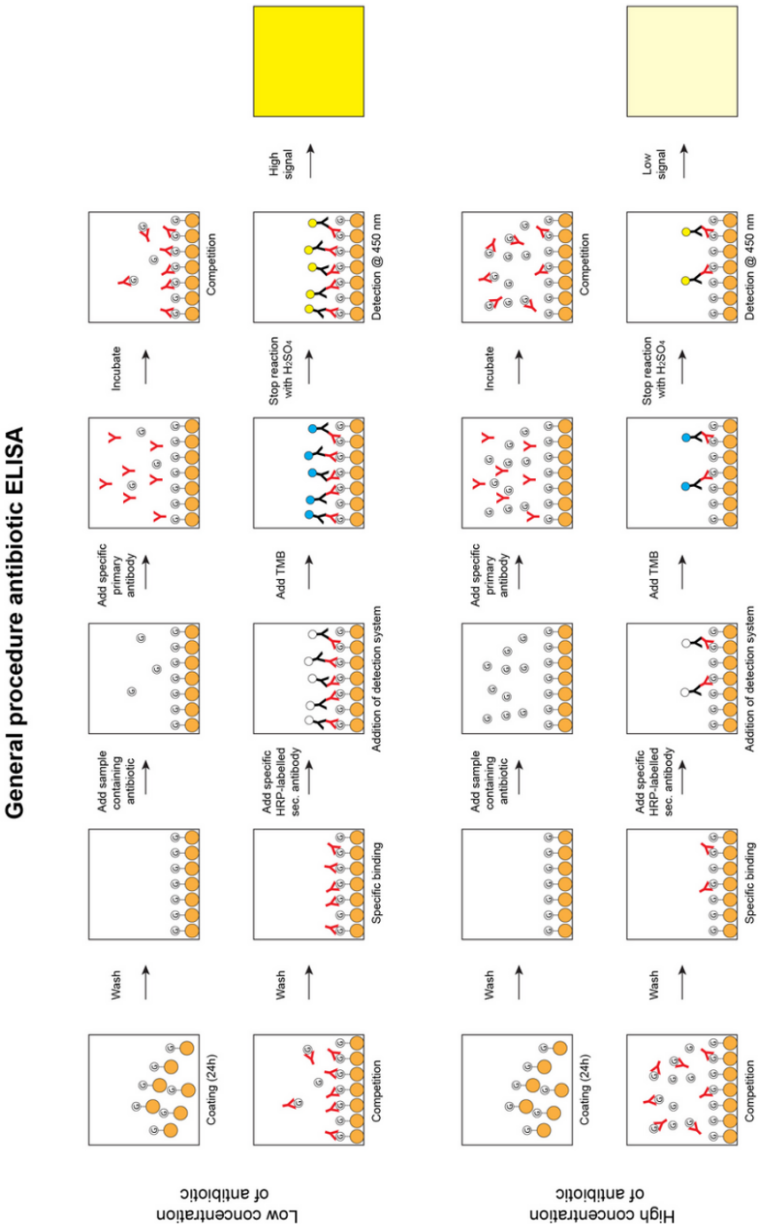

Figure 1.4: Sketches of the sequential steps for an ELISA assay consisting in detecting and quantifying gentamicin (red Y). A solution with a high gentamicin concentration results in a clearer solution than a solution with a low gentamicin concentration. That manifests through a lower (resp. higher) absorbance for high (resp. low) gentamicin concentrations, as shown in Figure 1.3. These sketches are extracted from [23]. Reprinted with permission from https://doi.org/10.1186/s40064-015-1411-y. Copyright 2015 The Authors, licensed under a Creative Commons Attribution (CC BY) license.

Fifthly, SPR chips are reusable. They are also cost-effective. Besides, functionalization is performed under dynamic conditions (circulating fluids) over the detection surface whereas in ELISA assays, the wells are washed under static conditions, which may be less efficient than inside a fluidic system such as integrated in an SPR setup.

Finally, the limited perspective of ELISA protocols for automation combined with uncertainties due to the numerous sequential steps makes it a less compelling tool for POC diagnosing.

1.3 Polymerase chain reaction (PCR) assay

Despite high performances, ELISA was shown as less competitive than SPR sensors for point of care detection in the previous section. Besides, ELISA assays were demonstrated as less accurate and sensitive than those performed with PCR tests in recent years [29–31]. PCR tests are also largely used for the diagnosis of cancer [32] and various infectious diseases [33–36], including COVID-19 [37, 38].

These tests are based on the analysis of the genetic material extracted from physiological samples collected in the nasopharynx or saliva. These samples collected by swab require several preparation steps before being analyzed, including DNA extraction and DNA amplification. Basically, the PCR detection method is based on repeated thermocycles. To summarize, the extracted DNA is first heated up to break the hydrogen bonds between both strands of DNA, as sketched in Figure 1.5 and denoted "D" in the graph of temperature presented in Figure 1.6. This step is called DNA denaturation.

After that each single DNA strand is cooled down to let a DNA probe, called a primer, specifically bind to the targeted DNA sequence of each DNA strand. This primer consists of the DNA sequence complementary to the targeted DNA sequence, bonded with a fluorophore and

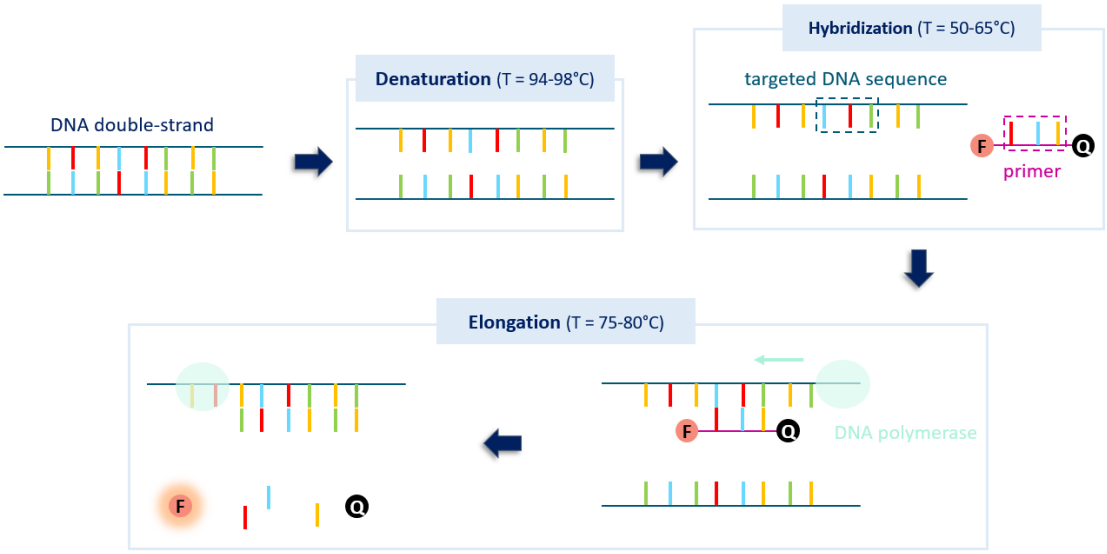

Figure 1.5: Sketches of the three main steps repeated during each thermocycle of a RT-PCR test to amplify the initial DNA material collected by swab.

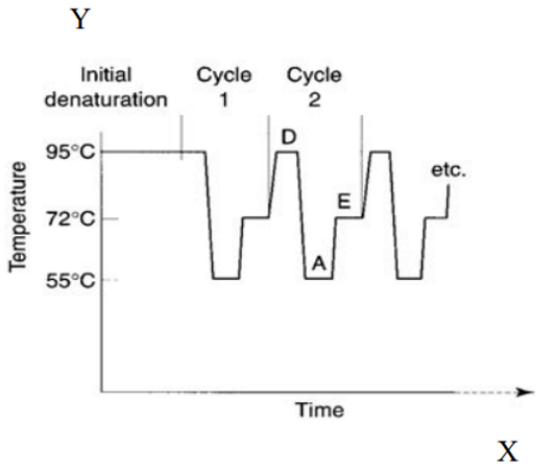

Figure 1.6: Evolution of the temperature during the repetition of each thermocycle to amplify the DNA material. This graph is extracted from [39].

a quencher (fluorophore inhibitor), as sketched in Figure 1.5. As long as the quencher and the fluorophore are close to each other, the fluorophore does not emit any fluorescence. This second step called hybridization of the primer with the DNA sequence is illustrated in Figure 1.5 and

denoted "A" in Figure 1.6.

Finally, the DNA polymerase copies each DNA single strand. It induces a fragmentation of the primer, which cleaves the fluorophore from the quencher. That results in fluorescence emission, as sketched in Figure 1.5, which is detected and measured by a spectrofluorometer. This last step called elongation is denoted "E" in Figure 1.6.

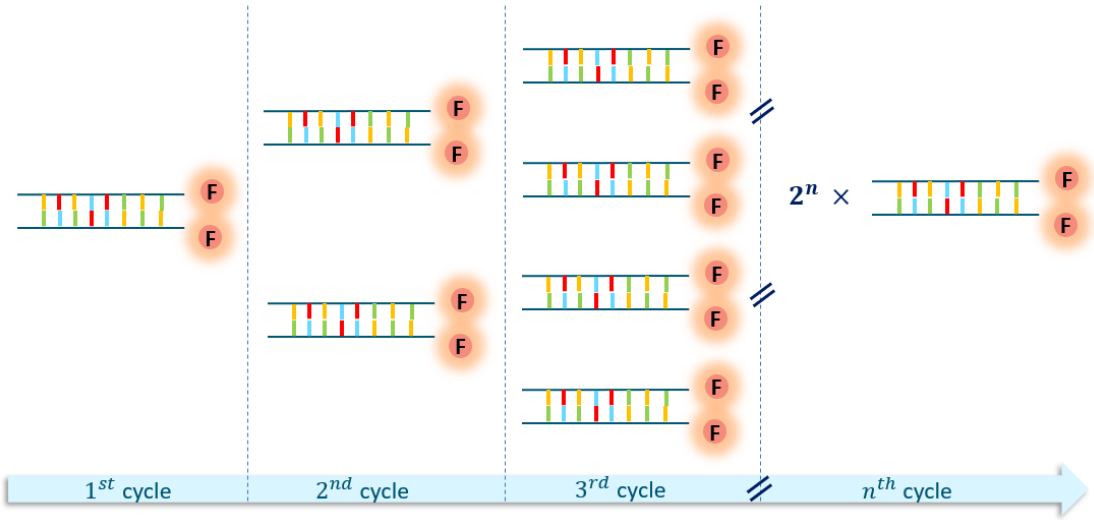

Figure 1.7: Sketch of the amplification of the DNA material and also of the fluorescence at the end of each thermocycle illustrated in Figure 1.5.

The cycle of the three sequential steps described above is repeated many times, as shown in Figure 1.6. At the end of each cycle, the amount of DNA material and of the degraded probe are doubled, as sketched in Figure 1.7. That manifests through a brighter fluorescence. Thus, if the fluorescence intensity is above (resp. under) a fixed threshold after several cycles, as shown in Figure 1.8(a) (resp. (b)), the targeted DNA sequence was (resp. not) detected.

The cycle number associated to this threshold, termed as "Ct value", depends on the dilution ratio applied to prepare the physiological sample and the targeted sequence of DNA, as

shown in Figure 1.9 in the case of the detection of SARS-CoV-2 (2019 novel Covid).

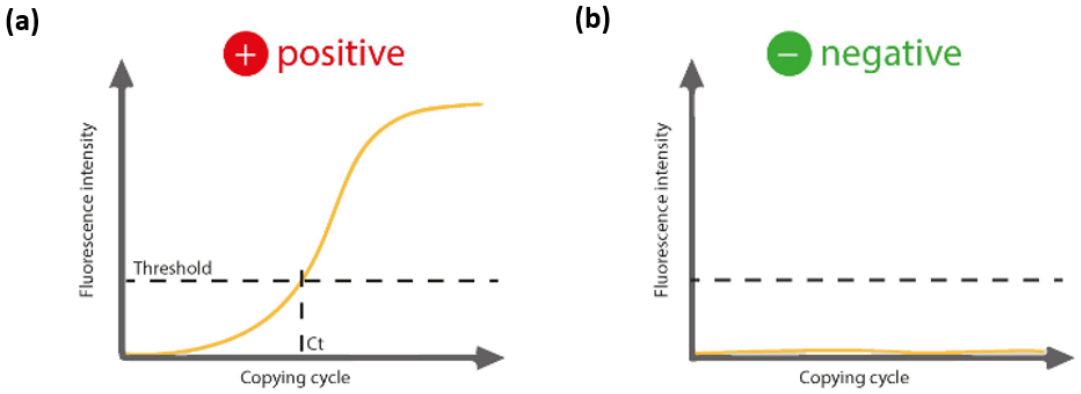

Figure 1.8: Sketches of amplification curves for (a) a positive and (b) a negative sample. These graphs are extracted from [40]. Reprinted in part with permission from https://doi.org/10.1002/cbic.202000250. Copyright 2020 The Authors, licensed under a Creative Commons Attribution (CC BY) license.

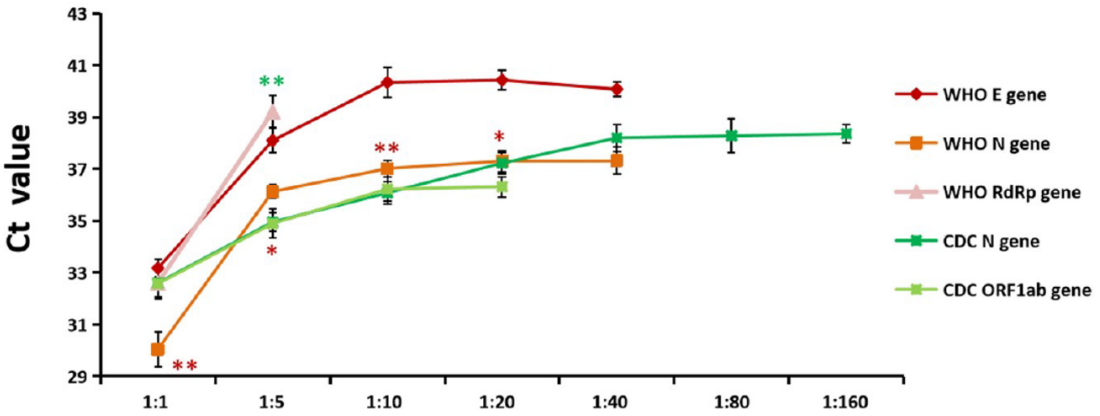

Figure 1.9: Graph representing the evolution of the threshold value, Ct, depending on the dilution ratio applied to the samples collected from the patients and the targeted gene used for the detection. This graph is extracted from [41]. Copyright 2020 The Authors, licensed under a Creative Commons Attribution (CC BY) license.

Figure 1.10 gives two sets of amplification curves performed with PCR tests and extracted from two different studies [41, 42]. Figure 1.10(a) gives the amplification curves performed for sev-

eral samples (1, 2, 3, 4) containing specific micro-RNA (non-coding RNA) sequence denoted "miR159" with different proportions (respectively 20 ng, 2 ng, 200 pg, 20 pg) and two control samples (5, 6). For the four samples containing miR159, the fluorescence signal increases, while it remains steady for both control samples. In addition, the higher the amount of miR159 in the samples, the faster the fluorescence output signal increases. Thus, detecting small amounts of genetic material in the initial samples required more thermocycle repetitions. In this manner, Figure 1.10(a) shows that amounts as little as 20 pg total RNA were successfully detected after 35 cycles of PCR.

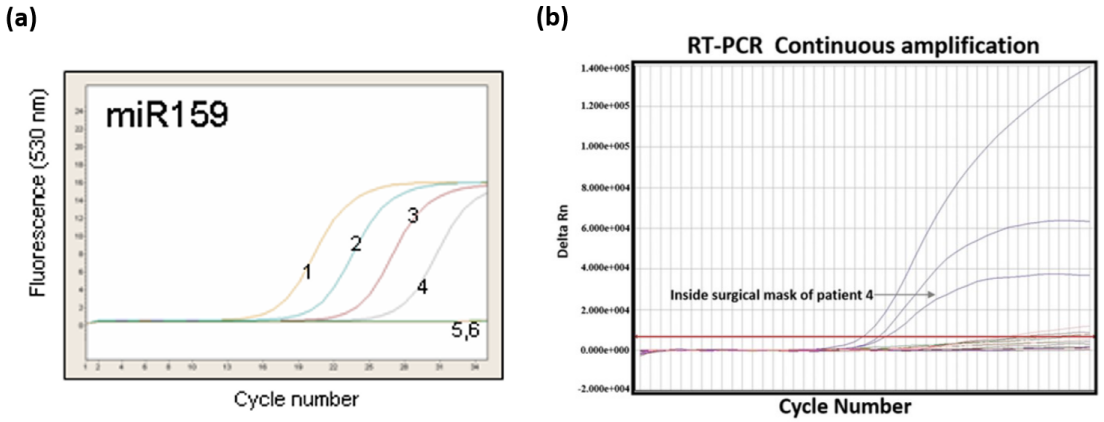

Figure 1.10: (a) Amplification curves for the detection of miR159 in four (1, 2, 3, 4) samples containing micro-RNA in different quantities (respectively 20 ng, 2 ng, 200 pg, 20 pg) and two control samples (5, 6). This graph is extracted from [42]. Reprinted in part with permission from Springer Nature, https://doi.org/10.1186/1746-4811-3-12. Copyright 2007 The Authors, licensed under a Creative Commons Attribution (CC BY) license. (b) Amplification curves for the detection of SARS-CoV-2 after 70 PCR cycles in three samples collected from patients positive to the SARS-CoV-2. The red horizontal line gives the threshold value above which the samples are considered as positive. The ordinate axis, denoted Rn (normalized reporter), represents the fluorescence emission intensity of the reporter dye (fluorophore) divided by the fluorescence emission intensity of the passive reference dye. This graph is extracted from [41]. Copyright 2020 The Authors, licensed under a Creative Commons Attribution (CC BY) license.

Figure 1.10(b) gives amplification curves performed with 70 cycles of PCR to diagnose COVID-19 from two kinds of complex (nasopharyngeal and oropharyngeal) samples collected from confirmed cases of COVID-19. These samples were directly collected from patients diagnosed as COVID-19

(curves with the highest slope on the second part of the graph) and the last one was collected from a mask, which was in direct contact with a patient positive to COVID-19. The red horizontal line represents the threshold value. After several tens of cycles, the fluorescence output signal associated to these samples increases over the threshold value. The three samples, including that collected from the mask in direct contact with a patient positive to COVID-19, were also successfully tested as positive with the PCR tests. Yet, that shows as well that several tens of cycles are required to improve the detection of low viral load.

High sensitivity and accuracy were achieved with the PCR tests for several applications. For example, a few hundred of viral RNA for the Novel SARS-Coronavirus-2 (SARS-CoV-2) copies/mL were successfully detected by PCR tests [43]. Besides, 0.5–5 pg/reaction were as well successfully detected for detection of porcine DNA [44]. The PCR tests were also worldwide performed during the COVID-19 pandemic crisis to ensure large-scale testing and screening.

Yet, several studies highlighted different issues regarding these tests [45, 46]. First, the RT-PCR tests consist of an analysis of genetic material. One of its main issues is its lack of robustness regarding the variation of viral RNA sequences [46, 47]. Indeed, during the COVID-19 pandemic, several mutations of the virus (and so its genetic material) occurred sequentially and fast. To prevent misdiagnoses, different DNA sequences were identified as less sensitive to mutation. Yet, some patients were still misdiagnosed as negative because the targeted genome of the virus causing the infection was different from the initial and also not recognized by the probe used to perform the tests.

Secondly, PCR tests require a cumbersome protocol including a pre-treatment of the samples collected before their analysis, which must be carried out by well-trained workers. In addition, the thermocyclers used to amplify the genetic material collected from patients is expensive. For these two reasons, the PCR analysis cannot be performed on POC sites. The specimens collected are also transported and tested sometimes several days afterward. This results in a variation

of the viral load in the sample which can become unrepresentative and manifests through false negatives.

To summarize, despite their high performance, ELISA and RT-PCR tests suffer from time-consuming procedures requiring expensive tools and expert users [48, 49]. These methods of detection are also not very appealing for POC settings. This motivates the development of new detection methods, including those based on surface plasmon resonance (SPR) [50, 51], described in the next section.

1.4 Lateral flow assays (LFA) and electrochemical assays

To overcome the drawbacks relative to ELISA and PCR tests, rapid biosensors were developed including lateral flow assay (LFA) [52–54] and electrochemical assay [55–57]. LFA-based detection devices are immunosensors using metallic nanoparticles functionalized with conjugated antibodies toward a specific antigen to selectively immobilize targeted antigen on a nitrocellulose membrane. They are easy to use even for self-trained users and were also largely used during the COVID-19 pandemic to test the population. Yet, these tests can be qualified as logical tests. Indeed, the response of these tests consists in a coloration change on a testing and a control lines, which are observed with a subjective perception. In addition, it suffers from a low sensitivity, which depends on the person (well-trained person or daily user), who collect the sample with swab [58, 59]. To improve this performance, fluorescent dyes (labelling) are used. Yet, that results in more expensive protocol. Moreover, that results in a limited range of physiological fluids, which can be tested and also to a limited panel of analytes. Furthermore, these tests require multiple antibodies.

Regarding the electrochemical tests, they consist in electrodes functionalized with bio-recognition agents to selectively capture targeted analytes. The biomolecular interactions (oxydo-reduction reactions) between the bio-recognition layer onto the electrode surface and the targeted analytes

are measured in real-time based on voltametric (impedimetric or amperometric) signal variations. These sensors demonstrated low LOD and high specificity [60, 61].

Finally, studies [62, 63] compared the performance (LOD and sensitivity), the cost and the operatibility of different detection approaches including LFA, electrochemical and SPR assays. It concluded that LFA was roughly easier-to-implement and more cost-effective but that it suffered from lower performance than electrochemical and SPR based sensors. Thus, LFA is not the most competitive tool of detection for early diagnosing infectious diseases such as COVID-19. Regarding electrochemical and SPR assay this same study described them as equivalent but with better LOD for SPR and better sensitivity for electrochemical sensor. Thus, SPR-based sensors appear as more relevant tools of detection for early diagnosis.

1.5 Surface plasmon resonance (SPR) sensors: a promising alternative

Among all the SPR sensors developed these last years, those based on a grating coupler were especially optimized to address the challenges of easy implementation, good portability and low-cost. Indeed, a recent study demonstrated SPR sensors achieving performances such as a sensitivity 1000-fold higher than fluorescence assays without labelling biomolecules [64]. In parallel, other works led to the development of a smartphone label-free SPR biosensor platform [65, 66] offering high potential for point-of-care applications. In addition, similar portable SPR configurations using a grating coupler were demonstrated as achieving similar performance as quantitative PCR for the same application such as the detection of micronucleic acid in a four channel multiplexing arrangement [67].

1.6 Objective and outline of the thesis

In this thesis, we propose and demonstrate a new plasmonic biosensor based on a grating coupler and operating in the "optical switch" configuration. Combined with functionalization, this detection method can address challenges in testing for disease detection, such as a low-cost and easy-to-implement detection device in POC sites. The theoretical and experimental investigations in this thesis cover the following aspects:

- The optimization of the optical switch pattern was theoretically and experimentally investigated by the study of the effect induced by different parameters such as the depth, the period and the profile of the grating.
- A fluidic system was designed and optimized to perform detection measurements under dynamic conditions.
- The optical switch configuration was experimentally demonstrated for the first time as a method of detection for small bulk refractive index (RI) variations.
- The optical switch configuration was used to perform biodetection with routinely used specific biopairs such as bovine serum albumin (BSA)/anti-BSA and human serum albumin (HSA) in clean fluids with a basic (direct) approach of functionalization.

This thesis is organized as follows:

- Chapter 2 introduces the concept of SP and describes the different conventional coupling methods to excite them. This chapter highlights the specific interest in the grating coupler in a configuration of detection using a differential measurement compared to similar existing devices of detection.
- Chapter 3 introduces the optical switch effect and gives a theoretical understanding of the principle of detection using this effect. This chapter describes the protocol of fabrication and the numerical technique used to fabricate and optimize the design of the gratings used as transducers in the optical switch configuration. The effects of the grating design on its optical switch response are investigated as well.

- Chapter 4 presents the measurements performed in the optical switch configuration. It demonstrates the optical switch as a tool of detection for small refractive index (RI) variations in the bulk (in aqueous media) and discusses the performances achieved.
- Chapter 5 presents and discusses preliminary biosensing assays performed in the optical switch configuration with specific biopairs routinely used.
- Chapter 6 summarizes the highlights and the contribution of this thesis. It also suggests future work, which could be explored based on the results presented in the previous chapters of this thesis.

These research works were carried out in cotutelle between the Laboratory Hubert Curien (UMR CNRS 5516) and the University of Ottawa. They were funded by SIS 488 doctoral school of Saint-Etienne and Labex Manutech Sleight, both included in the University of Lyon in France. Funding received from the Natural Sciences and Engineering Research Council of Canada through the University of Ottawa is also gratefully acknowledged.

Chapter 2

Introduction to surface plasmons as a method of detection

2.1 Introduction

Over the last few decades, SPR sensors were demonstrated as offering very interesting advantages such as label-free and real-time detection of a wide range of small and large molecules (proteins and cells) with high sensitivity for various sensing applications. This chapter will be devoted to SPs and their use for biosensing. First, the concept of a SP will be defined. Secondly, the first effect discovered to perform detection by using SP and termed as surface plasmon resonance (SPR) will be explained. Thirdly, the most widespread coupling methods to observe this effect will be discussed highlighting the state of the art. Fourthly, the systems of detection combining these plasmonic couplings and interferometer will be described and their interest discussed based on the literature. Finally, a focus on the conventional grating-coupler configuration will conclude this chapter with a discussion about the correlation between the grating-coupler design and its performance.

2.2 Surface plasmon (SP)

A surface plasmon is an evanescent wave propagating along a metal-dielectric interface, as sketched in Figure 2.1. This wave results from coherent collective oscillations of electrons propagating along the interface between two media with dielectric constants of opposite signs. The amplitude of this wave decays exponentially on each side of this interface. This attenuation

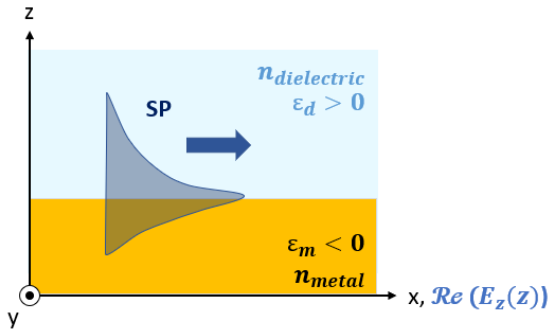

Figure 2.1: SP (dark blue shape and arrow) propagating along a metal-dielectric interface.

and so the penetration depth of a SP depend on the media on each side of the interface as demonstrated in [68]. Likewise, the wave vector, β_{SP}, and the propagation distance, L_x, of a SP depend on the dielectric constants of the metal, ϵ_m, and the dielectric, ϵ_d. Both parameters are respectively defined by the expressions below, given in [68] and [69]:

$$\beta_{SP} = \frac{2\pi}{\lambda} \cdot \sqrt{\frac{\epsilon_m \cdot n_d}{\epsilon_m + n_d}} \tag{2.1}$$

$$L_x = \frac{\lambda}{2\pi} \cdot \frac{Re(\epsilon_m)^2}{Im(\epsilon_m)} \left(\frac{Re(\epsilon_m) + \epsilon_d}{Re(\epsilon_m) \cdot \epsilon_d} \right)^{\frac{3}{2}} \tag{2.2}$$

where λ denotes the wavelength of the light source used to excite the SP, and n_d is the refractive index (RI) of the dielectric. The dielectric constants ϵ_m and ϵ_d are related to the RI of each medium according to the relation below:

$$\epsilon_i = (n_i)^2 \tag{2.3}$$

where ϵ_i represents the dielectric constant of a medium i and n_i is the RI of this medium.

Consequently, if the RI of the dielectric medium locally changes near the interface, it induces a variation in the propagation constant associated with the SP and therefore, a modification of the conditions required to reach the SPR, which is described in the next section.

2.2.1 Surface plasmon resonance (SPR)

The surface plasmon resonance (SPR) was observed for the first time in 1902 by Wood, who noticed anomalies in the reflectivity spectra of diffraction gratings [70]. In 1983, Liedberg demonstrated the potential of this effect for biosensing [71]. Since then, SPR proved to be an efficient tool of investigation regarding tiny variations of RI in sensing media near a metal-dielectric interface.

This effect consists of a transfer of energy from the incident light beam interacting with a metallic surface to a plasmonic mode. It occurs when their respective propagation constants are equal under a specific angle of incidence and wavelength. That results in the excitation of a SP. The relation describing this equality depends on the chosen coupling method, which will be described in the next sections. Figure 2.2(a) gives the dispersion relation in the case of a grating-coupler configuration.

The most common way to observe this effect consists in obtaining the intensity response of an order reflected by the grating over an angular or spectral range. The spectrum of this Fresnel reflection, as well called 0^{th} order, presents a resonance dip for a specific couple of wavelength and incident angle of the p-polarized impinging beam, as shown in Figure 2.2(b). As explained in the previous section, the SP parameters (especially its propagation constant) are sensitive to the environment around the metal-dielectric interface, along which it propagates. Therefore, a local variation in the RI of the dielectric sensing medium near the interface due to binding events or the injection of a new solution with a RI different from the previous one inside the

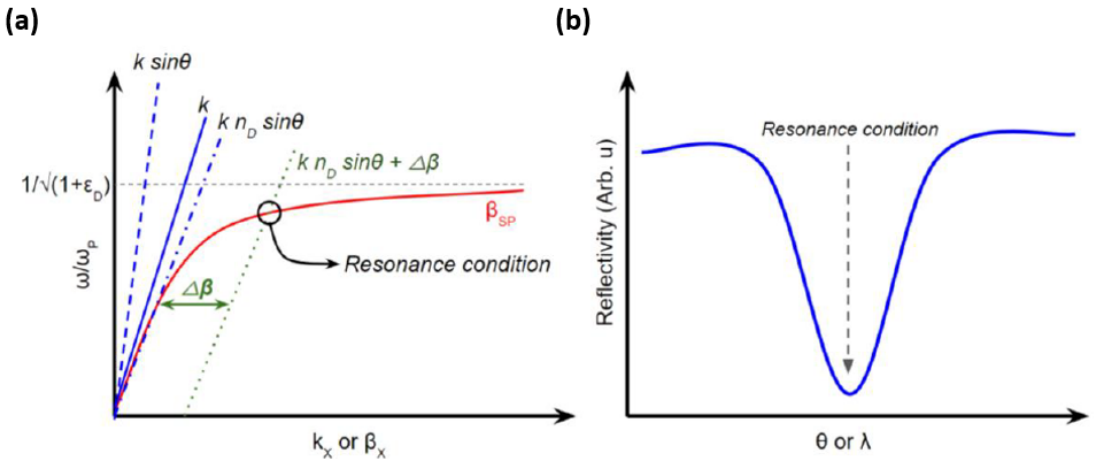

Figure 2.2: (a) Dispersion curve of the SP in the case of a grating coupler and (b) resonant dip in the reflectivity spectrum due to the phase matching between the incident light beam and the SP. Both Figures are extracted from [72]. Reprinted with permission from MDPI, https://doi.org/10.3390/bios8030080. Copyright 2018 The Authors, licensed under a Creative Commons Attribution (CC BY) license.

fluidic device induces a change in the propagation constant of the SP. Thus, under the initial incident wavelength and angle (λ_i, θ_w), the SPR conditions are no longer fulfilled, since the equality between the propagation constants respectively associated with the incoming light, k_x, and the plasmonic mode (eq. 2.1) is no longer fulfilled. Another couple of wavelength and angle of incidence (λ_i, θ_{w+g}) is associated with the new configuration, as illustrated in Figure 2.3. In the case of biosensing applications, this shift in the angle (resp. wavelength, depending on the chosen method of interrogation) of resonance is exploited to assess the RI variations along the metal-dielectric interface.

To assess the performance of SPR detection device, different criteria, such as the sensitivity and the LOD are used. The sensitivity, S, represents the partial derivative of the output signal (shift in the resonance angle or wavelength), res, depending on the variation of measurand (RI or concentration of analytes), a. It is defined by the relation below:

$$S = \frac{\partial res}{\partial a} \tag{2.4}$$

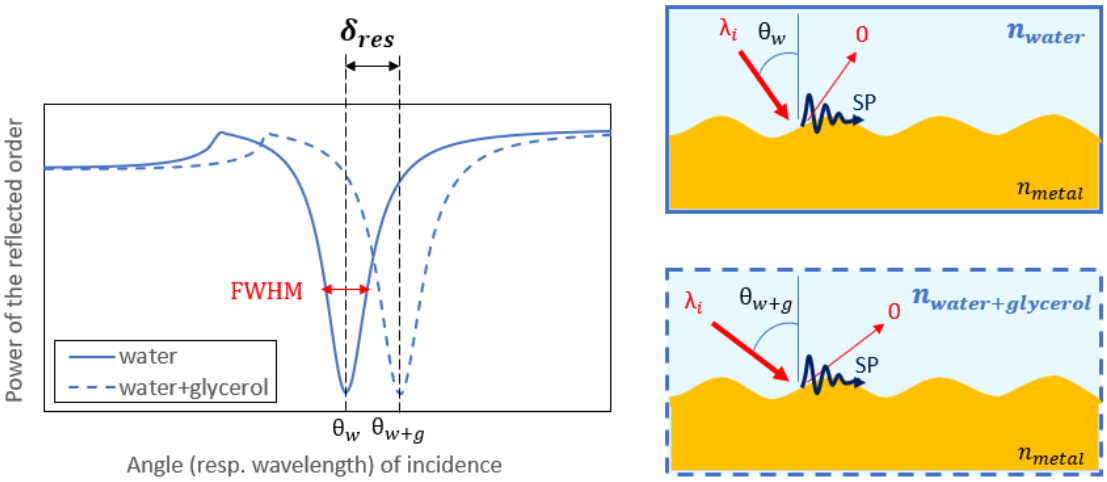

Figure 2.3: Shift in the resonance angle, δ_{res}, due to a change of sensing medium with a different RI at the interface along which the SP propagates.

Likewise, the LOD corresponds to the lowest variation of measurand that a sensor can detect. Assuming that the minimum signal/noise ratio (SNR) required for reliable detection would be equal to 2, the LOD is described by the relation below:

$$LOD = \frac{2 \cdot \sigma}{S} \tag{2.5}$$

where σ is the resolution of the measurement system, *i.e.*, the resolution of the goniometer (resp. spectrometer) in the case of an angular (resp. spectral) interrogation.

The Figure-of-Merit (FOM) is also commonly used to assess the performance of the SPR detection devices. It is defined as the ratio between the shift in the resonance angle (resp. wavelength) and the full width at half minimum (FWHM) associated to the resonant dip. The FOM identifies the best trade-off between an enhancement of the sensitivity and the LOD. Yet, this criterium is not applicable for the detection based on the optical switch developed in this thesis. To draw a relevant parallel between the classical SPR coupling and the detection based on the optical switch, we will focus on the LOD for the rest of this manuscript.

2.2.2 Coupling method

Different plasmonic configurations were developed for biosensing. In this subsection, we will present the most common of them. The first two leverage the SPR effect described in the previous subsection. They are differentiated from each other by their coupler: a prism and a grating. The last conventional coupling method discussed uses a waveguide as coupler and can be based on two different effects (including SPR) depending on the design of the coupler. It will be discussed in the last part of this subsection.

For each of them different interrogations can be used. But we will only focus on the two most commonly used: spectral and angular interrogation. Likewise, only intensity analysis will be considered for two reasons. First, it is the most commonly used approach in conventional SPR sensors. Secondly, it is the approach used with the optical switch configuration described in chapter 3. However, interrogation based on phase or polarisation has also been discussed in the literature [73, 74].

Kretschmann-Raether configuration

Kretschmann and Raether were the first to propose a coupling method to excite the SP in 1968 [75]. Nowadays, this configuration of optical sensing is certainly the most widespread using SPR. It consists in a prism with a base covered by a thin metal layer, where the prism has a higher RI than that associated with the dielectric medium on the outer boundary of the metallic layer, as illustrated in Figure 2.4(a). Under a specific couple of wavelength and incident angle, matching is achieved between the wave vector of the plasmonic mode and that of the incident beam, k_x, described by the expression below.

$$k_x = \frac{2\pi}{\lambda} \cdot n_p \cdot sin\theta \tag{2.6}$$

In this expression, n_p represents the RI of the prism and θ stands for the angle of the incident beam, which is larger than the critical angle to obtain a total reflection of the incoming beam

at the prism-metal interface. The equality between the expressions (2.1) and (2.6) results in the excitation of the plasmonic mode.

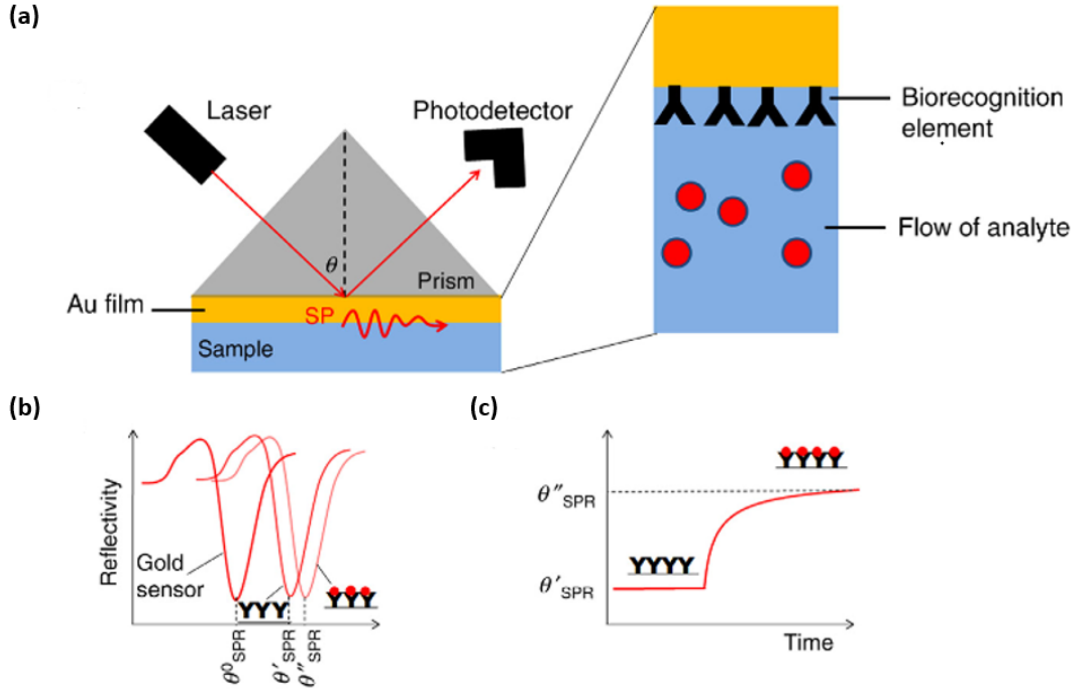

Figure 2.4: (a) Sketch of Kretschmann configuration setup comprising a prism with a RI n_p and its base covered with a thin film of gold. The photodetector allows to monitor the intensity of the reflected order, which achieves a minimum at the resonance angle denoted θ^0_{SPR} before functionalizing the surface and considering the sample represented in blue as the reference medium. (b) Shift in the resonance angle to the right at $\theta^{'}_{SPR}$ after the immobilization of the biorecognition elements and at $\theta^{''}_{SPR}$ after the binding events between these biorecognition agents and the analytes. (c) The sensorgram illustrates the shift in the resonance angle due to interactions between the biorecognition elements and analytes in real-time. These figures are extracted from the article [76] from Miyazaki *et al.*. Reprinted with permission from Elsevier, https://doi.org/10.1016/B978-0-323-49778-7.00006-0. Copyright © 2017 Elsevier Inc.

Thus, if the initial dielectric medium is replaced by another with a different RI or if some binding events occur at the metallic-dielectric interface along which the SP propagates, the reflection of the incident light beam is no longer attenuated at the prism-metal interface at the initial resonance angle (resp. wavelength, depending on the chosen interrogation method). Indeed, the

drop in intensity associated with the Fresnel reflection is shifted to a new incident angle (resp. wavelength), as shown in Figure 2.4 (b)-(c). Based on this angular (resp. wavelength) shift, the variation of RI or the amount of biomolecules immobilized on the metal layer can be quantified.

Biosensors based on Kretschmann-Raether configuration have been successfully commercialised. It was largely used to lead various studies such as drug discovery, assessment of kinetics for a wide range of analytes, measurement of specific interactions, and diagnosing diseases by the detection and quantification of biomolecules in physiological fluids [77, 78].

Figures 2.5(a) and (b) gives two sets of reflectivity spectra obtained at two different wavelength (670 nm and 785 nm) in a Kretschmann configuration. Each set of spectra shows a shift in the resonant angle while the concentration of glucose in the tested samples increases. That is due to the variations of RI induced by the different concentrations of glucose at the metal (gold) and sensing medium interface, which implies a change in the phase matching between the incident beam interrogated the metal film and the SP to reach the resonance condition. Based on these SPR responses, the sensorgrams given in Figure 2.6 were observed. A LOD of 4 mmol/L was successfully achieved. This value would be low enough for the diagnosis of normal, pre-diabetic and diabetic patients.

This configuration provides theoretically better resolution [68] and sensitivity [80] than a configuration using a grating coupler (described in the next section) as a transducer in the case of a wavelength interrogation. But in the case of an angular interrogation, this performance is rather similar between both coupling approaches.

LOD in the range of 10^{-5}-10^{-6} RIU were achieved with a basic thin gold layer on the top of the prism base [81, 82]. These performances were enhanced by different approaches such as adding a supplementary dielectric layer [83], using long-range SPR, combining a metallic nanostructure on the base of the prism, or opting for a phase interrogation instead of an angular

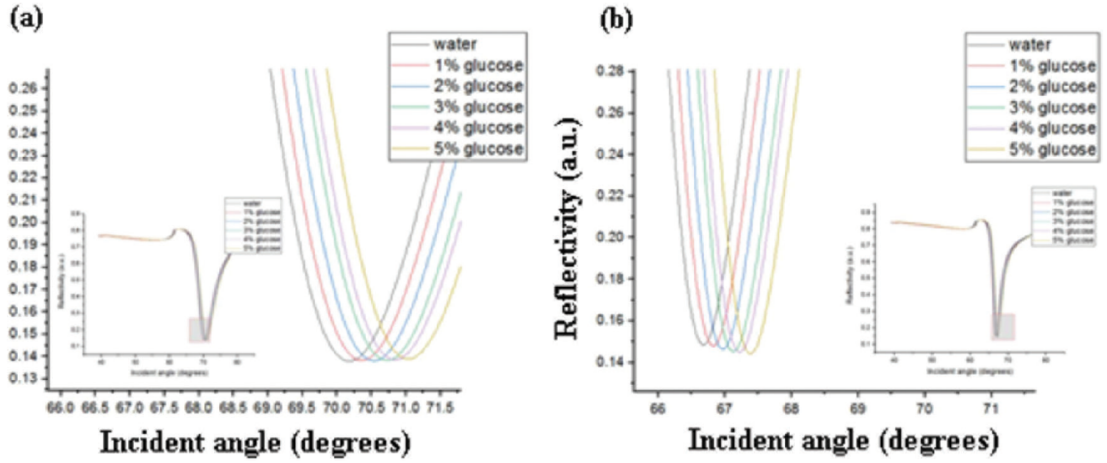

Figure 2.5: SPR responses in the Kretschmann's configuration to variations of glucose concentrations at an incident wavelength, λ_0, equal to (a) 670 nm and (b) 785 nm. These graphs are extracted from [79]. http://dx.doi.org/10.17576/jsm-2019-4806-13.

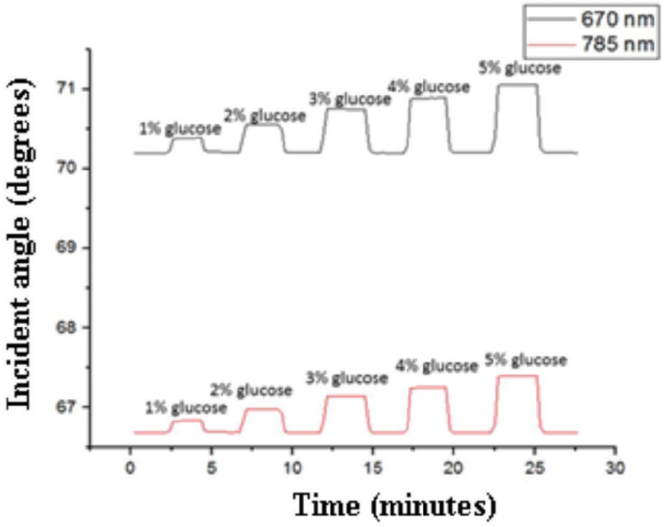

Figure 2.6: Sensorgram measured in real-time for the sequential injection of buffer (distilled water) and buffer doped with different concentrations of glucose. This graph is extracted from [79].

or wavelength one, as summarized in [69], to reach LOD in the range of 10^{-7} RIU. Yet, these approaches require more complex procedures of fabrication and are therefore expensive.

In addition, Kretschmann-Raether's configuration presents inconveniences such as a bulky arrangement hard to integrate into a fluidic system setup, which limits its miniaturization prospects. Besides, this detection method based on SPR does not permit a differential measurement to cancel some perturbations, except if the setup is turned into an interferometer [84] (as discussed in section 2.3), and so is more complex.

To summarize, despite its high performance, the most basic Kretschmann-Raether configuration suffers from a cumbersome arrangement due to its prism, which does not make it the most compelling case for POC settings. That is why other configurations, like that presented in the next part of this subsection, have been elaborated.

Grating coupler configuration

A broad variety of plasmonic sensors using nanostructures as transducers was demonstrated as highly promising devices of detection [6]. They consist of a coupling of a p-polarized incident beam with a SP by the -1^{st} or $+1^{st}$ diffracted order of a waveguide resonant grating, which corresponds to a nano- or microstructure coated with a thin metallic layer (the waveguide) [85]. Similarly to Kretschmann-Raether's configuration, this coupling manifests through a large and deep resonance dip in the reflectivity spectrum of the 0^{th} order, as shown in Figure 2.7(a) considering the configuration sketched in Figure 2.7(b). This dip results from a perfect synchronism respectively described for the -1^{st} and $+1^{st}$ diffracted order couplings by the equalities below:

$$k_0 \cdot sin(\theta) + k_0 \cdot n_e = K_g \tag{2.7}$$

$$k_0 \cdot sin(\theta) + K_g = k_0 \cdot n_e \tag{2.8}$$

In these relations, k_0 represents the wavevector of the incident beam, θ denotes its angle of incidence, K_g stands for the grating vector and n_e is the effective RI of the SP.

The relation (2.7) describes the contradirectional coupling via the -1^{st} order, while the equality

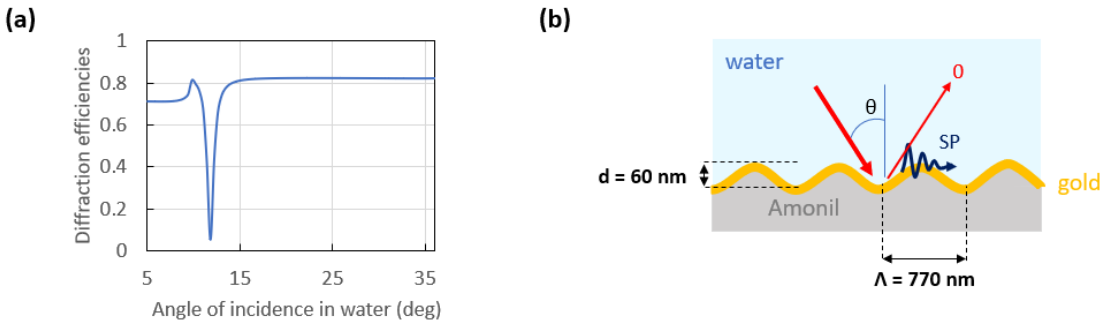

Figure 2.7: (a) SPR response computed via the software MC Grating of a sinusoidal grating probed with a p-polarized light beam at free-space wavelength λ_0=850 nm in the configuration sketched in (b). The diffraction of efficiency is defined as the ratio between the power of the reflected order and that of the incident beam interacting with the grating. (b) Sketch of a coupling configuration between an incident p-polarized light beam at free-space wavelength λ_0=850 nm and a sinusoidal grating coated with a 100 nm thick gold layer.

(2.8) describes the codirectional one via the $+1^{st}$ order. Both of them are respectively sketched by the half Ewalds'circles in Figures 2.8(a) and (b).

When one of these relations is fulfilled, the SP is excited by a partial absorption of the incident wave energy. It triggers its propagation on a few or tens microns depending on the metal of the grating. This absorption is induced by Joules effects on the collective oscillations of the electrons on the metal surface.

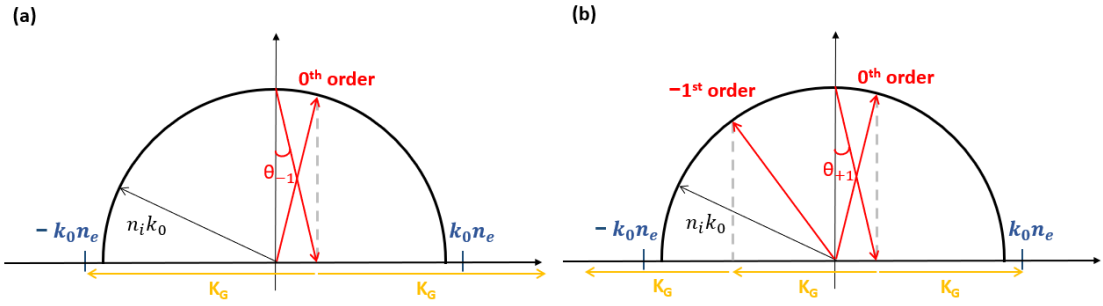

Figure 2.8: Half Ewald's circles showing the plasmon coupling via (a) the -1^{st} and (b) the $+1^{st}$ orders.

To make a choice between these configurations of synchronous coupling, two criteria must be taken into account. The first is the spectral (resp. angular depending on the chosen interrogation method) shift in the resonance dip under the effect of the RI change in the sensing medium in the vicinity of the metal layer. The second is the ambient optical noise that propagative diffraction orders different from that used to excite the plasmonic mode can generate.

Figure 2.9(a) illustrates the resonant wavelength shift in the reflectivity spectrum under a RI variation from 1.00 to 1.01 in the sensing medium by considering the interaction between a p-polarized incident beam and the sinusoidal gratings sketched in Figure 2.9(b) and (c), corresponding to both possible synchronous couplings. The resonant wavelength shift is similar for the co- and contradirectional couplings. Consequently, the wavelength sensitivity is rather identical between both coupling configurations. In this case, the first criterion does not lead to prefer one

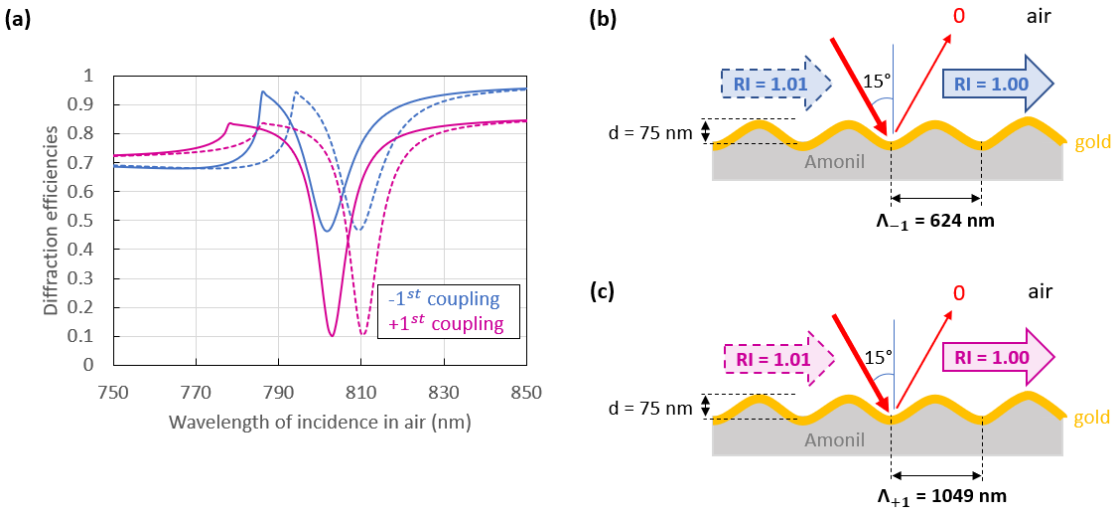

Figure 2.9: (a) Shift in the resonance wavelength due to an increase in the sensing medium RI of 0.01 RIU, considering the interaction between an incident p-polarized beam at 15° and the grating coated with a 100 nm thickness gold layer sketched in (b) and (c) initially in air. The solid curves are associated with the 0^{th} order spectra with air as the sensing medium, while the dashed correspond to the 0^{th} order spectra after an increase in the sensing medium RI of 0.01 RIU. The blue and pink curves are respectively associated with the -1^{st} and the $+1^{st}$ order coupling.

specific coupling order.

Figure 2.10 shows the diffraction efficiency of the 0^{th} order (green) *vs.* the period Λ of the grating sketched in Figure 2.9(b) with air as sensing medium. Diffraction efficiencies are defined by MC-Grating sofware website [86] as "complex amplitude and power of all reflected and transmitted diffraction waves" (orders). It corresponds to the ratio between the power associated with each order i and the initial power in the probing beam interrogating the grating surface.The deepest resonance dip is associated with the codirectional coupling via the $+1^{st}$ order with a 1049 nm period grating. Yet, coupling via the $+1^{st}$ order involves a propagative -1^{st} diffraction order (orange curve). Thus, under perfect synchronism conditions for the codirectional coupling, the higher the energy associated with the -1^{st} reflected order is, the less deep the resonance dip in the reflectivity spectrum of the 0^{th} order.

In this specific case, there is no strong reason to prefer coupling via the $+1^{st}$ order compared to coupling via the -1^{st} order. However, the considerations herein above are only illustrative and not general. Indeed, a depth change, a profile modification of the grating or a conical incidence can change the conclusions previously mentioned.

Like Kretschmann's configuration, this method of detection is based on the measurement of the shift in the resonance wavelength (resp. angle) in the reflectivity spectrum of the Fresnel reflection depending on the RI variation onto the grating surface, or the biological species immobilization on this same surface.

However, the coupling is obtained with specific parameters of the grating such as its period and its depth in this SPR-based configuration of detection. Besides, it was demonstrated that the shape of the grating profile had a non-negligible effect on the optical responses of the gratings [87–89] as well as the roughness associated with these profiles [90, 91]. The correlation between the performances and the main design parameters of the gratings used in this configuration will

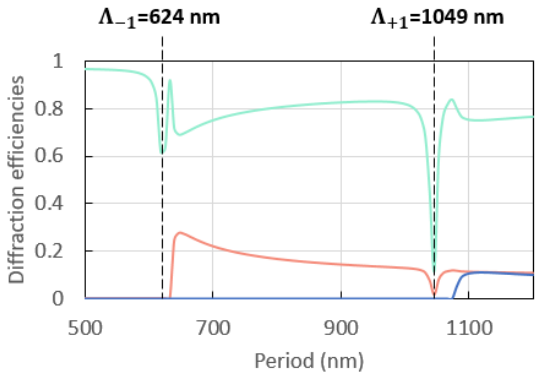

Figure 2.10: Diffraction efficiency *vs.* the period resulting from the interaction between an incident p-polarized beam at 15° and free-space wavelength $\lambda_0 = 800$ nm with a sinusoidal 75 nm-depth grating covered of a 100 nm-thick gold layer in air. The grating vector is respectively equal to $\frac{1}{\Lambda_{-1}}$ and $\frac{1}{\Lambda_{+1}}$ in the case of the $+1^{st}$ and the -1^{st} order couplings. The diffraction efficiencies of the -1^{st}, 0^{th} and $+1^{st}$ orders are respectively represented by the orange, green and blue curves.

be discussed in section 2.4.

Depending on their interrogation method and the illuminated side of the grating, the SPR sensors operating in this configuration achieve LODs in the range of 10^{-4}-10^{-7} RIU [92–94]. Some of them offer portability and multichannel operation, which make them attractive for the simultaneous detection of different analytes and POC applications.

The main advantage of the grating coupler based configuration is the tunability that it offers thanks to the different parameters involved in the coupling between the plasmonic mode and the incident light beam. Moreover, such devices are more portable, miniaturizable and easy-to-integrate into fluidic systems.

Waveguide-coupler configuration

Another configuration appealing for its high degree of miniaturization is based on waveguide-coupler. Different designs exist with this configuration. One of the most used comprises a high RI

material (waveguide) embedded in a lower RI material (substrate) in order to get total internal reflection (TIR), as sketched in Figure 2.11. A portion of the lowest RI material is removed and cladded by a thin metal layer. This part of the waveguide is immersed in the sensing medium. When light passes through the waveguide under phase matching conditions between the guided mode propagation constant, β_{mode}, and that of the SP, β_{SP}, described by the relation below, a part of the light beam propagating inside the waveguide interacts with the metal layer and excites a SP, which propagates along the metal-sensing medium interface:

$$\beta_{mode} = Re(\beta_{SP}) \tag{2.9}$$

This manifests through an attenuation of the transmitted output power at a specific wavelength, which depends on the uppercladding and/or the receptor-analyte adlayer changes on the detection surface. Thus, the biomolecular interactions between the biorecognition receptors and the targeted analytes can be quantified by a shift in resonance wavelength at which the transmitted output power from the waveguide is the most attenuated. Indeed, unlike the prism- and the grating-couplers previously described, the plasmon-waveguide resonance method cannot be based on an angular scan but only on a spectral scan. Although an amplitude modulation approach can be used [95, 96], it will not be discussed here.

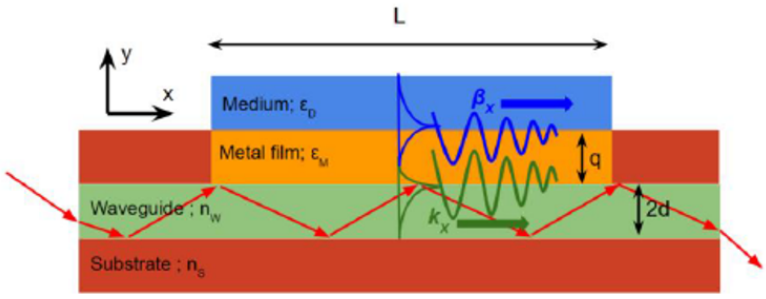

Figure 2.11: Sketch of the waveguide-coupling configuration, where the incident beam excites the SP when their propagation constants, β_x and k_x, are equal. This sketch was extracted from the article [72]. Reprinted with permission from MDPI, https://doi.org/10.3390/bios8030080. Copyright 2018 The Authors, licensed under a Creative Commons Attribution (CC BY) license.

LODs in the range of 10^{-4}-10^{-5} RIU [97, 98] were achieved with different designs using this configuration. Yet, these performances were enhanced and reached LODs in the range of 10^{-6} RIU by several improvements, including the use of polarization maintainers [99] and a bimetallic approach combined with a prism to inject the incident light beam [100].

Another design consists in a metal stripe along which incident light beam propagates. Figure 2.12(a) shows this configuration for detection based on a waveguide called the single-interface metal–dielectric waveguide. Like the previous design discussed, the biomolecular interactions on the surface of the metal film (adlayer) decrease the transmitted output power. Yet, in order to gain in sensitivity, two symmetrical designs called metal-insulator-metal (MIM) waveguide and insulator-metal-insulator (IMI) waveguide, respectively sketched in Figures 2.12(b) and (c), were elaborated. In the case of the MIM design, the SPs are very confined. Consequently, the

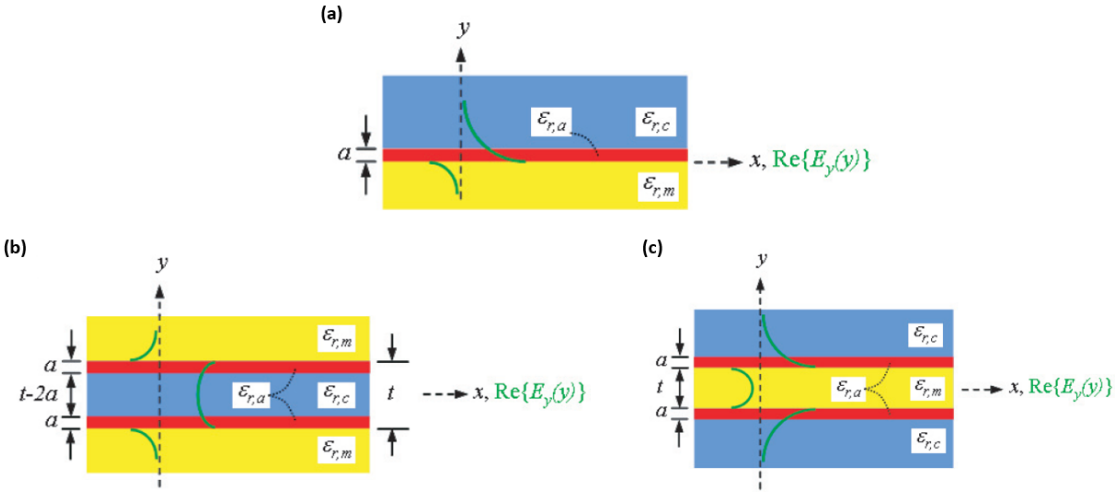

Figure 2.12: Sketches of 1D surface plasmon waveguide structures based on (a) a single interface metal-dielectric waveguide, (b) a MIM waveguide, and (c) a IMI waveguide. The metal layers with a relative permittivity $\epsilon_{r,m}$ are represented in yellow, and the dielectric media with a relative permittivity $\epsilon_{r,c}$ in blue. The dielectric adlayers with a thickness a and a relative permittivity $\epsilon_{r,a}$ are coloured in red. The real part of the main transverse electric field component (Re{Ey}) of the mode of interest is sketched in green on all structures. These figures are extracted from the article [101]. Reprinted with permission from IOP Journal, doi:10.1088/1367-2630/10/10/105010. Copyright 2015 The Authors, licensed under a Creative Commons Attribution (CC BY) license.

attenuation in the transmitted output power is very high. On the contrary, the SPs propagate along a long distance and are only slightly attenuated in the case of the IMI design, but the SPs are less confined.

The approach is no longer based on SPR for such detection configurations. Indeed, the MIM design supports short-range SP, while the IMI design supports long-range SP. The propagation of such specific SPs relies on the symmetry of the environment around the medium through which they propagate. Thus, in the case of a perfectly symmetrical environment, the transmitted output power is maximal. That is why the biomolecular interactions between the biorecognition layer and the analytes in the physiological fluid injected induce a decrease in the intensity of the transmitted output power, which enables the quantification of the binding events between the receptor and the analytes.

LODs in the range of 10^{-6}-10^{-8} RIU were simulated with MIM waveguides [102, 103] and reached experimentally with IMI designs [104, 105].

Optical fibers have also been used for coupling to SPs, and with the addition of polarization maintainers, their performance becomes less deformation-sensitive. This makes this configuration compelling for remote detection, especially in environments hard to reach and for in-vivo experiments [106–108].

Generally, detection based on waveguide-coupled schemes benefit from a high degree of miniaturization, and could be easily arrayed. These attributes are very appealing for POC applications and multianalyte detection. The main drawback of such a method is the measurements sensitivity to the alignment of the incident beam with the waveguide.

2.3 Plasmonic Mach-Zehnder interferometer (MZI)

All the configurations described in subsection 2.2.2 monitor a single signal: the power of the 0^{th} order or the power of the output beam propagating through a waveguide. It is also hard to discriminate between the noise due to perturbations such as mechanical vibrations or variations in the intensity of the light source and the signal due to binding events or a change of RI over the detection surface. To overcome this issue, new configurations monitoring simultaneously at least two signals or a single signal resulting from the interference of two signals were developed. The plasmonic Mach-Zehnder (MZI) sensor is considered as one of the highest-performing plasmonic interferometers. This interferometry system conventionally uses a Kretschmann-Raether configuration, described in subsection 2.2.2. Yet, other coupling methods such as nanostructures [109], waveguides [110, 111], and combination of both of them [112] with a LOD in the range of 10^{-5}-10^{-6} RIU were as well studied. The two first parts of the present section will be devoted to the most conventional plasmonic MZI based on Kretschmann configuration and waveguide coupling. The last part will focus on an alternative with a grating-coupler configuration based on a differential measurement.

2.3.1 Prism-coupler

As previously mentioned, the SPR-based detection devices use different interrogation methods to assess the variations in the bulk RI and/or biomolecular interactions onto the detection surface of the device. Angular, spectral and intensity interrogations are the most commonly used. Yet, phase analysis demonstrated a great promise to improve the performance reached by SPR transducers during the last years, and especially their sensitivity [69, 109, 112]. The plasmonic MZI is based on this promising interrogation method [84]. This sensing approach assesses the RI variations at the metal-sensing medium interface by the phase shift in an output interference pattern. This interference pattern results from the superposition of a SPR-affected beam with a reference beam as shown in Figure 2.13.

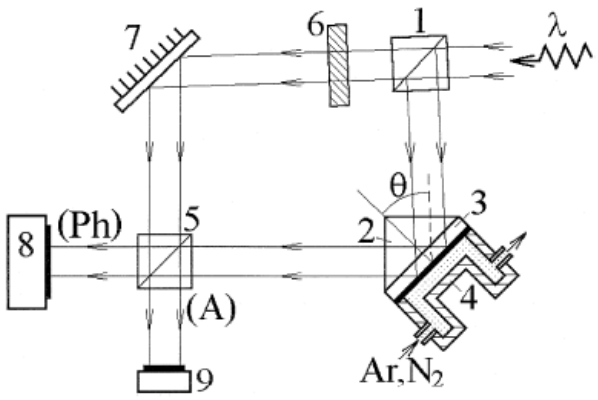

Figure 2.13: Sketch of the plasmonic MZI comprising (1)(5) beam splitters, (2) a prism, (3) a slide covered with a thin gold layer, (4) a gas cell, (6) an absorbing filter, (7) a mirror, (8) a CCD-matrix, and (9) a wide-aperture photodiode. This figure is extracted from the article [113]. Reprinted with permission from Elsevier, https://doi.org/10.1016/S0030-4018(97)00726-8. Copyright © 1998 Elsevier Science B.V.

Basically, the setup of such sensor involves a beam splitter, which separates an impinging p-polarized beam into two arms with different optical pathways. The first one is used as a reference because it does not interact with the SPR-coupler of the setup, contrary to the second one, which is used as a sensing arm because of its interaction with the SPR coupler under the resonance conditions for the initial sensing medium.

Thus, when binding events and/or a variation in RI onto the detection surface occur, the SPR conditions are no longer fulfilled under the initial resonance conditions. This manifests through a new spatial phase distribution in the interference pattern, and therefore through a shift of the clear and dark fringe positions in the interference pattern. Such detection strategies led to high performance such as a LOD in the range of 10^{-8} RIU [113].

However, the beams associated with each arm have distinguished optical pathways. That can introduce noise into the measurements if a perturbation induces a variation of phase in only one arm. To overcome this issue, another but similar configuration comprising a non-polarized

incident beam and a Wollaston's prism [84], sketched in Figure 2.14, was elaborated.

Basically, this setup uses a Wollaston's prism before the detectors to separately gather the recombinations of the sensing arm and the reference arm respectively associated with the p- and s-components. Since only the p-component of the non-polarized beam is affected by the SPR effect, the perturbation introduced into the system due to the different optical pathways between the reference and the sensing arm of the p-component can be canceled and removed from their resulting output interference patterns by a differential measurement between the phase of the interference pattern associated to the p- and the s-component.

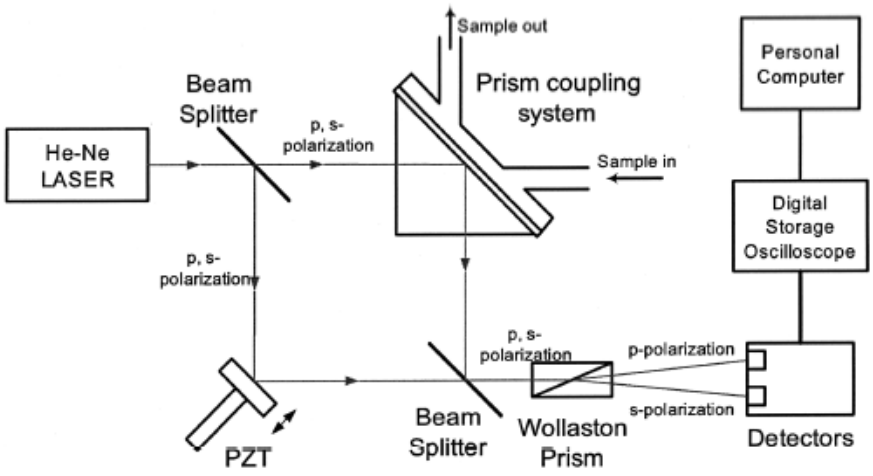

Figure 2.14: Sketch of the plasmonic MZI based on a differential measurement between p- and s-polarizations. This figure is extracted from the article [84].

Figures 2.15 and 2.16 show measurements performed with such a setup to detect and assess the concentration of glycerin in solutions comprised of different ratios of deionized water (DI) and glycerin. Figure 2.15 gives the initial interference pattern of the s- (violet curve) and the p-polarizations (blue curve) for DI, used as the reference solution. These interference patterns are in phase opposition. The differential phase shift between each polarization is also initially equal to 180 degrees.

Figure 2.16 shows the differential shift induced by the sequential injection of three solutions containing different concentrations in glycerin and DI. The injection of all solutions was cycled once to demonstrate repeatability. The repeated injection of DI results in a differential phase shift around 180 degrees. Besides, the higher the concentration in glycerin in the other solutions injected, the higher the shift in the differential phase output. In addition, both injection of each solution comprised of glycerin and DI resulted in a quite similar value. The slight mismatch between each cycle of measurements is due to drift. This effect was corrected by laser feedback interferometry in another study [114]. Yet, that resulted in a more complex and cumbersome arrangement.

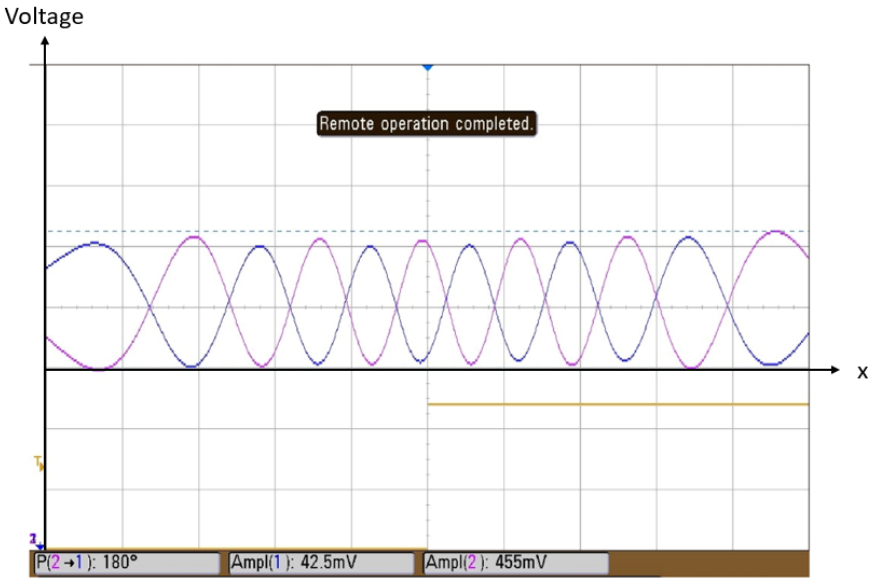

Figure 2.15: Interference pattern of the SPR response of the s- (violet curve) and the p-polarizations (blue curve) for DI (reference solution). This graph is extracted from [115]. Reprinted with permission from Elsevier, https://doi.org/10.1016/j.optcom.2016.06.033. Copyright © 2016 Elsevier B.V. The voltage and x axes were added to the original figure.

With this configuration, a high LOD in the range of 10^{-8} RIU was achieved. In addition, working at a fixed incident angle avoids an angular scan each time a new solution is injected through the

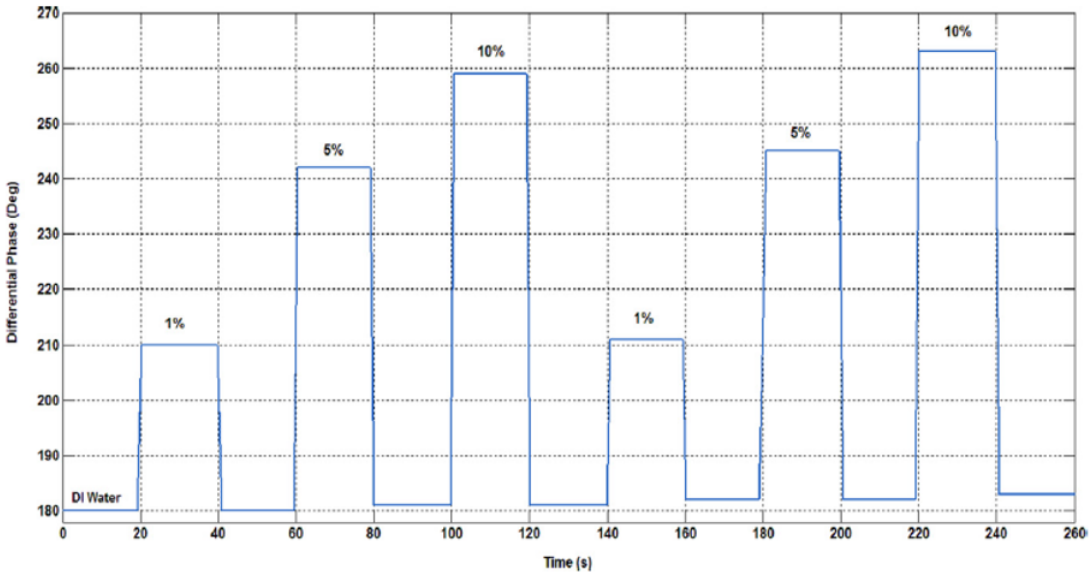

Figure 2.16: Differential phase shift induced by the sequential injection of three solutions containing different concentrations in glycerin and water (reference solution). The injection of all solutions was cycled once to demonstrate repeatability. This graph is extracted from [115]. Reprinted with permission from Elsevier, https://doi.org/10.1016/j.optcom.2016.06.033. Copyright © 2016 Elsevier B.V.

detection device or the use of a spectrometer, contrary to the conventional SPR sensors based on wavelength or angular interrogation method.

Yet, the dynamic range of this approach is very limited due to the abrupt variation of the phase, as illustrated in Figure 2.17, which results in a decrease in sensitivity while the concentration of the targeted analytes increases.

Consequently, this configuration is more adapted for logical sensors assessing if a concentration is or is not above a fixed threshold [113]. Moreover, even if this approach of detection presents high performance, the combination of the MZI with SPR coupling configuration is rather bulky and expensive. Therefore, it does not give the best miniaturization outlooks and is also not the most suitable detection device for the POC settings.

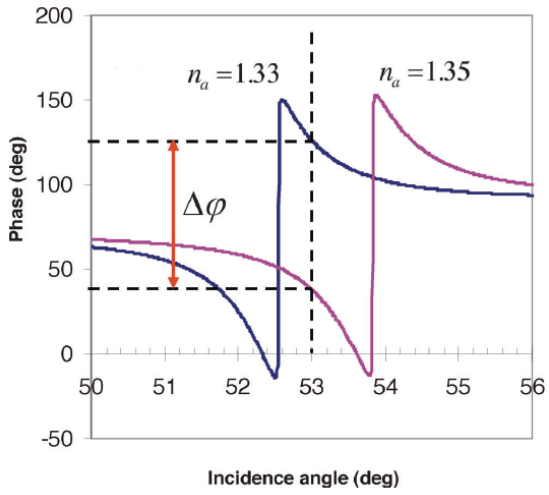

Figure 2.17: Shift in the phase due to an increase of the bulk RI in the sensing medium. This graph is extracted from the article [69].

Finally, it must be mentioned that other plasmonic interferometers based on a phase-modulation were demonstrated as high-sensitive detection devices, such as Fabry-Pérot and Michelson [116]. However, they respectively suffer from complex fabrication and a restricted wavelength range along with sensitivity to mechanical vibrations. Their production is also not aligned with low-cost mass production. For this reason, the MZI seems to offer the best trade-off among all these plasmonic interferometers despite its limitations previously mentioned for its use at the POC. For this reason, other plasmonic MZIs based on waveguides offer better perspectives for miniaturization as described in subsection 2.3.2.

2.3.2 Waveguides

Contrary to the prism-coupler, the waveguide benefits from a high degree of miniaturization and is easier to integrate into a microfluidic system. Thus, different designs of compact MZI sensors using waveguides [110, 111, 117, 118] were developed to combine the advantages offered by the waveguide and the interferometers. Figure 2.18(a) gives a sketch of the most widespread and

basic sensor based on a waveguide MZI [119]. This configuration generally consists in an input waveguide divided into two arms via Y-junctions: one used as a reference arm and the second used as a sensing arm. The sensing arm (on the left) is exposed to fluids (sensing media) over a distance, L, contrary to the reference arm (on the right), which is embedded in a polymer such as CYTOP, as sketched in Figure 2.18(b). Then, both arms are recombined via a Y-junction. Thus, the guided modes propagating through each arm are interfered.

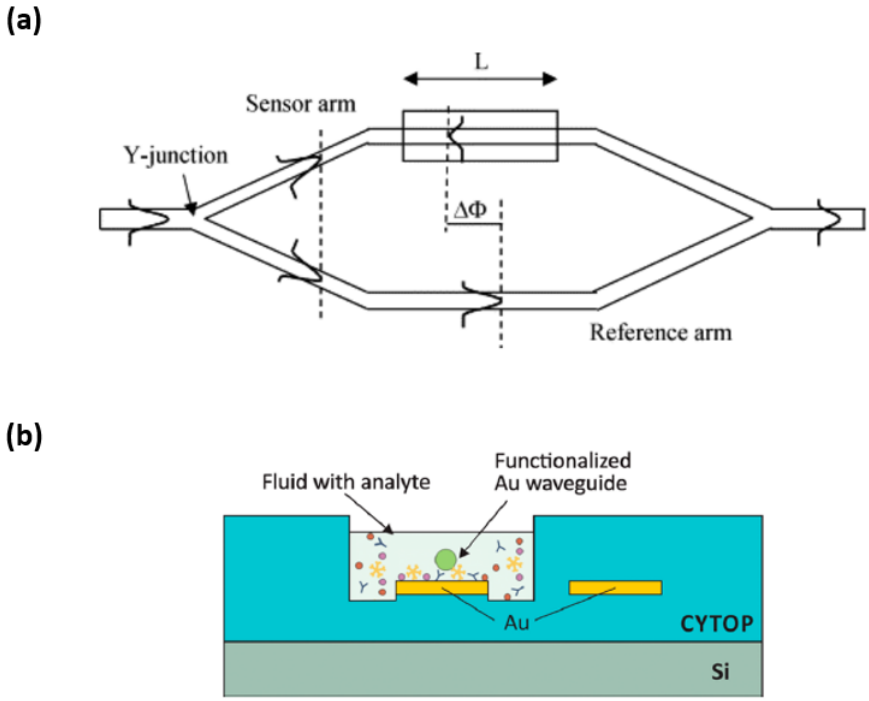

Figure 2.18: (a) Sketch of an integrated MZI based on waveguides with a single output. $\Delta\Phi$ represents the phase shift between the guided modes propagating through the reference and the sensing arms. This sketch is extracted from [120]. Reprinted with permission from Elsevier, https://doi.org/10.1016/S0925-4005(03)00257-0. Copyright © 2003 Elsevier Science B.V. (b) Front cross-section of a MZI based on plasmonic waveguides showing a functionalized waveguide (sensing arm) and a CYTOP-embedded waveguide (reference arm). This sketch is extracted from the article [121]. Reprinted with permission from American Chemical Society. Copyright © 2014 American Chemical Society.

A light beam is coupled into the input waveguide. The sensing channel is initially exposed to a

reference solution. Thus, the phase shift, $\Delta\Phi$, between the guided modes propagating through the reference and the sensing arms, is defined by the relation below:

$$\Phi_D = \frac{2\pi L}{\lambda_0}(n_{eff,s} - n_{eff,r}) \tag{2.10}$$

where $n_{eff,s}$ and $n_{eff,r}$ represent the effective RI in the sensing and the reference arms.

When binding events or a change of RI occur at the interface between the sensing medium and the metallic waveguide in the etched (sensing) channel, a variation in $n_{eff,s}$ results, which in turn changes the phase shift between the reference and the sensing arms relative to the reference solution. Changes in phase shift manifest through a variation in the output power collected by a detector[101]:

$$P_{out} = P_{in}e^{-2\alpha(L_0+L)}\frac{1}{2}(1 + cos\Phi_D) \tag{2.11}$$

where L_0 corresponds to the length of the full MZI minus the sensing length L, P_{out} is the output power collected by the detector, P_{in} represents the input power coupled into the input waveguide and α is the attenuation coefficient. Thus, biomolecules immobilized on the sensing waveguide or the change of RI over its surface can be assessed.

Figures 2.19(a) and (b) show measurements performed in this specific MZI configuration. Figure 2.19(a) gives the real-time sensorgram (on the bottom) for the sequential injections of DI and five solutions comprised of different ratios of glucose and DI. Based on the output power collected by the detector and presented in this sensorgram, the phase shift, $\Delta\Phi$, between the guided modes in the reference and sensing arm is computed and given on the top of Figure 2.19(a). In this sensorgram, the baseline is recovered for each injection of the reference solution (DI) and the phase shift decreases while the concentration of glucose in the injected solution is low (higher dilution ratio).

Figure 2.19(b) shows the linear correlation between the output phase shift and the RI variations due to the sequential injection of solutions comprised of different ratios of water and NaCl

over the detection surface in a similar integrated MZI. The real-time bulk sensing sensorgram for the injection of the second solution comprising of DI and (125 mM of) NaCl is given in the inset on the left.

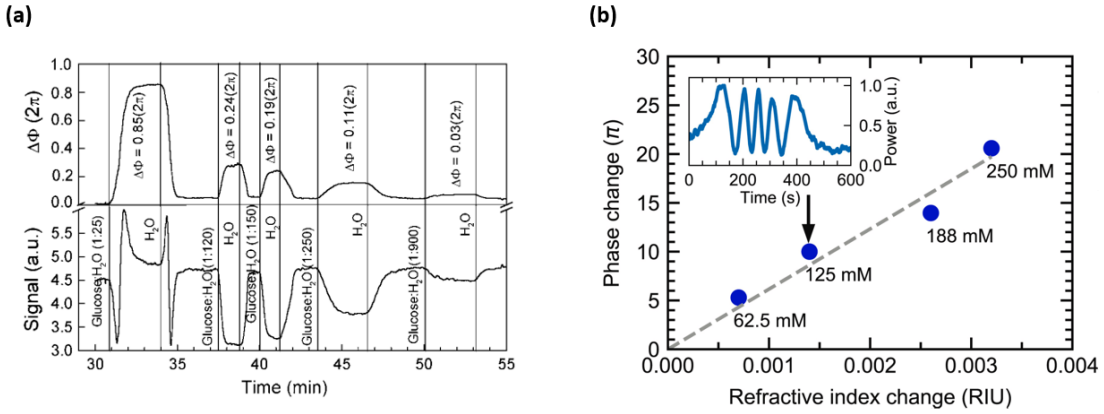

Figure 2.19: (a) Sensor response (bottom) and associated phase shift (top) due to variations of the RI over the detection surface induced by the sequential injections of several mixtures of glucose and DI. This figure is extracted from [122]. Reprinted with permission from IOP Publishing. (b) Graph showing a linear correlation between the phase change and the RI variations over the detection surface of an integrated MZI reported in [123]. The inset on the left gives the real-time bulk sensing sensorgram for the second variation of RI given in the graph. This figure is extracted from the article [123]. Reprinted with permission from Elsevier, https://doi.org/10.1016/j.bios.2021.113816. Copyright © 2021 Elsevier B.V.

Thus, LOD in the range of 10^{-6}-10^{-7} RIU were achieved with such integrated MZI. In addition, as shown in Figures 2.19(a) and (b), this plasmonic configuration was used for various applications in toxicology [124], for the detection of pesticides [122] and microRNA [125], which are promising biomarkers for human diseases in complex samples such as urine, and as immunosensor [126, 127].

In addition, certain specific designs such as that based on dual output MZI sketched in Figure 2.20(a) and reported in [110] showed high potential to cancel noise, as shown in Figure 2.20(b). Besides, asymmetric designs of MZI were as well developed to enhance the phase shift accumulated at the output, as shown in the red box in Figure 2.20(c).

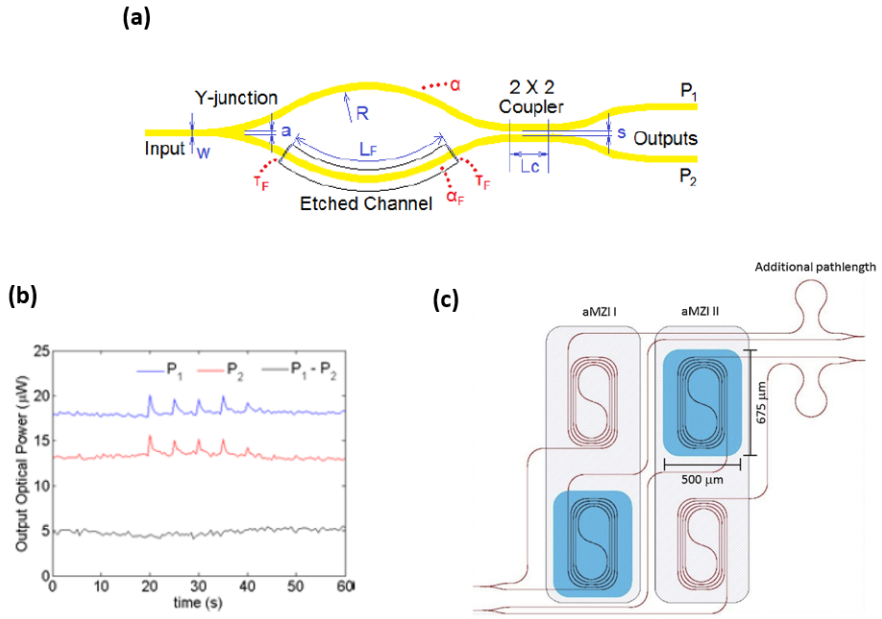

Figure 2.20: (a) Sketch of a dual output MZI. The dimensions labeled on the parts are: w = 5 μm, R = 5.5 mm, a = 2 μm, L_c = 100.25 μm, s = 3 μm, and L_F = 1.1985 mm. (b) Time traces of every single output (P_1, P_2) and their differential measurement (P_1-P_2) with the introduction of artificial noise. These figures are extracted from the article [110]. Reprinted with permission from IEEE, https://doi.org/10.1109/JLT.2016.2543138. Copyright © 2016, IEEE. (c) Sketch of two asymmetric MZI with an additional path length in each reference arm on the left of the sketch. The blue areas show the sensing arms over which the fluids circulate. This sketch is extracted from [128]. Reprinted with permission from Elsevier, https://doi.org/10.1016/j.snb.2019.126758. Copyright © 2019 Elsevier B.V.

Despite a more elaborated arrangement, this configuration does not provide a significant enhancement of the performance than those achieved with a single waveguide described in subsection 2.2.2. Simultaneous detection of several analytes can be performed using several MZIs in parallel. Finally, gratings are often used to couple the input light beam to the input waveguide, as they provide better integration and alignment tolerance [129], resulting in additional fabrication steps and greater expense.

Thus, other configurations of detection based on a differential measurement and a grating-coupler

were suggested as that described in the next subsection.

2.3.3 Grating-coupler

As mentioned in section 2.2.2, the grating-coupler configuration offers a great tunability compared to other methods of coupling. Moreover, gratings provide better integration and alignment tolerance. Thus, alternatives to MZIs were explored to benefit from the advantages provided by grating-couplers and to enhance the performance via a differential measurement without using a bulky or expensive arrangement.

Thus, Ichihashi *et al.* theoretically studied a specific interaction between a rectangular grating and an incident beam resulting in two resonant dips [130], as shown in Figure 2.21. This configuration is based on a differential measurement, between the shift in the resonant angle respectively induced by the coupling of the incident beam with the $+1^{st}$ and the -2^{nd} diffraction orders of the grating, $\Delta\theta_{+1^{st}order}$ - $\Delta\theta_{-2^{nd}order}$.

This study demonstrated that the sensitivity of such a system of detection could theoretically

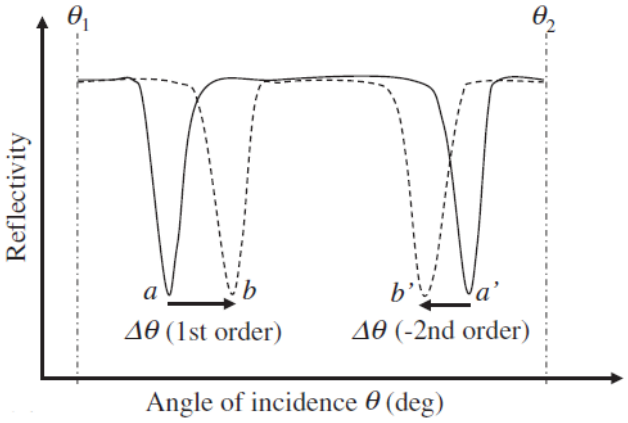

Figure 2.21: Angular spectrum of the 0^{th} order presenting two resonant dips. This graph is extracted from [130]. Reprinted with permission from Springer Nature, https://doi.org/10.1007/s10043-014-0119-5. Copyright © 2014, The Optical Society of Japan.

be improved by a factor 3 compared to the conventional grating coupler configuration described in subsection 2.2.2.

The authors of this work suggest to fabricate the rectangular grating used in this specific configuration by e-beam lithography [131, 132]. Yet, this technique is not well-adapted to mass and cost-effective production. Moreover, it requires an angular scan, which implies that the resonant dips would not be simultaneously measured. A single perturbation during the angular scan could also not been canceled. In addition, the repeated angular scan needed for the reflectance spectrum could introduce noise into the measurements.

In a nutshell, the configuration of detection proposed by Ichihashi *et al.* shows theoretically an interesting potential for sensing applications with a simple and inexpensive setup. Yet, the guidelines suggested regarding the fabrication of the grating design mentioned is not aligned with a low-cost and mass production. In chapter 3, we will propose a similar configuration of detection based on a differential measurement with a grating design easier and cheaper to fabricate. To draw a relevant parallel with existing SPR detection devices based on grating-coupler reported in the literature, the next section will discuss the performance reached by such sensors depending on their design.

2.4 Design and performance of grating-coupler based configurations

As previously mentioned, the great tunability and the excellent integration of the grating couplers into detection devices motivated the optimization of their designs to enhance the performance reached with such SPR sensors. Indeed, several studies highlighted the effect induced by different parameters of the gratings on their optical response, such as the shape of their profile, their period and their depth. The present subsection is also devoted to these effects in the case of a conventional configuration (no interferometer) using a grating-coupler in a SPR detection device.

2.4.1 Effect of the profile

The grating-coupler configuration offers great tunability for sensing. A broad variety of profiles were also studied and developed in recent years to improve the performance of the SPR grating-based sensors [133].

In 2017 López-Muñoz *et al.* developed a plasmonic biosensor based on Blu-ray nanoslits [134], as shown in Figure 2.22(a). This portable biosensor based on a spectral interrogation in reflection achieved a bulk LOD of 6.3×10^{-6} RIU and a LOD in the range of pM for the detection of specific antibodies against a tumor-associate antigen related to colorectal cancer. It reaches a sensitivity of 465 nm/RIU. Yet, the main drawback of such a design is its period shape and size which are fixed by the initial structure of the disc used.

In 2019, Zeynab *et al.* proposed a more tunable graphene and gold-coated ellipse grating as SPR sensor with a spectral interrogation in reflection [87]. They computed the effects of different features of the profile including the horizontal diameter of the ellipse, denoted T_2 in Figure 2.22(b). After optimization of their theoretical design, they demonstrated that such detection device could reach a sensitivity of 1782 nm/RIU.

In the same manner, Chahkoutahi *et al.* suggested similar nanostructures with half-cylindrical-shaped rods in 2021 [135], sketched in 2.22(c). They studied them for the specific detection of different hemoglobin concentrations. Their simulations demonstrated that a sensitivity of 570 nm/RIU could be achieved. These performances obviously higher are certainly due to the more tunable profile proposed. Yet, no fabrication process is suggested to realise such gratings and support such values with experimental results. Moreover, these structures require supplementary layers which make their fabrication more complex and expensive. This would not be aligned with the mass production challenge for large-scale testing highlighted by the pandemic crisis in recent years.

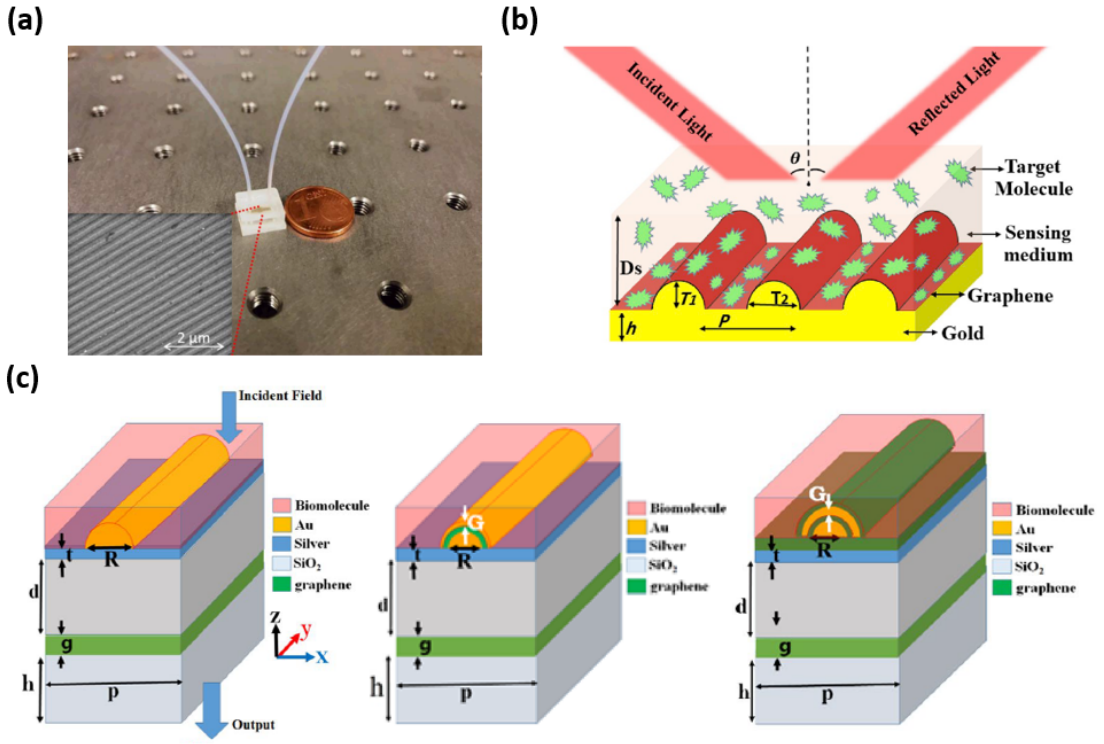

Figure 2.22: (a) Image extracted from [134] of the biosensor with a Scanning Electron Microscopy (SEM) image of the Blu-ray nanoslit integrated inside the fluidic system ahown in inset. Reprinted with permission from Elsevier, https://doi.org/10.1016/j.bios.2017.05.020. Copyright © 2017 Elsevier B.V. (b) Sketch of a graphene-gold ellipse grating used as coupler, extracted from [87], for the SPR detection of analytes in the sensing medium. Reprinted with permission from Elsevier, https://doi.org/10.1016/j.physe.2020.114005. Copyright © 2020 Elsevier B.V. (c) Sketches of three different half-cylindrical periods proposed in [135] to detect hemoglobin concentrations in blood. Reproduced with permission from Springer Nature, https://doi.org/10.1007/s11468-021-01531-5. Copyright © 2021, The Author(s), under exclusive licence to Springer Science Business Media, LLC, part of Springer Nature.

That is why the sinusoidal [64, 136] and the binary [73, 137, 138] gratings, which are easier to fabricate and model, are still currently used. Indeed, LODs about 10^{-5}-10^{-7} RIU were reached with such simple profiles. In 2020 Iqbal *et al.* compared the theoretical sensitivity of both structures under spectral interrogation [88]. They concluded that the sinusoidal grating offered better sensitivity due to stronger fundamental harmonics.

In addition, as it will be explained in section 3.2.1 in the next chapter, a sinusoidal and deep grating will be used as coupler in the new plasmonic configuration demonstrated in this thesis. To draw a relevant parallel with this new configuration, we will focus on the sinusoidal grating profile in the next subsections to study the effects of period and the depth on the performance of the conventional grating-coupler configuration.

2.4.2 Effect of the period

The sinusoidal and rectangular profiles are produced by a fast and inexpensive technique called laser interferential lithography (LIL), which will be described in subsection 3.3.1. Moreover, these profiles benefit from a good tunability. Their performance as sensor transducers can also be optimized by modifying different parameters including the period.

Thus, Dai *et al.* demonstrated in 2018 that the sensitivity of a grating interrogated by an angular modulation could be improved depending on the diffraction order of the grating used to excite a surface plasmon [138]. This choice between a positive or a negative order is conditioned by the value of the grating period (resp. higher or lower), as previously explained in subsection 2.2.2. Thus, a configuration with a surface plasmon excited by a negative diffraction order and so comprising a lower period grating coupler achieves a higher sensitivity compared to a conventional prism-coupler configuration.

In 2019, Cao *et al.* theoretically demonstrated that the period of a grating had a strong effect on the sensitivity under spectral interrogation [139]. This was confirmed in 2020 by Long *et al.*, who demonstrated theoretically and experimentally that a grating with a larger period reached a better sensitivity [140]. They achieved a sensitivity of about 2077 nm/RIU with a sinusoidal grating with a period of 6733 nm.

To summarize, depending on the interrogation method, the period has different effects on the

optical response of a grating. This parameter can be optimized to enhance the sensitivity of a SPR detection device using a grating coupler.

2.4.3 Effect of the depth

As previously discussed, the shape and the period of the grating profile affect the performance reached by the SPR sensors based on a grating coupler. But, the depth can also optimize the performance of such sensors, even if its effect on their optical response is weaker [141]. Indeed, several studies theoretically [142, 143] and experimentally [144] demonstrated that for a fixed period, the depth could enhance the performance of sinusoidal and binary gratings.

Figure 2.23(a) shows four computed resonant dips resulting from the interaction of an incident p-polarized light beam at free-space wavelength $\lambda_0 = 850$ nm with the sinusoidal gold-coated grating sketched in 2.23(b) under the same conditions for different depths of the grating.

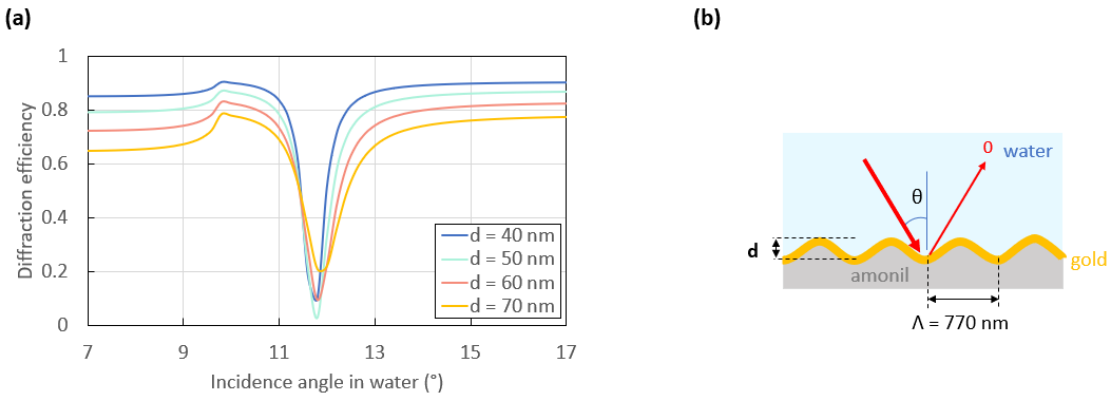

Figure 2.23: (a) reflectivity spectrum resulting from the interaction of a p-polarized incident light beam at free-space wavelength of $\lambda_0 = 850$ nm over an angular scan of the incident angle θ in water with the sinusoidal 100 nm thickness gold-coated grating sketched in (b) under the same conditions but with a varying depth d. The gratings responses were computed via MC-Grating software.

The dip associated with the optical response of the 70 nm grating (yellow curve) is broader and

less deep than the other resonant dips. This results in a higher FWHM and a lower resolution than for the other gratings. Based on our simulations, the 70 nm depth grating will not provide the best performance.

Regarding the dips associated to the optical response of the 40 and 60 nm depth grating (dark blue and orange curves), their depths are quite similar. Yet, the resonant dip associated to the 40 nm depth grating is straighter than that of the 60 nm depth. That implies a higher FOM. Thus, the 40 nm depth grating would be preferred.

The resonant dips associated to the 40 and 50 nm depth gratings are quite similar. Indeed, their computed optical responses are only slightly displaced from each other along the diffraction efficiency axis. That suggests that the optimized depth of the grating is in the range of 40-50 nm.

Figure 2.24(a) shows the shift in the resonance angle for the 30 nm (pink curves), the 40 nm (dark blue curves) and the 50 nm (bright blue curves) deep sinusoidal gold-coated gratings embedded in water (RI = 1.33, solid curve) and a mix of glycerol and water (RI = 1.35, dashed curves), as sketched in Figures 2.24(b)-(d).

As shown in Figure 2.24(a), the shift in the resonance angle is quite identical for the three gratings. Their sensitivities are also quite similar. In addition, the depths of their resonant dip are as well quite similar. The ease of their identification will be the same. Yet, the dips simulated for the 50 nm depth grating in both solutions are slightly broader than those of the 40 nm depth grating. Thus, the 40 nm depth grating provides a better FOM since its FWHM is narrower. Analogously, the resonant dips of the 30 nm depth grating are narrower but also less deep than those of the 40 nm depth grating. In the present case, the 40 nm deep grating would be preferred to the others to reach better LOD and sensitivity. The depth has also an effect on the performance of a detection device based on a grating coupler.

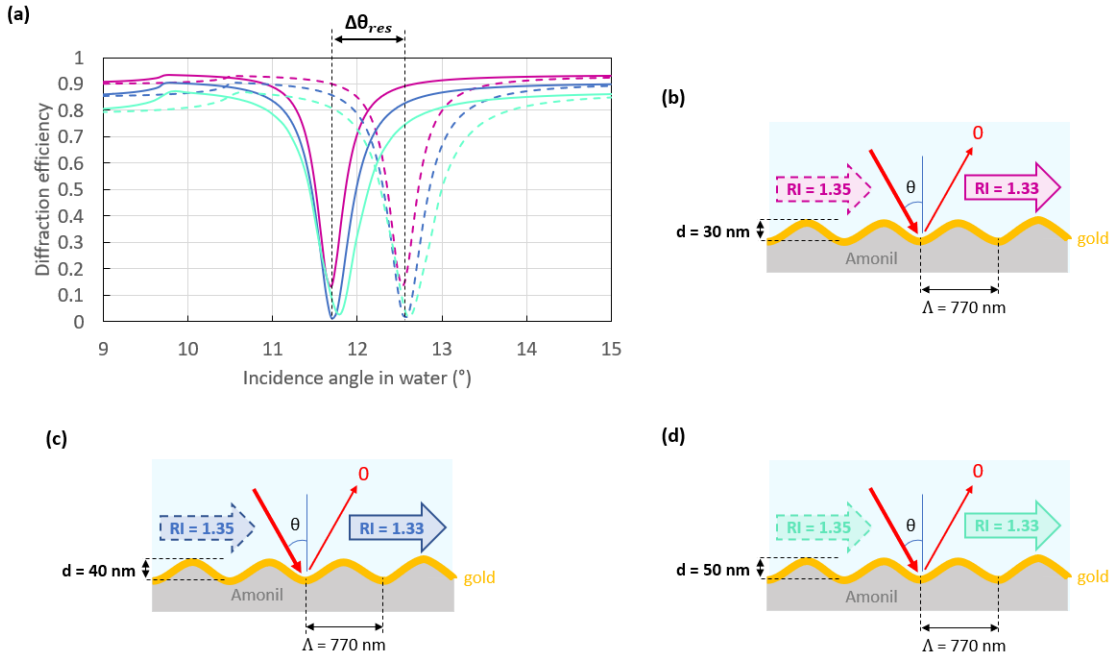

Figure 2.24: (a) Shift in the resonance angle due to a change of sensing medium with different RI (solid curve for initial water and dashed curve for a mix of water and glycerol with a RI of 1.35) for a (b) 30 nm (pink curves), (c) 40 nm (dark blue curves) and (d) 50 nm (bright blue curves) depth grating.

In conclusion, the shape of the profile, the period and the depth of a grating affect its optical response and so the performance reached by the SPR detection device using it as coupler. Their effect can change depending on the method of interrogation used to perform the sensing measurements, especially regarding the period of the grating. In the case of a quasi-sinusoidal grating, the depth is certainly the parameter with the weakest effect on the optical response of the grating, as mentioned in [141].

In the present subsection, we focused on the main parameters of the grating design to optimize its optical response for SPR-based detection. Yet, depending on the initial profile of the grating chosen, the effects induced by other parameters such as the duty cycle, the thickness

and the superposition of metallic layers covering the grating were as well studied to optimize the optical response of these gratings [85, 142, 145].

2.5 Conclusion

The overview of the most widespread SPR-based configurations in this second chapter highlighted their advantages and main drawbacks for POC applications. First, most of them work under angular or spectral interrogation. Yet, an angular scan can introduce mechanical noise into the measurements, whereas spectral interrogation requires the integration of a spectrometer into the detection setup. That involves lower performances or a bulky arrangement, which are not aligned with the challenges of high sensitivity, cost-effectiveness and miniaturization at stake for the detection devices used in POC.

To overcome these issues, other detection devices enabling a differential measurement and/or using other interrogation methods were developed such as waveguide and MZI configurations. Yet, the increase in their performances required more complex protocols of fabrication or cumbersome setups.

That is why, other approaches based on a configuration similar to that using a grating coupler, such as that described in subsection 2.3.3 were theoretically explored. Indeed, grating couplers offer numerous advantages (tunability, portability, miniaturization, easy-to-integrate into a fluidic system, potential for a multichannel system for simultaneous detection of different analytes, ...) for POC applications. Yet, this approach presents limitations relative to the mass production of the grating design used as a transducer.

In the next chapter, we propose a new plasmonic configuration enabling a differential measurement using a grating coupler. The principle of detection in this specific configuration will be introduced and the cost-effective and fast fabrication protocol of the couplers used in this

specific configuration will be detailed.

Chapter 3

Design and fabrication methods

3.1 Introduction

As highlighted in the previous chapter, the sensors using a grating coupler and based on a differential measurement can address the challenges at stake for applications in POC. This chapter proposes a new plasmonic configuration of detection using a grating coupler to leverage an optical effect termed the "optical switch" for sensing. First, the concept of the optical switch is introduced and the principle of detection using this effect is presented. Secondly, the protocol of fabrication applied to obtain the specific design of the grating required to observe the optical switch is detailed. Thirdly, the numerical method (Chandezon's method) used to compute and optimize the theoretical optical response of such nanostructures is presented. Fourthly, the optimization of the theoretical and experimental responses of these gratings is discussed by the study of different parameters (period, depth and profile) and their effects on the optical response of these nanostructures.

3.2 Optical Switch configuration

The present section is devoted to the new plasmonic configuration based on the effect termed "optical switch" developed in this thesis. First, the concept of the optical switch effect will be introduced. Secondly, the principle of detection using this effect will be presented and its specific interest will be explained.

3.2.1 Theory

In this thesis, we focused on an effect termed the "optical switch", reported for the first time in 2014 by Sauvage-Vincent *et al.* [146]. This effect involves a transfer of energy between two orders diffracted by a deep sinusoidal metallic grating, as the angle of incidence is varied over a few degrees about a specific angle of incidence, termed a working point (defined further below). Figure 3.1 shows the first computed switch pattern reported. Curves A and B respectively represent the angular spectrum of 0^{th} and -1^{st} diffracted orders, while curve C gives the balance (summed) spectrum.

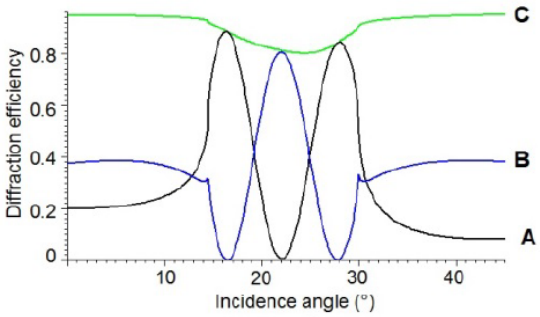

Figure 3.1: Superposition of the computed angular spectra of the 0^{th} (curve A) and -1^{st} (curve B) diffraction orders resulting in an optical switch pattern. The computed balance (sum of A and B) is given by curve C. This Figure is extracted from [146]. Reprinted with permission from Optica Publishing Group, https://doi.org/10.1364/OE.22.013314. Copyright © 2014 Optical Society of America

The detection approach using the optical switch is similar to that used in grating couplers, described in subsection 2.2.2, but with a supplementary condition. It requires that the incoming

beam is simultaneously coupled to two plasmonic modes, one propagating codirectionally and the other contra-directionally relative to the incident beam, instead of only one plasmonic mode, as respectively sketched in Figures 3.2(a) and (b). This condition is always respected under normal incidence [147], but it is naturally no longer always true for oblique incidence. Indeed, under oblique incidence, a shallow one-dimensional grating cannot fulfill this requirement, except if it presents two different spatial frequencies in its Fourier spectrum [148]. But this is not the chosen approach here. In our switch configuration, two specific angles (wavelengths or periods)

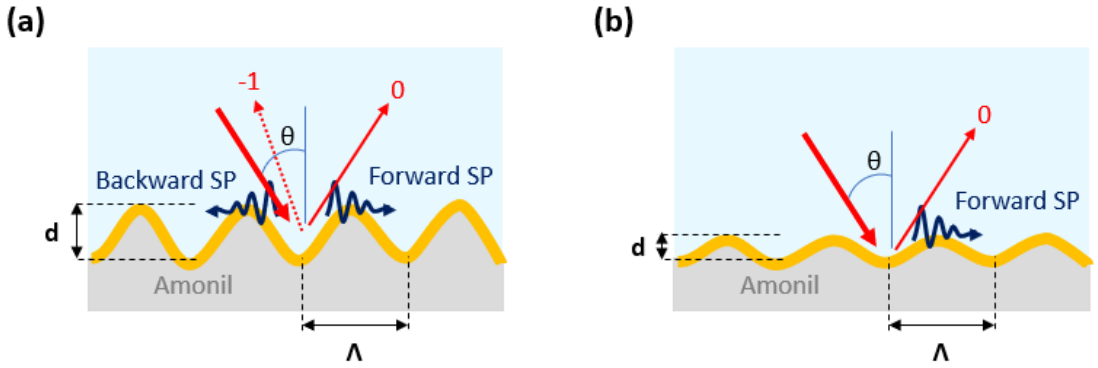

Figure 3.2: 0^{th} and -1^{st} diffraction orders and backward and forward propagating SPs coupled by the interaction of an incident beam with (a) a deep and (b) a shallow grating of amonil covered by a thin gold-layer (yellow layer).

may excite a SP. They are located approximately equidistant on each side of Littrow's angle, θ_L, as shown in Figure 3.3, with Littrow's angle defined by the relation:

$$\sin(\theta_L) = \frac{\lambda}{2 \cdot n \cdot \Lambda} \tag{3.1}$$

where λ represents the wavelength of the incident of light source probing the grating, n is the sensing medium covering this grating and Λ denotes the period of the grating interrogated. The angle on the left of Littrow's angle is denoted θ_{+1}. At this angle of incidence, the incident light wave is coupled to the SP via the $+1^{st}$ order of the grating, which provides $+K_G$ of momentum, as sketched in Figure 3.4(a). The plasmonic mode thereby excited is qualified as a forward SP owing to its propagation direction along the incident beam. This excitation scheme is termed

"codirectional" coupling.

In the same manner, the angle on the right of Littrow's angle, θ_{-2}, refers to the incident angle for which the incident light wave is coupled to the SP via the -2^{nd} order of the grating, providing a $-2K_G$ of momentum, as sketched in Figure 3.4(b). The plasmonic mode thus excited is qualified as backward. Its propagation direction is oriented opposite to the direction of the incident beam. This excitation scheme is termed "contra-directional" coupling.

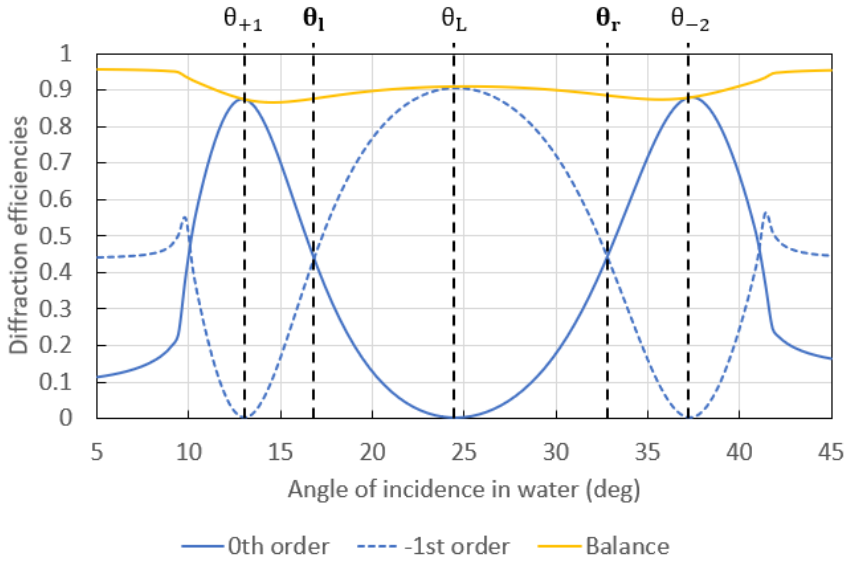

Figure 3.3: Computed switch pattern resulting from the superposition of the angular spectra associated with the -1^{st} and the 0^{th} diffraction orders for a sinusoidal gold grating with a period of 770 nm and a depth of 220 nm probed in water by an incident p-polarized light beam at free-space wavelength $\lambda_0 = 850$ nm. This switch pattern was computed via MC-Grating software.

As shown in Figure 3.3 from the balance curve (yellow) taken as the sum of all diffraction orders power, the SP coupling is almost lossless. Indeed, for both angles (θ_{+1}, θ_{-2}) the sum of the power of the 0^{th} and -1^{st} orders is almost unity. Energy is transferred between the two diffraction orders (-1^{st} and the 0^{th} diffraction orders) while varying the angle of incidence over a few

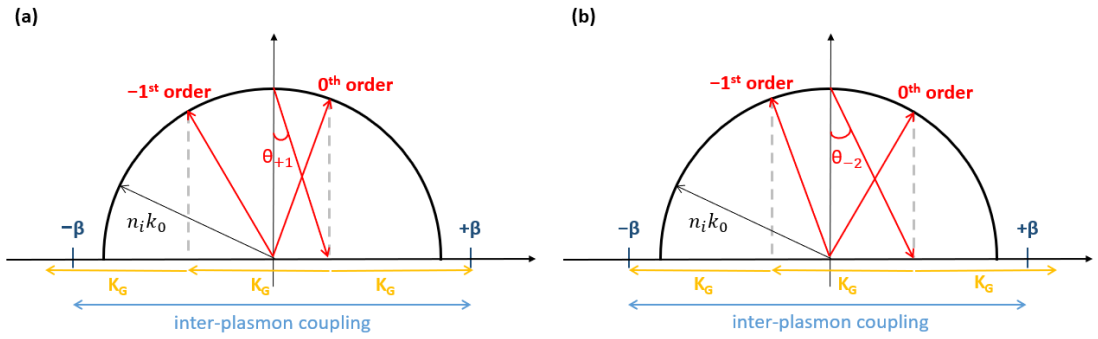

Figure 3.4: (a) Co-directional and (b) contra-directional coupling schemes, illustrating diffraction and SP interaction processes. θ_{+1} and θ_{-2} are the angles of the incident beam. K_G stands for the grating wavenumber (momentum). $+\beta$ and -β respectively denote the propagation constants associated with the forward and the backward SPs. n_i and k_0 respectively represent the RI of the sensing medium and the wavenumber of the incident beam. This figure is extracted from [149]. Reprinted with permission from https://doi.org/10.3390/s23031188. Copyright © 2023 by the authors. Licensee MDPI, Basel, Switzerland. The Authors, licensed under a Creative Commons Attribution (CC BY) license.

degrees about working points denoted θ_l and θ_r in Figure 3.3. This is the so-called "switching effect" [146].

Obtaining a null or at least minimal diffraction efficiency for the 0^{th} order and a maximal one for the -1^{st} at Littrow's incidence by adjusting the grating depth is well-known as much for the s- as for the p-polarization [150]. However, the cancellation of the -1^{st} order and the maximization of the 0^{th} order at the incident angles θ_{+1} and θ_{-2} has been studied and explained only recently with a rigorous phenomenological approach and coupled mode analysis [146]. A subsequent study [150] highlighted that obtaining the peaks and the dips previously mentioned resulted from the contribution of several fields interfering in the directions of the 0^{th} and -1^{st} orders. More specifically, they interfere respectively in a destructive and constructive way in the directions of the -1^{st} and 0^{th} orders.

This is in complete opposition with the commonly used SPR-based configuration which consists in monitoring the angular shift in the resonant dip. Indeed, for this conventional approach,

the resonant dip in the reflectivity spectrum results from the excitement of the SP because of its coupling with a shallow grating, which is much below the wavelength of the incident beam. This manifests through the absorption of the incident wave energy by the SP and also by a loss of energy, as shown by the drop of the balance curve (yellow) at θ_{res} in Figure 3.5.

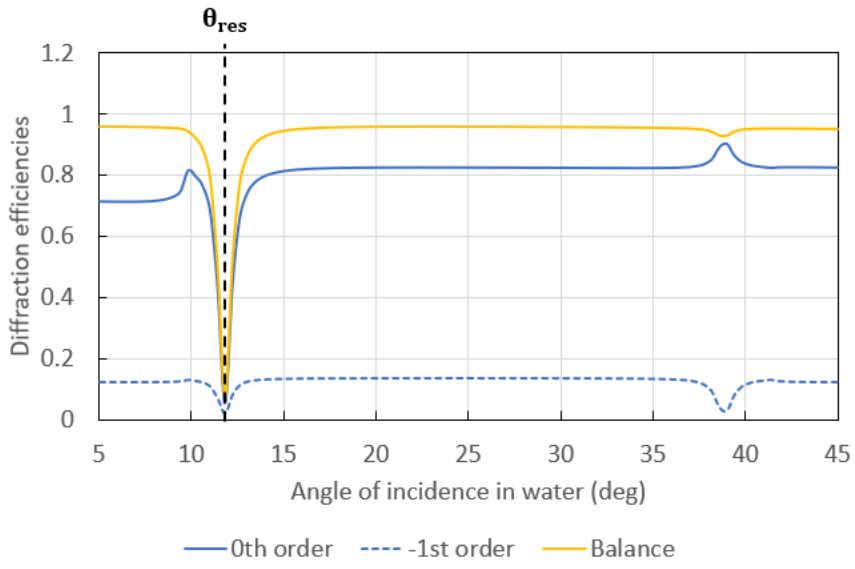

Figure 3.5: Computed SPR response with the superposition of the angular spectra associated with the -1^{st} and the 0^{th} diffraction orders for a sinusoidal gold grating with a period of 770 nm and a depth of 60 nm probed in water by a p-polarized light beam at free-space wavelength $\lambda_0 = 850$ nm. This SPR response was computed via MC-Grating software.

Indeed, in the case of the conventional configuration, if the incident angle is fixed at θ_{res}, there is a coupling from the incident beam to the forward plasmonic mode due to a perfect synchronism described by the relation below:

$$\beta_+ = k_0 \cdot n_a \cdot \sin(\theta_{res}) + K_g \tag{3.2}$$

where β_+ is the propagation constant of the forward SP, n_a stands for the RI of the analyte bounding the interface along which SPs propagate, θ_{res} denotes the angle at which the plasmon coupling occurs and K_G is the grating vector.

Thus, in the example given in Figure 3.5, the 0^{th} reflected order is propagative and the plasmon mode is excited through the $+1^{st}$ order of a shallow 60 nm-depth grating when the synchronism occurs between the wave vector of the incident beam and the wave vector of the SP, as described by the equation 3.2.

In the case of the switch effect, the large ratio between the depth and the period of the grating used results in a large coupling coefficient between the forward and backward plasmonic modes despite the imperfect synchronism:

$$3K_G > 2k_0 \cdot n_e \tag{3.3}$$

where K_G is the grating vector, $k_0 = \frac{2\pi}{\lambda}$ and n_e is the effective refractive index of the SP. This produces inter-plasmon coupling between both plasmonic modes as illustrated in Figure 3.4.

Thus, if the angle of incidence is fixed to θ_{+1}, the co-propagating plasmonic mode is excited by perfect synchronism through the $+1^{st}$ diffraction order of the grating, but it is simultaneously coupled to the contra-propagating plasmonic mode via the 3^{rd} order of the grating. Consequently, the propagation distance of the forward and backward SPs are reduced and so are their respective absorption; thus the low losses observed at this angle [150]. By analogy, the same conclusion is reached by fixing the angle of incidence to θ_{-2}.

To summarize, the optical switch is a quasi-lossless effect resulting from the interaction between a p-polarized light beam and a high depth/period ratio grating. It consists in a transfer of energy between the 0^{th} and the -1^{st} diffraction orders of the grating around two working points at which the power of these diffracted orders are equal. The principle of detection based on this

effect is explained in the next subsection.

3.2.2 Principle of detection

The optical switch pattern presents two working points, denoted θ_l and θ_r (on each side of Littrow's angle), defined as the angles of incidence at which the diffraction efficiencies of the -1^{st} and the 0^{th} orders are equal. To perform sensing measurements, the incident angle is kept fixed at one of these angles. This avoids an angular scan (or the use of a spectrometer depending on the interrogation method chosen), which would introduce mechanical noise into the measurements and increase the cost and size of the interrogation system, thereby limiting the performance and accessibility of the detection device. Thus the optical switch configuration will be interrogated in intensity.

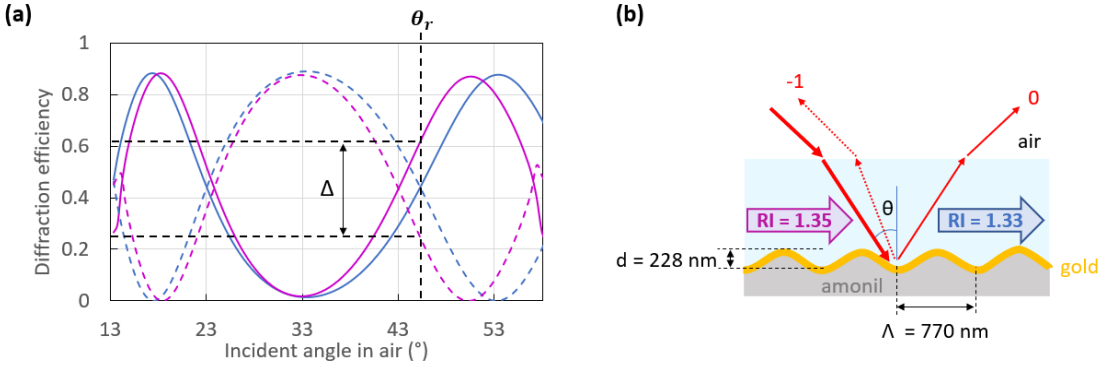

Figure 3.6: (a) Computed angular responses resulting from the interrogation by a light beam at a free-space wavelength $\lambda_0 = 850$ nm of an ideal sinusoidal 100 nm thickness gold-coated grating, sketched in (b), initially covered by water (RI = 1.33, dark blue curves) and then by a solution comprised of water and glycerol (RI = 1.35, pink curves). The dashed and solid curves represent the diffraction efficiencies of the -1^{st} and 0^{th} orders.

Figure 3.6(a) shows two switch patterns, which were computed via the software MC Grating by modeling one period of an ideal sinusoidal gold-coated grating, sketched in Figure 3.6(b), bounded by two different sensing media. The first sensing medium with RI = 1.33 (dark blue curves) is chosen as the reference solution (water). The second sensing medium with RI = 1.35

is a solution comprised of water and glycerol. Under initial conditions (dark blue curves), the incident angle is arbitrarily fixed at the right working point, θ_r, as shown in Figure 3.6(a). The diffraction efficiencies of both 0^{th} and -1^{st} orders are equal, so the differential measurement between these two diffracted orders is equal to zero. Yet, a change of sensing medium (pink curves) modifies the initial switch pattern and results in variations in the diffraction efficiencies of the 0^{th} and -1^{st} orders, which are no longer the same at θ_r. Therefore, the difference in the diffraction efficiencies of the 0^{th} and -1^{st} orders, Δ, at θ_r is no longer zero. Thus, the principle of detection via the optical switch configuration consists in assessing the variation in RI at the metal-sensing medium interface based on the contrast in diffraction efficiency between both 0^{th} and -1^{st} orders with the angle of incidence fixed at a working point.

The main interest in this specific configuration relies in monitoring two diffracted orders with a simple setup (described in section 4.2). It enables differential measurements which cancel the drift and perturbations common to both monitored orders, leading to an improved LOD, as it will be experimentally demonstrated in chapter 4. In addition, the design of the grating used as coupler in this specific configuration can be fabricated by a low-cost manufacturing technique called laser interferential lithography (LIL) [151] described in the next section.

3.3 Fabrication of the grating couplers

The main challenge of this thesis is to propose a low-cost and high-sensitive alternative to the current gold-standards for biosensing. As mentioned in the previous section, deep sinusoidal gratings are used to observe the optical switch effect. To produce such gratings, LIL is a compelling technique since it enables a fast and inexpensive production of many samples on large areas. In spite of its main drawback (incident wavefront curvature), a study [152] mentioned that "for a square 10 cm×10 cm grating of period 1 µm the hyperbolic fringes cause a maximum period perturbation of 2 nm". LIL also enables fabrication of nanograting on large areas. In addition, another study [153] experimentally showed that this effect can be significantly reduced

(by 86%) for such gratings by adding a simple a concave vacuum chuck to the traditional setup used for LIL. Yet, we observed that a prolonged exposure to fluids of the gratings produced by LIL was damageable and modified the surface of these samples. The initial grating masters were also replicated in amonil by a nanoimprinting process to prevent this effect and perform reliable and repeatable detection measurements.

The present section describes all the sequential steps of the protocol for producing the gold-coated grating replicas with an optimized design used to perform the measurements in the optical switch configuration presented in chapters 4 and 5.

3.3.1 Production of grating masters

The first step consisted in producing grating masters in photoresist by LIL with depths greater than those required for the final gratings, to compensate for depth losses induced by the nanoimprint process, and obtain final replicas, as discussed in greater detail in the next subsection. The production of such sample masters required three sequential steps as described below and summarized with the features of each product used in Tables in section 7.1-7.7 (Appendix chapter).

Spin-coating

Spin-coating is a well-established technique for the deposition of thin and uniform layers on flat substrates. Figure 3.7 shows the process applied in the case of this thesis. First, the adhesion promoter SurPass^{TM} 4000 provided by DisChem was deposited on a 26×26 mm^2 glass substrate via a static dispense in order to improve the adhesion of the photoresist applied afterward via the same process. Then, a spin-coating process consisting in two sequential steps at 3000 rpm for 10 s and at 5000 rpm at 50 s was performed. Next, this process was repeated with the positive photoresist Shipley S1828 from MICROPOSIT. Finally, the samples were softbaked for 1 min at 60°C to evaporate the solvent and increase the density of the photoresist layer.

The thickness of the layer deposited by this technique depends on the viscosity of the photoresist

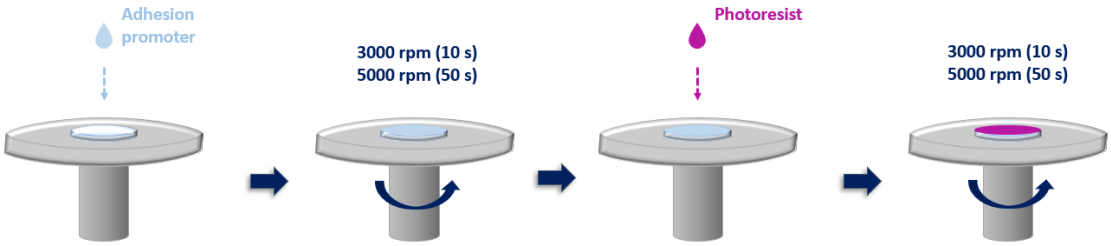

Figure 3.7: Spin-coating process.

and the rotational speed applied [154]. In the case of this thesis, the positive photoresist Shipley S1828 was deposited with the parameters mentioned in Figure 3.7 to obtain a photoresist layer with a thickness of a few hundred nanometers.

To prevent imperfections and discontinuities in the photoresist film deposited by spin-coating, each glass substrate was first of all meticulously cleaned via three sequential steps: ultrasonic cleaning in acetone for 10 min, ultrasonic cleaning in ethanol for 10 min, and static incubation in DI for 10 min. Finally, the samples were dried under nitrogen gas.

Laser interferential lithography (LIL)

LIL is a cheap and fast technique of production for nanostructures on large areas. This method of production is also aligned with low-cost manufacturing and enables the production of various nanotructure profiles [151, 155], including sinusoidal gratings.

Figure 3.8 gives the sequential steps of the protocol applied to fabricate the sinusoidal grating used for this thesis. The photoresist-coated samples were first exposed to a uniform He-Cd laser beam at a wavelength of $\lambda = 442$ nm and an incident power density of 204 μW/cm^2 for 115 s to reach the linear operating regime of the photoresist.

A second exposure was then applied, consisting of the superposition of two balanced and coherent beams from the same laser at an incident power density of 408 μW/cm^2 for 115 s, to

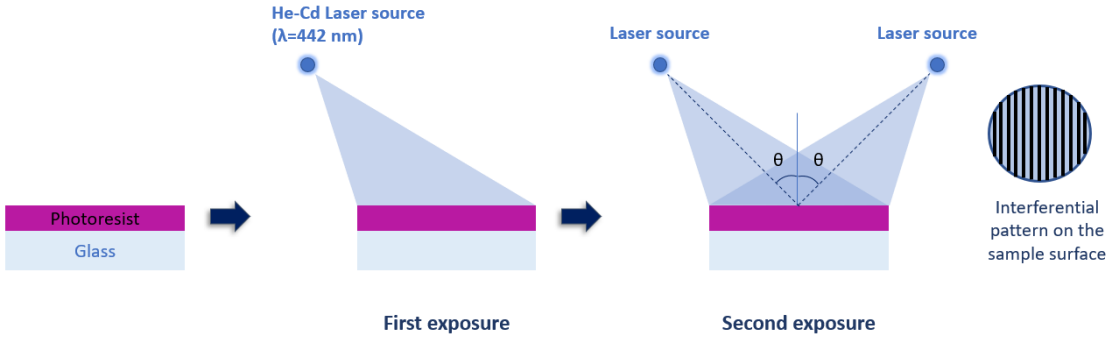

Figure 3.8: LIL process for sinusoidal gratings.

produce the desired interferometric sinusoidal profile. During this second exposure, the grating period, Λ, in the photoresist was fixed at 770 nm by the laser wavelength, λ, and the angle of incidence of the laser beams, θ (controlled by a Labview program), based on the relation below:

$$\Lambda = \frac{\lambda}{2 \cdot sin(\theta)} \tag{3.4}$$

The interference gave rise to a fringe pattern due to the overlap of both beams. This period was chosen based on the optimization of the theoretical switch pattern, explained in subsection 3.4.2.

Development

Two types of photoresist are used to produce nanostructures by LIL: positive and negative. Their solubility in a developer solvent depends on the dose received during their exposure to laser beams. In this thesis, we used the positive photoresist Shipley S1828 to fabricate the grating master.

This photoresist comprises a photosensitive compound called Diazonaphthoquinone (DNQ), which is degraded by illumination and dissolved during the development step. Figure 3.9 illustrates this effect. The most exposed areas (bright fringes) during the second exposure of LIL are removed because of their high solubility, while those not exposed (dark fringes) remain be-

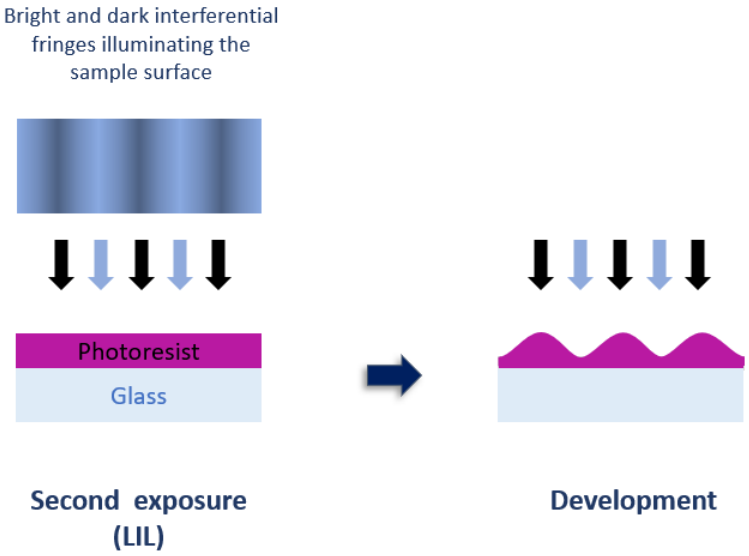

Figure 3.9: Effect induced by the development on the thin photoresist layer depending on the areas exposed to bright (blue arrows) and dark (black arrows) fringes during the second illumination of LIL.

cause of their lower solubility. In the present thesis, the samples were developed in the developer MF319 (MICROPOSIT) for 9 s. Thus, we obtained 770 nm period gratings with a depth about 290 nm, as shown in Figure 3.10. 209 grating masters were directly produced by this protocol of LIL during this thesis.

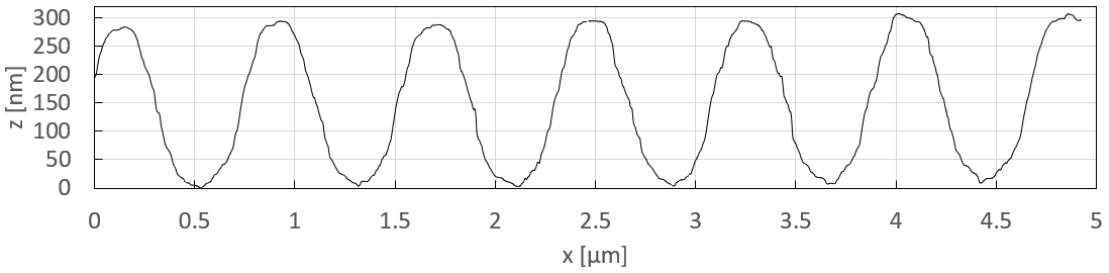

Figure 3.10: Profile extracted from an AFM characterization of a grating master fabricated by the sequential steps of spin-coating, LIL, and development with the parameter previously detailed.

3.3.2 Production of the grating replicas

As previously mentioned, we noticed that a prolonged exposure to fluids damaged the gratings produced by these steps, resulting in non-repeatable sensing measurements. Thus, a nanoimprinting process was developed to replicate these gratings in a harder material - Amonil. In the present subsection, the sequential steps of the nanoimprinting process applied to produce harder grating replicas are described and summarized with the features of each product used in tables in section 7.13-7.19 (Appendix chapter).

PDMS stamp

The PDMS (polydimethylsiloxane) stamp fabricated to transfer the sinusoidal master grating was produced via the following detailed protocol sketched in Figure 3.11. This step of the protocol of fabrication was developed and carried out by Nicolas Crespo-Monteiro and Arnaud Valour. First, a "hard" PDMS solution was formed by mixing in a 3:1 ratio (by weight) RTV615 silicone rubber compound with a curing agent (Momentive^{TM}). The solution was then deposited on the master fabricated by LIL by spin-coating (10 seconds at a speed of 3000 rpm followed by 50 seconds at 5000 rpm). This deposition fills the pattern of the master, as shown in Figure 3.11. Then, this sample was sequentially soft-baked at 50°C for 30 minutes and 70°C for one hour. Next, the hard PDMS-coated master is placed in a sample holder, and coated by a "soft" PDMS solution formed by mixing in a 9:1 ratio (by weight) RTV615 silicon rubber compound with a curing agent. This sample is finally soft-baked at 70°C for two hours. Coating with a soft PDMS layer more easily enables removal of the PDMS stamp from the master. Indeed, the hard PDMS is stiffer and also harder to manipulate.

Nanoimprinting process

To transfer the sinusoidal grating pattern to a more resistant material than the photoresist, a thin layer of Amonil MMS1 was used as the imprint resist. This layer was deposited by spin-coating on a clean 26 $\times$ 26 mm^2 glass substrate after previous deposition of Amoprime as adhesion

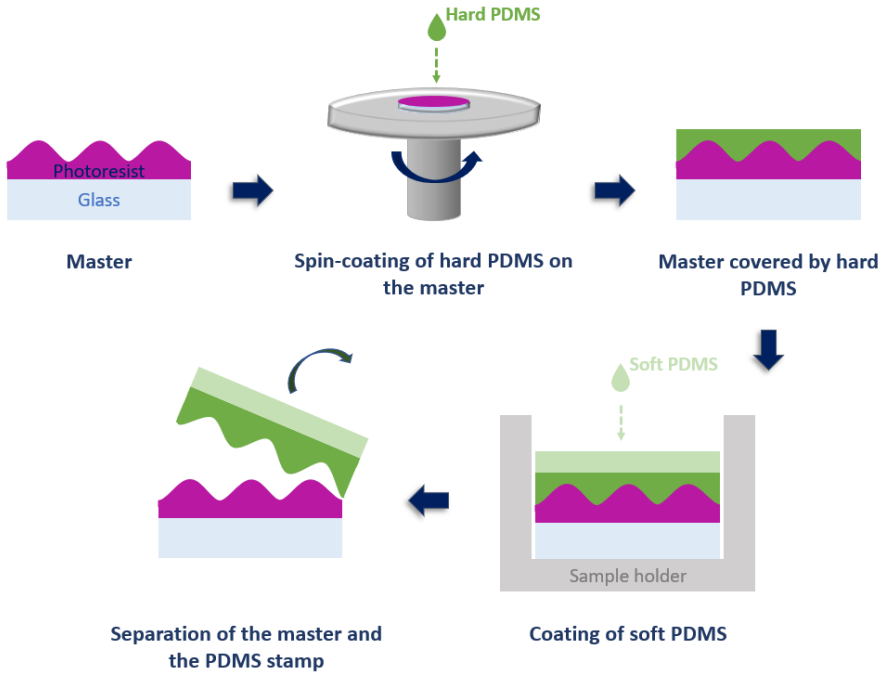

Figure 3.11: Sequential steps of the protocol for the production of a PDMS stamp.

promoter. Secondly, a low imprint pressure of 1 Bar was applied for 30 seconds using a printing press to the PDMS stamp in contact with the sample. Thirdly, the sample was illuminated by a UV lamp (Ucube 365-100-2) provided by Uwave to harden the imprint resist. Finally, the stamp was released from the replica, which was then soft-cured at 60°C for 1 min. This step of the protocol of fabrication was carried out by Arnaud Valour for the most of the grating replicas. 87 grating replicas were directly produced by the combination of LIL and nanoimprint processes previously described.

Nanoimprinting presents several advantages. Firstly, it provides samples which are reusable many times contrary to samples only fabricated by LIL. Thus, a few dozen assay were performed with each sample produced by this process. This is aligned with the challenge of a low-cost. Secondly, it enables the production of many similar samples from a single master and thus is especially appealing for mass production. Thirdly, it reduces the average roughness, R_a, of the

samples compared to the initial master as shown in Figure 3.12. The average roughness is defined as the average deviation of all points of a profile from a mean line taken over the evaluation length, as described by the equation below [156]:

$$R_a = \frac{1}{N}\sum_{j=1}^{N}|r_j| \tag{3.5}$$

Based on the relation 3.5, the average roughness along the gratings was assessed as 3-6 nm for the profile of the master shown on the top of Figure 3.12, as 0.4-1 nm for the grating replica presented in the middle of Figure 3.12, and as 1-4 nm for the metallised grating replica given on the bottom of the same figure. The profile of the master is obviously rougher than that of the replica. We assume that this effect is due to the surface tension of the Amonil used to transfer the pattern of the PDMS stamp provided from the initial grating master. In addition, although the profile of the metallised replica slightly increases the roughness of the sample, this roughness remains lower than that of the master.

Fourthly, this process enables to slightly modify the profile of the initial grating masters. Indeed, the comparison between the period extracted from each profile and a perfect sinusoid, given in Figure 3.12, shows that the profile of the initial grating master agrees less with a perfect sinusoid than those of the replica (metallised or not). Here again, we assume that the surface tension of Amonil plays a role.

However, nanoimprinting also induces a decrease in the depth of the initial grating. Indeed, Figure 3.12 shows that in the case of the sample presented, a decrease slightly higher than 50 nm was observed between the depths of the initial master and the replica.

Among all of the samples replicated by this process, we observed a depth loss between 1% and 44% compared to the initial depth of the master used to produce the replicas depending on the depth of the master. Indeed, we noticed that for grating masters of depth greater than 250

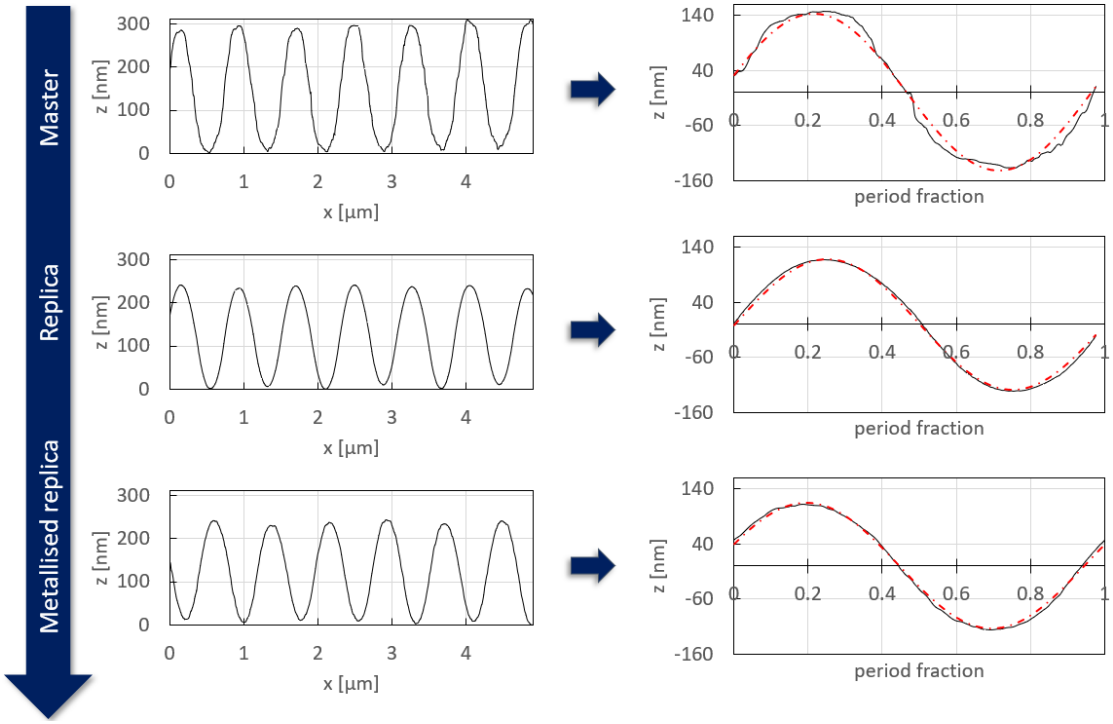

Figure 3.12: Evolution of the grating profile from the initial master to the metallised grating replica as measured by AFM scans (left panels). The right panels show a period extracted from each AFM profile with a perfect sinusoidal fit (red dashed-dotted curve)

nm, most of the replicas produced had a depth near 250 nm (irrespective of the master depth), as shown by the graph in Figure 3.13. Part of the depth loss occurs when the sinusoidal pattern is transferred from the PDMS stamp to the grating replica, because the replicas produced from the same PDMS stamp do not have the same depth, as shown in Figure 3.13. Indeed, although most of the replicas have a depth of about 250-260 nm, some of them present higher and lower depths.

Part of the depth loss is also likely due to transfer of the initial sinusoidal pattern defined in photoresist by LIL to the hard PDMS stamp. That would explain why no replica reached the same depth as the initial grating master.

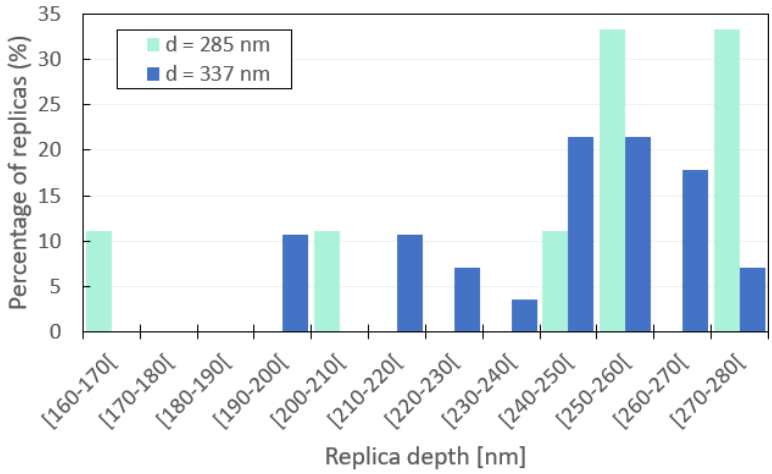

Figure 3.13: Distribution of replica depths from two grating masters with an initial depth, d, of 285 nm (green) and 337 nm (blue); 9 replicas were formed with the 285 nm deep master and 28 were formed with the 337 nm deep master.

3.3.3 Deposition of thin metal layers

To form the final grating couplers, chromium and gold layers were sequentially deposited on the Amonil replicas by thermal evaporation. A thin chromium layer was used as an adhesion promoter for the gold layer. The deposition rates and the final thicknesses were about 3-4 Å/s and 6-7 nm for the chromium film, respectively, and 13-14 Å/s and 120-121 nm for the gold layer, respectively. These two layers were deposited in a vacuum chamber pumped to a pressure of about 10^{-6} mBar. The thickness of the gold layer was chosen to be greater than 100 nm to prevent transmitted orders from emerging during the detection measurements. For the sample shown in Figure 3.14(a), an average depth of 228 nm was measured by AFM characterization, as shown Figure 3.14(b) and (c).

3.4 Design of the diffraction gratings

In recent years, the optimization of the grating design to improve the performance of the SPR-based sensors was widely explored. This effort was supported by numerical modeling methods such as the C method (Chandezon's method). The next section will be devoted to this modeling

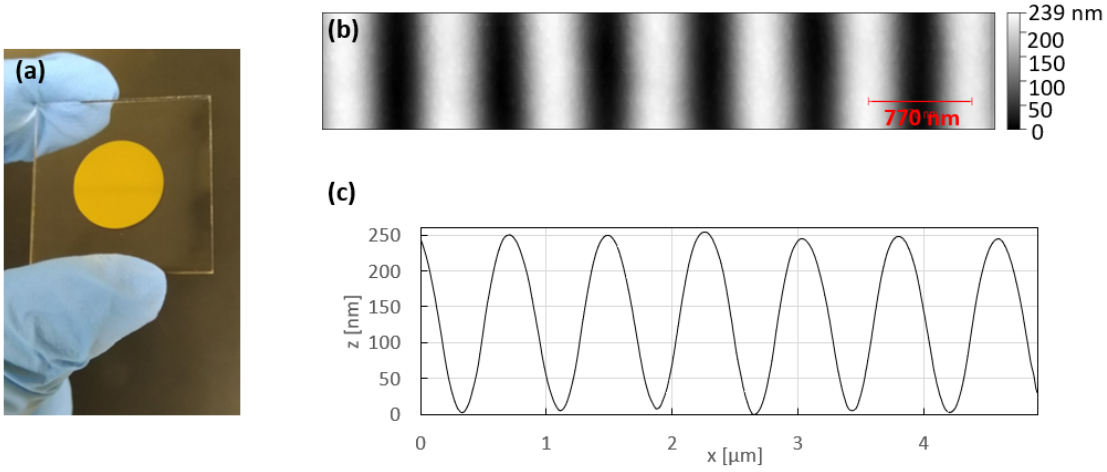

Figure 3.14: (a) Picture of a chromium and gold-coated grating replica with (b) a partial AFM characterization of its surface featured by (c) a sinusoidal profile. These pictures were extracted from the article [149]. Reprinted with permission from https://doi.org/10.3390/s23031188. Copyright © 2023 by the authors. Licensee MDPI, Basel, Switzerland. The Authors, licensed under a Creative Commons Attribution (CC BY) license.

method for diffraction gratings, which was used to compute the theoretical optical response of the sensor developed in the present thesis. This computational technique will first be described. Then, its use to simulate and optimize the theoretical optical response of the gratings used in the experiments will be justified. Finally, the effects induced by several grating parameters (period, depth, profile) on the switch pattern will be theoretically and experimentally highlighted and discussed.

3.4.1 Chandezon's method

The C method is a formalism elaborated by Chandezon and co-workers in 1980 to model surface-relief gratings [157, 158]. It consists in formulating Maxwell's equations into a non-orthogonal system (u,v,w) described by:

$$u = x, v = y, w = z - a(x) \tag{3.6}$$

where (x,y,z) is the rectangular Cartesian coordinate system and $a(x)$ is a function of x such as $a(x) = z$.

In this manner, curvilinear structures can be considered as flat surfaces in the Cartesian coordinate system, separating two heterogeneous media such as those denoted D_{fluid} and D_{metal} in Figure 3.15, having a permittivity and permeability that depends on the coordinate u. Thus, the continuity of tangential field components at the interface is easily enforced. Indeed, the matching conditions at the interface between both media are made easier by the equality of Fourier coefficients along $w = 0$ on each side of the interface.

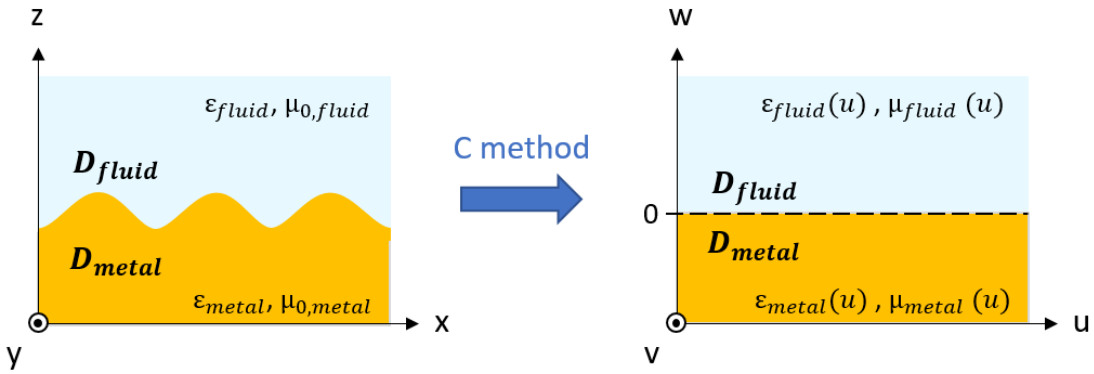

Figure 3.15: Sketch of the transformation of a corrugated grating into a flat interface by the C method.

This method offers several advantages compared to others such as RCWA (rigorous coupled-wave analysis). Firstly, it is simultaneously applied to both s- and p-polarizations as the formulation of Maxwell's equation is the same for each of them. Secondly, the C method is exact and does not approximate the profile of the grating [159]. Also except for binary structures, this method is more efficient for most of the grating profiles. Finally, this method offers versatility and simplicity. The C method is self-consistent. It doesn't use the grating equation, but only Maxwell's equations.

Preist *et al.* demonstrated in 1995 application of this method for periodic multilayer gratings with arbitrary shapes [160]. These results certainly contributed to the improvement of sensor performance via the optimization of more elaborated structures, like those mentioned in subsection 3.4.2 and several others such as those presented in [161, 162].

In the same manner, Chandezon *et al.* recently demonstrated that this method, combined with Heisenberg's uncertainty relation, could model diffraction from aperiodic and finite structures [163]. These works could be useful to gain an understanding of the effects of roughness on the optical response of gratings, especially for deep sinusoidal gratings [91] such as those used for this thesis.

In the present thesis, the gratings used to perform the experimental assays were sinusoidal and gold-coated. For such finite conductivity structures, the C method was also justified.

3.4.2 Switch design

In section 2.4, the effects of shallow grating parameters on SPR responses were theoretically and experimentally discussed. In this thesis, similar studies were carried out for the optical switch configuration to produce gratings with an optimized switch pattern. A switch pattern is considered as optimized when the lateral minimal power of the -1^{st} order at θ_{+1} and θ_{-2} as well as the central minimal power of the 0^{th} order at Littrow's angle correspond to the extinction of these orders. Experimentally, a complete extinction cannot be observed, especially because of unexpected reflections of the probing beam with the lid delimiting the flow cell. A coefficient of extinction was also defined by the expression below and considered as optimal when its value was inferior to 10%:

$$C_{ext} = \frac{V_{0,L}}{V_{max}} \times 100 \tag{3.7}$$

Where $V_{0,L}$ is the minimal power measured at Littrow's angle in 0^{th} order and V_{max} denotes the maximal power measured over the angular scan in 0^{th} order anf -1^{st} order. In addition, the

distance between both operating angles θ_l and θ_r must be large enough to distinguish and reach them with the setup presented in the next chapter.

The present subsection presents and discusses investigations of the effect of the period, the depth, and the profile of the gratings used in the switch configuration, on their optical responses. Other parameters such as the roughness [91] were studied but they will not be discussed in detail here.

Effect of the period

The pattern of the optical switch can be modified by changing the period of the nanostructure. Indeed, this parameter modifies the distance between both working points at θ_l and θ_r and the slopes associated with both diffracted orders in the linear region around these angles of incidence.

The distance between both working points must be large enough to experimentally reach and distinguish θ_l and θ_r. Indeed, if these angles are too close from Littrow's angle, θ_L, the photodiode used to measure the -1^{st} order may hide the incident beam and also introduces errors into the measurements.

Regarding the slopes in the linear region around each working point, their value is correlated with the sensitivity of the system: higher are these slopes, higher is the sensitivity of the detection system working in an optical switch configuration.

Figure 3.16(a) shows three computed switch patterns resulting from the interaction of a p-polarized light beam with a varying Λ period sinusoidal grating probed under the same conditions, as sketched in Figure 3.16(b). These three structures theoretically provide an optimal switch pattern with extinctions of the -1^{st} order at θ_{+1} and θ_{-2} as well as an extinction of the 0^{th} order at Littrow's angle. The main differences between the switch patterns of these nanostructures are their slopes in the linear regions around each working point and the dis-

tance between these two points, given by the double arrows in Figure 3.16(a). Indeed, the 750 nm period grating (dark blue curves) presents a larger distance between both working points (black dashed cursors) than the other gratings. Its working points should be easier to access experimentally and to distinguish. However, the 790 nm period grating (yellow curves) presents slightly higher slopes in the linear region around each working point and so a better theoretical sensitivity than the other gratings. The 770 nm period grating (bright blue curves) is a trade-off between the other two gratings.

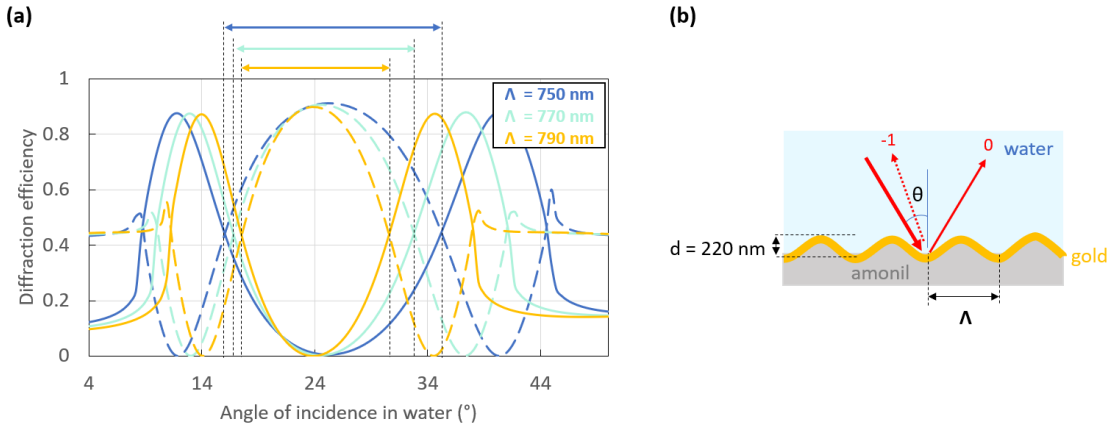

Figure 3.16: (a) Switch pattern resulting from the interaction of a p-polarized beam with the sinusoidal grating sketched in (b). This 100 nm gold-coated grating is interrogated at an incident free-space wavelength of 850 nm over an angular scan in water. The period is the only parameter varied: Λ=750 nm (dark blue curves), Λ=770 nm (bright blue curves), and Λ=790 nm (yellow curves). The dashed curves represent the -1^{st} order while the solid curves represent the 0^{th} order. The double arrows correspond to the distance between both working points for each switch pattern.

Figure 3.17(a) shows the experimental and theoretical normalized switch pattern of a 790 nm period grating, sketched in Figure 3.17(b), that we produced by laser interferential lithography (LIL), with the protocol detailed in subsection 3.3.1. Both theoretical switch patterns were computed by approximating the periods in the colour boxes given in Figure 3.17(c) by a linear combination of 45 sinusoids and using them as representative periods (infinitely repeated) to compute the theoretical switch pattern of the grating via the software MC-Grating. To ensure

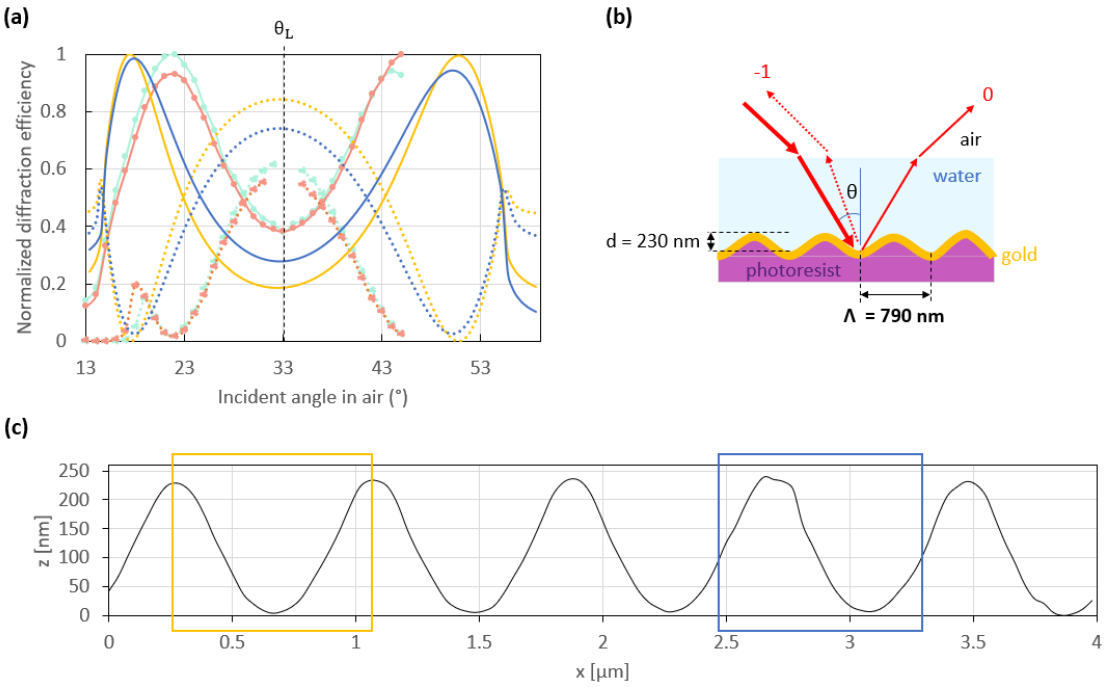

Figure 3.17: (a) Theoretical (dark blue and yellow curves) and experimental (bright blue and orange curves) normalized switch patterns resulting from the interaction of a p-polarized beam at a free-space wavelength of 850 nm with the structure illustrated in (b). The dotted lines represent the -1^{st} order, while the solid lines represent the 0^{th} order. The theoretical normalized switch patterns were simulated considering the period highlighted with boxes of the same colour in (c) which gives the AFM profile of the 100 nm thick gold-coated grating used to measure the experimental switch pattern in (a). The experimental switch patterns were normalized by dividing the respective measurements (photodiode output voltage of the transimpedance circuit) by the maximum value. The theoretical switch patterns were normalized in the same way as the experimental ones (using the computed diffracted waves) to be directly compared.

the relevance of the comparison between all the switch patterns presented in the rest of this thesis, including those given in Figure 3.17(a), a normalization was applied to the experimental and theoretical switch patterns. The experimental switch patterns were normalized by dividing the respective measurements (photodiode output voltage of the transimpedance circuit) by the maximum value. The theoretical switch patterns were normalized in the same way as the experimental ones (using the computed diffracted waves) to be directly compared.

Both experimental switch patterns (bright blue and orange curves) were measured at different locations on the same sample, and they are very similar. That suggests a good uniformity of the sample. However, they are not as optimized as the theoretical switch patterns (dark blue and yellow curves) simulated via the software MC-Grating based on the periods extracted from the AFM profile highlighted by the dark blue and yellow boxes in Figure 3.17(c). Indeed, the working points were rather close to Littrow's angle, θ_L, and also hard to reach without hiding the incident beam. That is why the measurements of the -1^{st} order power were only performed

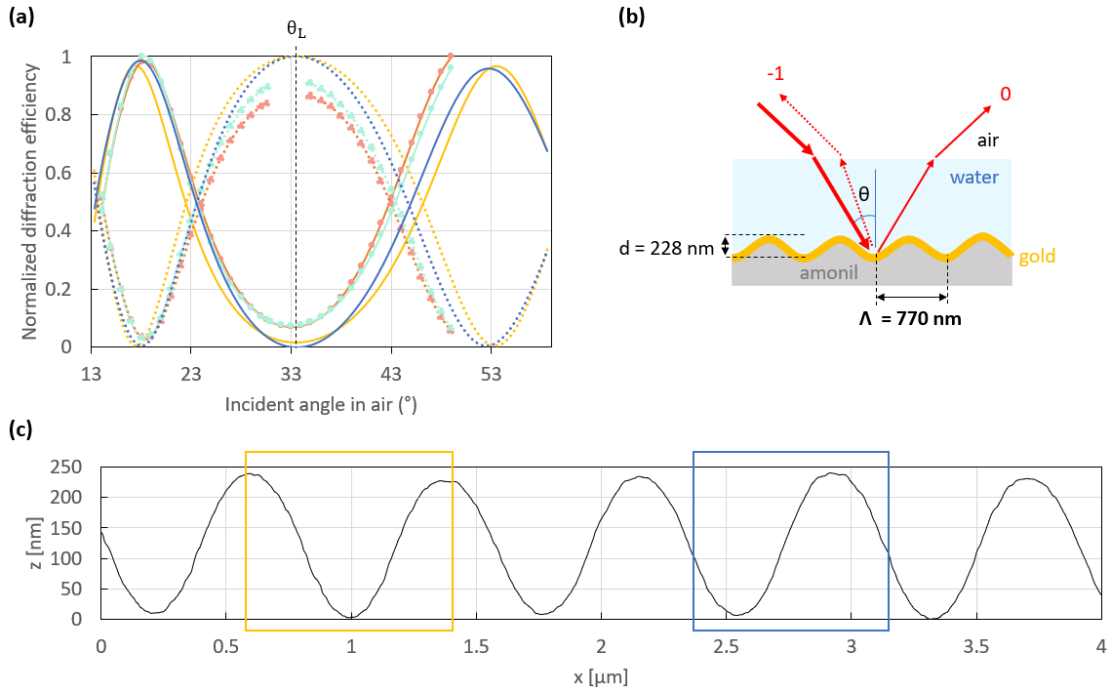

Figure 3.18: (a) Theoretical (dark blue and yellow curves) and experimental (bright blue and orange curves) normalized switch patterns resulting from the interaction of a p-polarized beam at a free-space wavelength λ_0=850 nm with the structure sketched in (b). The dotted lines represent the -1^{st} order, while the solid lines represent the 0^{th} order. The theoretical normalized switch patterns were simulated considering the period highlighted with boxes of the same colour in (c) which gives the AFM profile of the 121 nm thick gold-coated grating used to obtain the normalized experimental switch patterns in (a). The experimental switch patterns were normalized by dividing the respective measurements (photodiode output voltage of the transimpedance circuit) by the maximum value. The theoretical switch patterns were normalized in the same way as the experimental ones (using the computed diffracted waves) to be directly compared.

over narrow angular scans between each working point and Littrow's angle, as shown in Figure 3.17(a). In addition, the contrast in power between the 0^{th} and the -1^{st} orders at Littrow's angle is not as high as expected compared to the theoretical switch patterns - a point that will be further discussed in the third part of this subsection. Indeed, both experimental switch patterns (bright blue and orange curves) respectively present a coefficient of extinction of 37.97% and 38.32%. We assume that these differences between the theoretical and the experimental patterns are in part due to the profile shape, which was not perfectly sinusoidal and to roughness.

Regarding the roughness effect, this hypothesis is in part supported by the theoretical normalized switch patterns given in Figure 3.17(a), which were simulated by considering different periods as representative of the sample used to perform the experimental switch patterns shown in 3.17(c). Indeed, the period in the dark blue box looks less smooth than that in the yellow box, especially at its extremums. This resulted in a theoretical normalized switch pattern with lower contrast (dark blue curves) between the -1^{st} and the 0^{th} orders at Littrow's angle than that simulated based on the period highlighted in the yellow period.

To ensure a large enough distance between both working points, gratings with a smaller period of 770 nm were produced. Figure 3.18(a) shows the experimental (bright blue and orange curves) and theoretical (dark blue and yellow curves) normalized switch patterns of this grating design sketched in Figure 3.18(b). In the same manner as for the 790 nm period grating, the experimental switch patterns measured at two different locations on the grating surface are very similar. But the working points were easier to reach, as shown by the measurements over broader angular scans between both working points and Littrow's angle, θ_L, compared to the 790 nm period grating.

In addition, the experimental switch patterns agree quite well with the theoretical ones, which are themselves more similar and optimized than those of the 790 nm period grating. Indeed, the coefficients of extinction of both (bright blue and orange) experiemental switch patterns

presented in this figure are respectively equal to 7.37% and 7.02%. This suggests that the 770 nm period grating is smoother and more regular than that with a period of 790 nm. Thus, further experimental results presented in this thesis were obtained with 770 nm period gratings. However, it must be noticed that the increase in the slopes around the working points was in part due to the introduction of the nanoimprinting process to produce the final sample used to obtain the switch pattern shown in Figure 3.18(a). Indeed, we noticed that the profile of the photoresist gratings produced by LIL becomes modified and damaged after a prolonged exposure to fluids encountered in biosensing. That compromised the reliability and the repeatability of the measurements and could partially explain the non-negligible mismatch between the theoretical and experimental normalized switch patterns given in Figure 3.17(a). That is why the 770 nm period master gratings produced in photoresist by LIL were replicated using a nanoimprinting process adapted from [90] and detailed in section 3.3.2. That resulted in more resistant and smoother grating profiles and also in more optimized switch patterns.

In the first part of this subsection, the effect of the period on the optimization of the switch pattern was theoretically and experimentally demonstrated. A smaller period grating was demonstrated as offering a larger distance between both working points of a switch pattern whereas larger period gratings led to higher slopes.

In addition, we showed that the effect of the period on the switch pattern was not enough to explain all the discrepancies between our theoretical and experimental results. The depth is an especially crucial parameter to the switch design. The next part of the present subsection will be devoted to the effect of grating depth on the switch pattern.

Effect of the depth

The main difference between an optical switch configuration and a conventional configuration based on a grating coupler is the ratio between the depth and the period of the grating. In the case of an optical switch configuration, this ratio is higher since the depth of the grating must

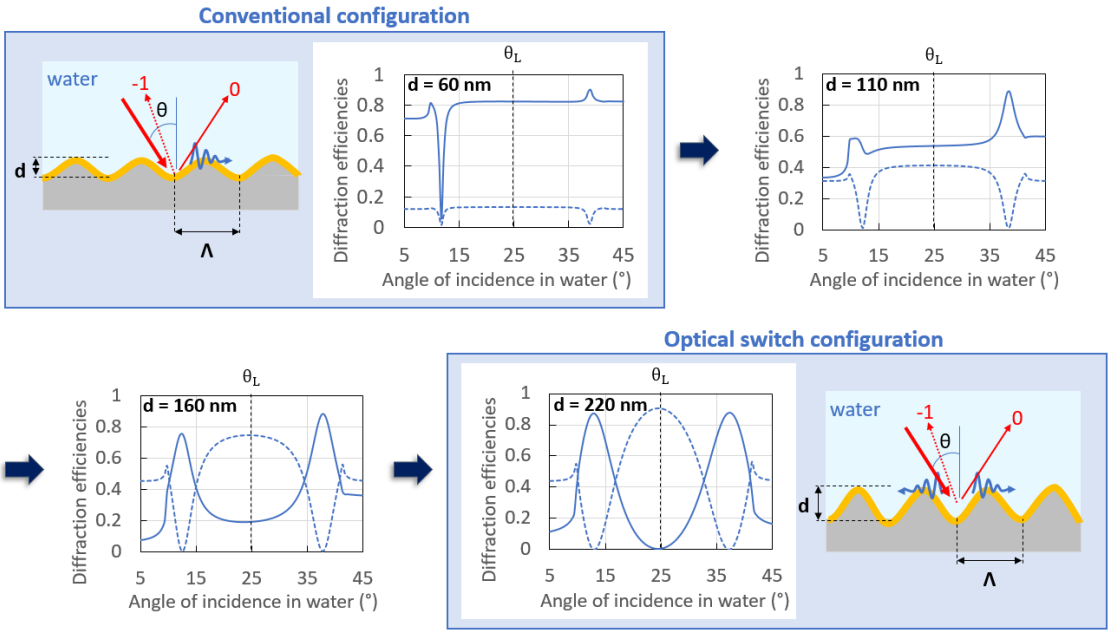

Figure 3.19: Effect of the grating depth on the optical response in water of a sinusoidal grating interacting with a p-polarized beam at a free-space wavelength λ_0=850 nm.

be high enough to enable the inter-plasmonic coupling between the backward and the forward plasmonic modes.

Figure 3.19 shows how the increase in the grating depth modifies the optical response of a 100 nm thickness gold-coated sinusoidal grating in water. As shown in this figure, the depth has a strong effect on the contrast between the -1^{st} and the 0^{th} orders, especially at Littrow's angle, θ_L. This point will be further discussed in section 4.3, but the sensitivity and the dynamic range of a detection device working in an optical switch configuration are correlated with this contrast between both diffracted orders at Littrow's angle. Thus, the depth must be rigorously chosen to optimize the switch pattern and the performance of the system.

Figure 3.20 shows three experimental normalized switch patterns measured with three different replicas produced from the same grating master. These structures also have quite identical

profiles and the same period. Yet, their depths vary slightly because of the variations in the depth losses due to the nanoimprinting process used to produce the grating replicas. Figure 3.20

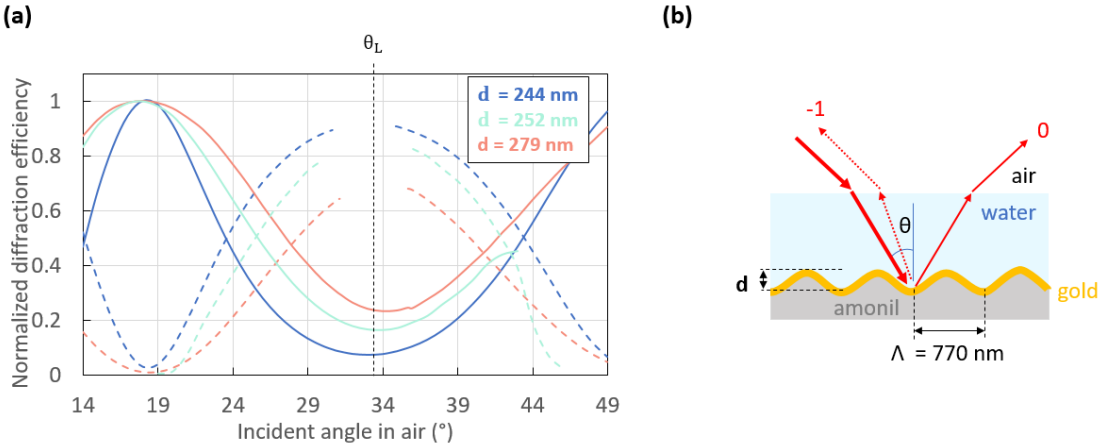

Figure 3.20: (a) Experimental switch patterns resulting from the interrogation of gold-coated sinusoidal gratings with different depths, sketched in (b), under an incident wavelength $\lambda_0 = 850$ nm at free-space over an angular scan.

shows that beyond a threshold depth, the switch pattern is no longer optimized. Indeed, the switch pattern measured with the 244 nm depth grating (dark blue curves) presents a good contrast ($C_{ext} = 7.37\%$) between the normalized power of the -1^{st} and the 0^{th} orders at Littrow's angle, θ_L. But the other deeper (252 nm and 279 nm) grating replicas from the same grating master present switch patterns with lower contrast ($C_{ext} = 16.48\%$ and $C_{ext} = 23.33\%$)at this specific angle. This demonstrates that despite the large ratio between the depth and the period of the gratings used to produce a switch pattern, the depth of the gratings must not be above a specific threshold value, or the switch pattern will no longer be optimal.

In this subsection, we showed that the depth was the main parameter differentiating a grating coupler operating in a conventional SPR configuration and in an optical switch configuration. The effect of the grating depth on the optimization of the switch pattern was theoretically and experimentally shown. But, as mentioned in subsection 3.4.2, we noticed that the profile also had a non-negligible effect on the switch pattern response. Thus, the last part of the present

subsection will be devoted to the effect of this parameter on the switch pattern.

Effect of the profile

We demonstrated in both previous parts of this subsection that the period and the depth of a sinusoidal grating must be optimized to maximize the contrast between the -1^{st} and the 0^{th} orders and the distance between the working points.

Contrary to these two parameters, the profile of the grating is harder to control. Yet, its effect on the switch pattern is strong. In the last part of the present subsection, the effect of the grating profile on the switch pattern will also be investigated.

Figure 3.21(a) shows three experimental switch patterns (bright blue, orange and yellow curves) and a simulated one (dark blue curves). The three experimental switch patterns result from the interaction of a p-polarized light beam at a free-space wavelength $\lambda_0 = 850$ nm with a sinusoidal gold-coated grating with a 770 nm period and a similar depth: 228 nm for the bright blue and 233 nm for the orange and the yellow. The theoretical switch pattern was simulated based on a perfect sinusoidal grating of the same period (770 nm) and an intermediate depth (230 nm) between those of the three gratings used to measure the experimental switch patterns. Figures 3.21(b)-(d) compare a perfect sinusoid with a period extracted from an AFM measurement of each grating used for the measurements given in Figure 3.21(a).

Despite the same period and quite identical depths, the grating with the period shown in Figure 3.21(b) yields a switch pattern (bright blue) in better agreement with the simulation than the gratings with the periods given in Figures 3.21(c) and (d) (orange and yellow switch patterns, respectively). We assume that this difference in the optical response is due to the slightly different profile of these gratings. Indeed, the period shown in Figure 3.21(b) agrees obviously better with a perfect sinusoid than those shown in Figures 3.21(c) and (d). In the same manner, the period shown in Figure 3.21(c) presents a better overlap with a perfect sinusoid than that given

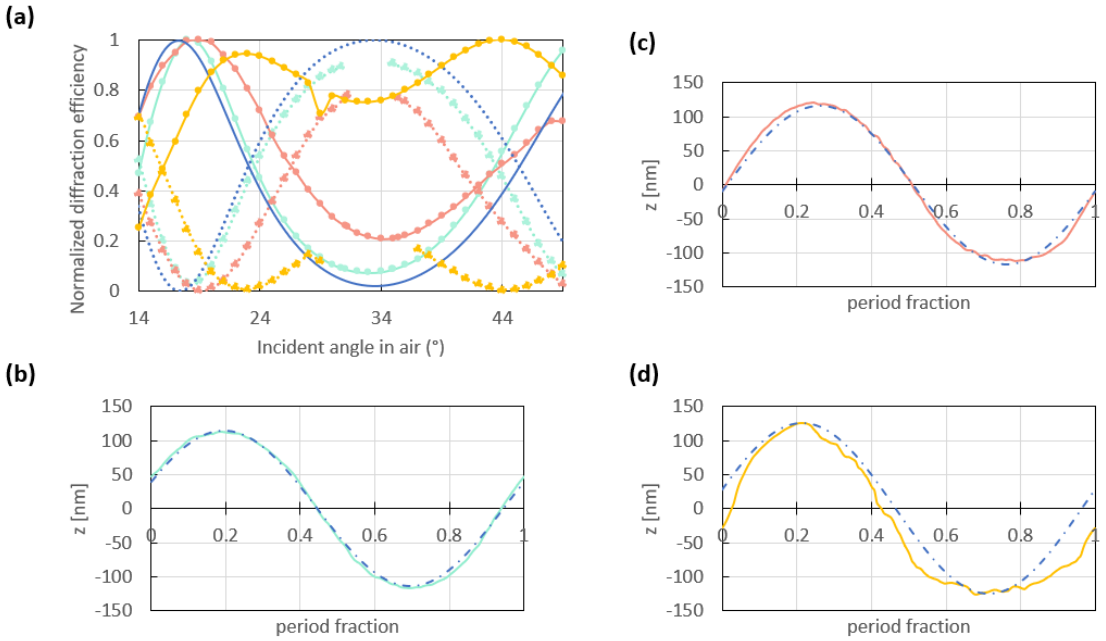

Figure 3.21: (a) Simulated (dark blue curves) and experimental (bright blue, orange and yellow curves) switch patterns resulting from the interrogation of a sinusoidal 121 nm-thick gold-coated grating with a p-polarized light beam at a free-space wavelength of λ_0= 850 nm. The theoretical switch pattern was computed via MC-grating based on a perfect 230 nm depth and 770 nm period sinusoid. The three gratings used to measure these optical switches had a 770 nm period and a similar depth of 228 nm (bright blue) and 233 nm (orange and yellow). One period extracted from AFM measurements of each grating is compared to a perfect sinusoid in (b), (c) and (d) for the bright blue, the orange and the yellow switch patterns of (a).

in Figure 3.21(d). In addition, the period shown in Figure 3.21(d) is rougher than both other periods given in Figure 3.21(b) and (c). That certainly contributed to the bad switch response provided by the grating with this profile, as shown in Figure 3.21(a) (yellow curves). This phenomenon was observed for other gratings with different depths, as shown in Figure 3.22 with deeper grating switch patterns shown in (a) and their period profiles given in (b) and (c).

In conclusion, the profile as well as the depth and the period of the gratings used in an optical switch configuration must be seriously considered to optimize their switch patterns. Indeed, we demonstrated in the present subsection that these parameters had non-negligible effects on the

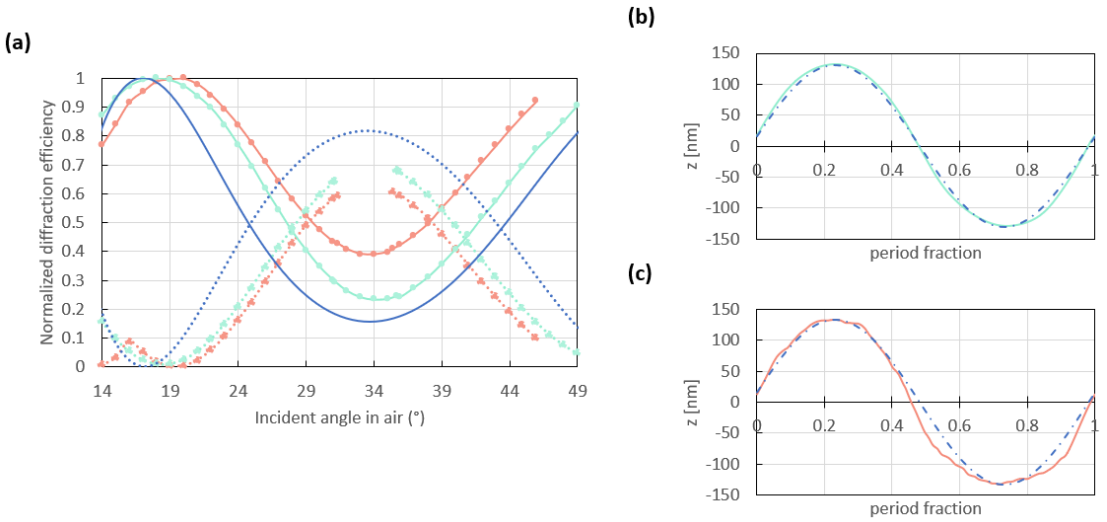

Figure 3.22: (a) Simulated (dark blue curves) and experimental (bright blue, orange and yellow curves) switch patterns resulting from the interrogation of a sinusoidal 121 nm-thick gold-coated grating with a p-polarized light beam with a free-space wavelength of λ_0= 850 nm. The theoretical switch pattern was computed via MC-grating based on a perfectsinusoid 264 nm deep and of period 770 nm. Both gratings used to measure the switch patterns have a 770 nm period and a similar depth of 261 nm (bright blue) and 267 nm (orange and yellow). One period extracted from AFM measurements of each grating is compared to a perfect sinusoid in (b) and (c) for the bright blue and the orange switch patterns of (a).

distance between the working points and the contrast between the 0^{th} and the -1^{st} orders, which affect the performance in sensing as it will be discussed in the next chapter. These parameters are fixed by the protocol of fabrication for the grating replicas.

3.5 Conclusion

In this third chapter, the principle of detection and the interest in the optical switch configuration using sinusoidal gratings as couplers were presented. This profile of grating is quite tunable and simple to produce by LIL, which is a cost-effective and rapid technique of production. This method of production is also aligned with low-cost manufacturing challenge at stake in this thesis. Yet, we showed that a prolonged exposure to fluids for the sample produced directly by LIL was swusceptible to damage.

To overcome this issue, a nanoimprinting process was developed and added to the initial protocol of grating fabrication. This supplementary step was especially appealing for low-cost and mass production since it provided many reusable samples from each initial grating master produced by LIL. In addition, we showed that the grating replicas produced by this nanoimprinting process were less rough than their initial grating master produced by LIL and provided more optimized switch patterns.

Another part of this chapter investigated theoretically and experimentally the effects of the grating design on the performances of the grating especially in the optical switch configuration. We showed that the depth of the gratings used as couplers was the main difference between a conventional and an optical switch configuration. The effects induced by the period and the profile shape of the grating on the switch pattern were as well demonstrated and studied. Their effects on the slope around each working point and the distance between them, which are correlated to the performance achievable by the sensors working in such a configuration, were especially highlighted.

In the next chapter, the detection measurements performed with the optimized grating design produced and optimized as previously described and explained will be presented for small bulk RI variations. The optical switch will be demonstrated as a method of detection and its specific advantages will be presented.

Chapter 4

The optical switch as a method of detection

4.1 Introduction

This fourth chapter divided into two parts is devoted to the experimental detection of small RI variations in the bulk performed with the grating structures described in section 3.4.2 in the previous chapter. In the first part, the arrangement of the setup operating in the optical switch configuration to perform the detection will be described and discussed. In the second part, the proof-of-concept of the optical switch configuration as a method of detection will be supported by an experimental demonstration of bulk sensing for small variations in RI under an intensity interrogation. In this last part, the interest in the differential measurement will be as well discussed based on experimental results.

4.2 Setup

In the present thesis, several sensing platforms were designed and tested to enable the circulation of the fluids over the grating coupler used as a detection surface. The main challenges were to

prevent the dead volumes and to enable a front-side interrogation of the grating to perform real-time measurements. These platforms were integrated into a setup designed to collect and monitor the power in both 0^{th} and -1^{st} diffracted orders. The present section describes and explains choices relative to the design of these first sensing platforms.

4.2.1 Sensing platform

The first experimental measurements of the switch patterns presented in section 3.4.2 were performed in a tank, sketched in Figures 4.1(a)-(b), without any integrated fluidic system. This tank helped to identify gratings with a good experimental optical switch response in water and to perform the first detection experiments for small RI variations in the bulk by adding a few drops of glycerol to the fluid. But to investigate further, a fluidic system to exchange the fluids in real-time was needed. Moreover, the large fluidic volume of the tank was a main drawback and needed to be reduced to remain aligned with the low-cost challenge at stake in this thesis.

Thus a new design with a 0.75mm-height circular flow cell, sketched in Figures 4.1(c)-(d), was elaborated and fabricated. As mentioned in our article [149], this custom fluidic cell "was closed by a PETG (polyethylene terephthalate glycol) lid with a machined trench housing a 20.35 mm diameter, 1.78 mm-thick O-ring to seal and delimit the sensing area. The lid was drilled with two holes through which peek tubing was threaded and glued (Krazy Glue^{TM} from Canadian Tire, Ottawa, Canada), enabling solutions to be injected using a syringe pump. A metal base was used to support the grating, and a flat square metal flange was used to secure the PETG window to the base by four screws, ensuring that a uniform pressure was applied by the O-ring to the substrate. The grating area was designed to be smaller than the diameter of the O-ring to ensure there was no contact between the O-ring and the sensing surface." This shape was chosen because it was easier to fabricate. Yet, it resulted in poor fluidic exchanges, as will be discussed in section 4.3. That motivated the modification of the shape and the height of this flow cell for the preliminary biosensing assays presented in the next chapter, as will be discussed in section 5.2.

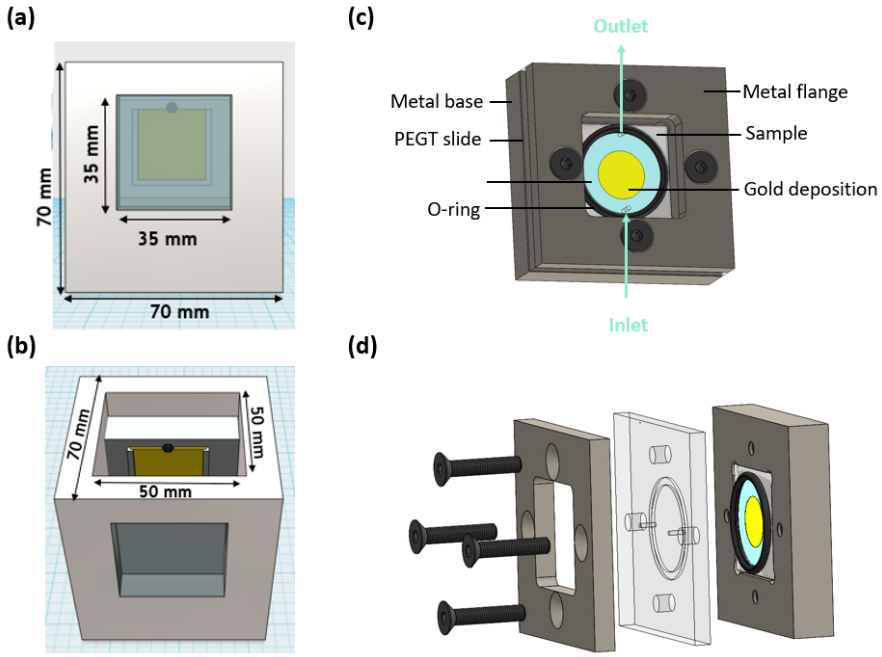

Figure 4.1: (a) Front view and (b) top view of the initial Teflon tank designed to perform the first switch pattern measurements. The yellow square represents the gold-coated sample and the blue transparent square the window through which the grating was interrogated. (c) Front view and (d) exploded view of the first fluidic system to perform measurements in real-time. The schematic of the sensor given in (c) is adapted from [149]. The colour of the inlet and outlet was changed. Adapted with permission from https://doi.org/10.3390/s23031188. Copyright © 2023 by the authors. Licensee MDPI, Basel, Switzerland. The Authors, licensed under a Creative Commons Attribution (CC BY) license.

It must be noticed that for the fluidic systems shown in Figures 4.1(c)-(d), the circulation of the fluids was chosen to be in the same direction as that of the grating peaks and valleys to promote the interaction of the chemical compounds and biological species along the grating.

4.2.2 Interrogation setup

The sensing platform described in the previous subsection was integrated into an interrogation setup sketched in Figure 4.2. The reference and the manufacturer of each item presented in this Figure are summarized in Table 7.20 (Appendix chapter). A 850 nm wavelength laser diode was used as a light source to probe the grating used as a coupler in the detection device. This

choice of wavelength was motivated by the large availability of these laser diodes on the market and their compatibility with the biological targets used, which were probed by its beam on the detection surface.

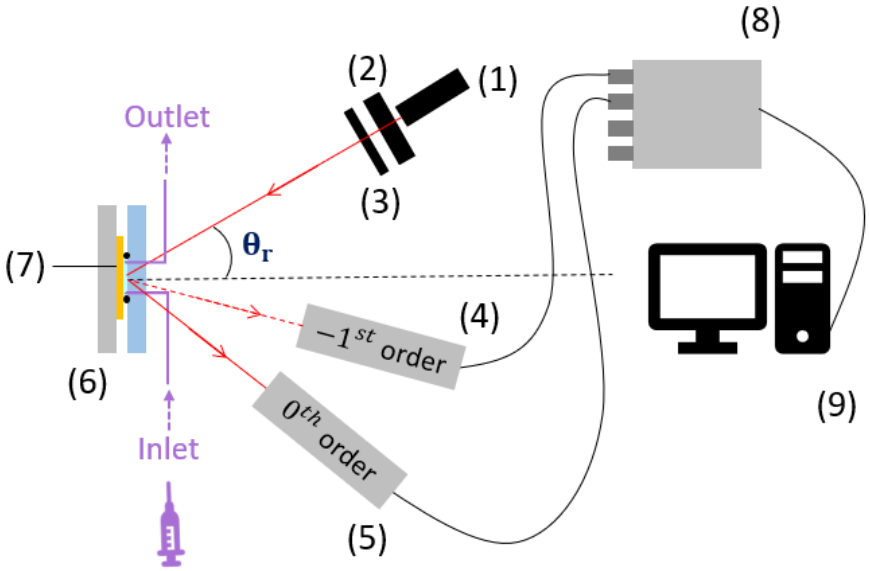

Figure 4.2: Setup used to perform the measurements, comprising an 850 nm wavelength laser diode (1), a polarizer (2), an aperture (3), and two photodiodes (4) and (5) to measure the power in the -1^{st} (dashed red line) and the 0^{th} (solid red line) orders diffracted from the gold-coated grating (6) placed within a flow cell (7) into which fluids are injected via peek tubing interfaces (purple) connected to a syringe pump. A DAQ (data acquisition) device (8) and a computer (9) were used to record the measurements. This figure is extracted from [149]. Reprinted with permission from https://doi.org/10.3390/s23031188. Copyright © 2023 by the authors. Licensee MDPI, Basel, Switzerland. The Authors, licensed under a Creative Commons Attribution (CC BY) license.

Moreover, using infrared (IR) light sources enables using higher grating periods, which were easier to produce with a high depth/period ratio. In addition, Phedran and Maystre demonstrated in 1974 that working at short wavelengths induced higher sensitivity to profile distorsion (non perfect sinusoid profile) and variations in depth [141]. The choice of an IR light source was also justified to prevent a bad agreement between the computed and the experimental switch patterns resulting from the interaction of a p-polarized beam and a grating with an optimized

design, overall based on the comparison carried out in subsection 3.4.2 in the previous chapter.

A polarizer (2) was used to ensure p-polarization for the incident light beam and an aperture (3) to minimise background light. The grating interrogated by the p-polarized collimated light beam of this source was placed inside the flow cell described in the previous subsection, represented by item (6) in Figure 4.2. The solutions were injected through this flow cell by polyetheretherketone (peek) tubings (inlet and outlet), which were fixed to needles of syringes controlled by a pump (11 pico plus elite single syringe) from Harvard Apparatus.

A rotation stage holding the flow cell was used to set the angle of incidence at one of the working points, as shown in Figure 4.3. As described in our article [149], "the grating inside the flow cell was aligned along the central rotation axis via an xy stage", as shown in Figure 4.3. "Both 0^{th} and -1^{st} orders power were collected by two 5×5 mm^2 Si-based photodiodes, which were fixed to tracks connected to two other rotation stages with their axes of rotation aligned with those of the rotational stage controlling the cell orientation. Photodiode current was converted to voltage using a transimpedance circuit giving an output signal (voltage) proportional to the incident optical signal. A module of acquisition was used to collect the measurement data from each photodiode and a computer was used to record this data in real-time. Labview software was used to perform data acquisition from both photodiodes."

4.3 RI sensor

4.3.1 Preparation of solutions

The final grating design chosen, presented in section 3.4.2, was optimized for operation in water. To carry out the proof-of-concept of the optical switch as a method of detection for small RI variations in the bulk, DI was also used as the reference medium (s_0) to establish the baseline of the sensorgrams, which will be presented in the next subsection. Three other solutions (s_1, s_2, and s_3) comprised of a mixture of DI and glycerol were prepared to produce RI increments

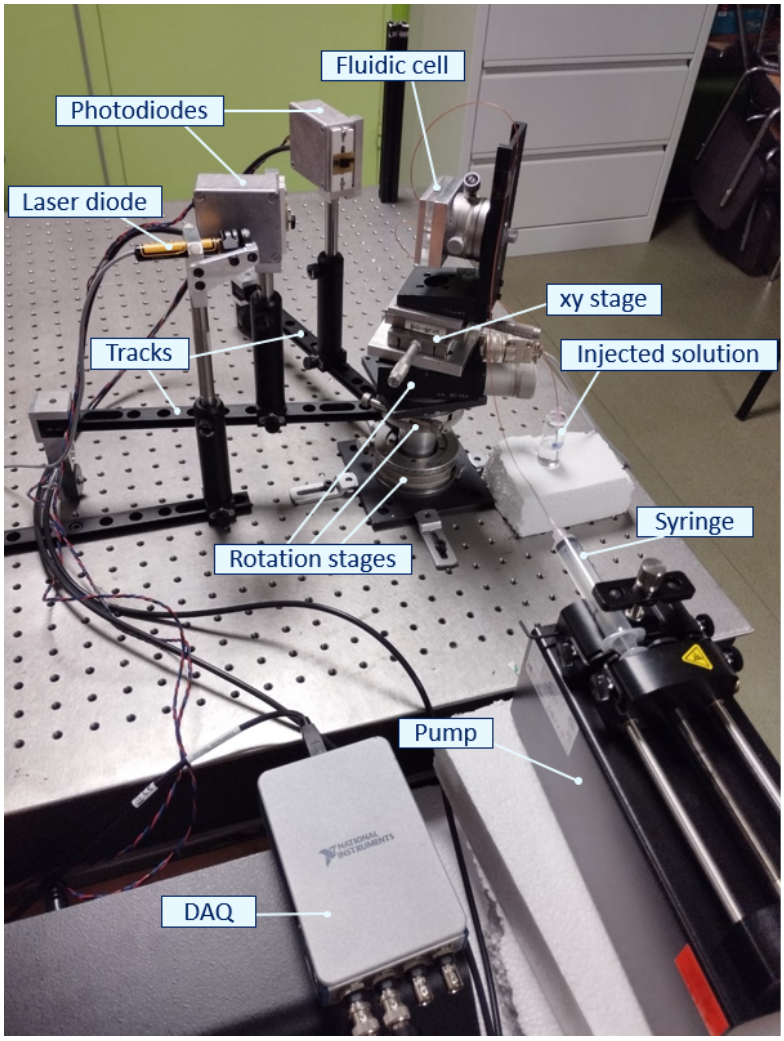

Figure 4.3: Picture of the setup to measure the switch patterns and perform real-time sensing measurements.

of about 10^{-3} RIU. The features of the glycerol used and the details relative to the preparation of each solution are reported in Tables 7.21 and 7.22 (Appendix chapter). The RI of the solutions s_0, s_1, s_2, and s_3 were respectively 1.3211, 1.3265, 1.3283, and 1.3311, as measured using an instrument based on a prism coupler (Metricon, Model 2010, Prism 200-P1) at $\lambda_0 = 1312$ nm. Based on the dispersion coefficients of water and glycerol reported in [164] and Sellmeier dispersion equation given below, these RI were calculated as 1.3274, 1.3326, 1.3347, 1.3368 at λ_0

= 850 nm:

$$RI(\lambda)^2 = 1 + \frac{s\lambda^2}{\lambda^2 - \lambda_s^2} \tag{4.1}$$

where s and λ_s are the dispersion coefficients.

4.3.2 Proof-of-concept

To demonstrate detection in the optical switch configuration, the four solutions (s_0, s_1, s_2, s_3) prepared as detailed in the previous subsection were sequentially injected over the gold-coated grating replica with the profile given in Figure 4.4. This replica was placed inside the sensing platform with an integrated fluidic system described in subsection 4.2.1. Figures 4.5 and 4.6 present both sensorgrams obtained with the angle of incidence sequentially fixed at the left and right working points. Table 7.23 (Appendix chapter) summarizes the protocol, which was applied to carry out these measurements.

The solutions s_0, s_1 and s_2 were injected twice to demonstrate the repeatability of our measurements. Table 4.1 and 4.2 give the mean (time-averaged) and the standard deviation of the differential output voltage for the injection time of each solution represented in yellow in Figures 4.5 and 4.6. At both working points, data shows that the differential output voltage was recovered for each injection of the same solution. That demonstrates the repeatability of the

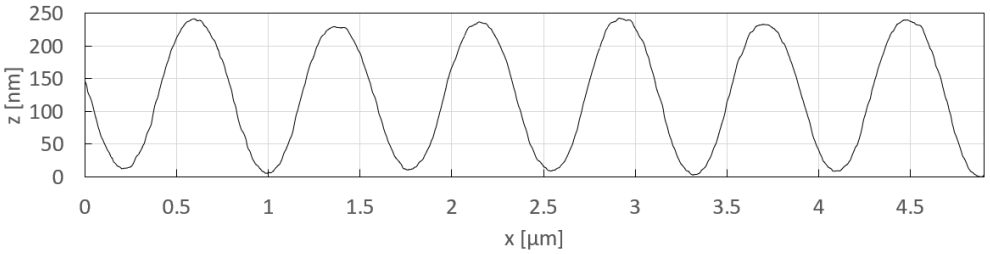

Figure 4.4: AFM profile of the corrugated gold-coated grating replica used to perform the measurements. This Figure is adapted from [149]. A box of colour has been removed. Adapted with permission from https://doi.org/10.3390/s23031188. Copyright © 2023 by the authors. Licensee MDPI, Basel, Switzerland. The Authors, licensed under a Creative Commons Attribution (CC BY) license.

measurements.

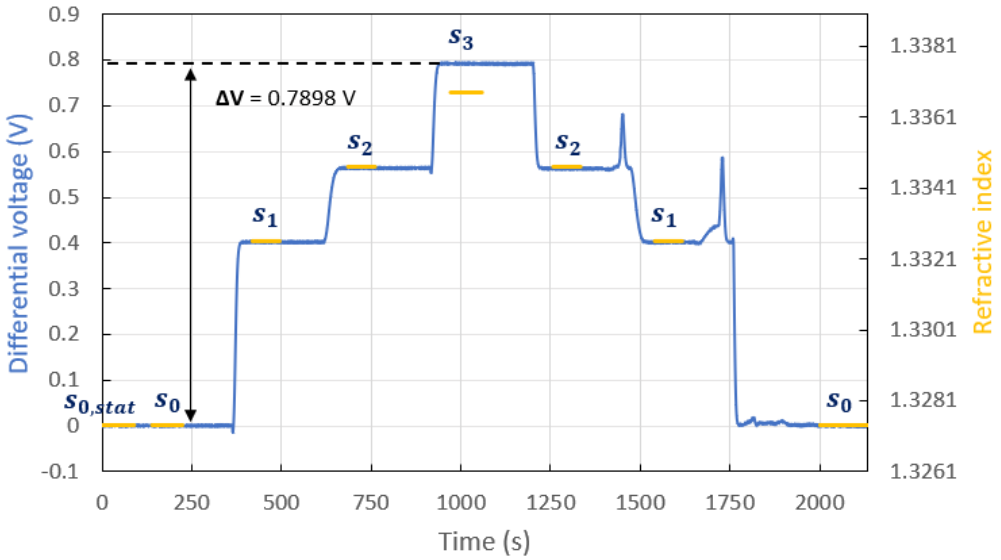

Figure 4.5: Differential measurement (blue curve) resulting from the power variations between the 0^{th} and the -1^{st} orders of the diffraction grating interrogated by a p-polarized beam at free-space wavelength $\lambda_0 = 850$ nm at left working point, θ_l. The yellow lines represent the RI of the solution injected during the measurements. The solution denoted $s_{0,stat}$ at the beginning of the sensorgram is associated to the measurement of the differential output signal under static conditions (pump turned off) with the flow cell filled by the solution s_0. This Figure is extracted from [149]. Reprinted with permission from https://doi.org/10.3390/s23031188. Copyright © 2023 by the authors. Licensee MDPI, Basel, Switzerland. The Authors, licensed under a Creative Commons Attribution (CC BY) license.

In addition, Figures 4.5 and 4.6 obviously show a strong correlation between the differential output voltage measured and the RI of the solutions injected inside the detection device. Indeed, each yellow line associated with the solutions shows a good overlap with the differential output voltage. Figures 4.7(a) and (b) support this observation by demonstrating a linear correlation between the RI of the solutions injected inside the detection device and the (time-averaged) mean of the differential output voltage associated with each of them at the left and right working points, reported in Tables 4.1 and 4.2.

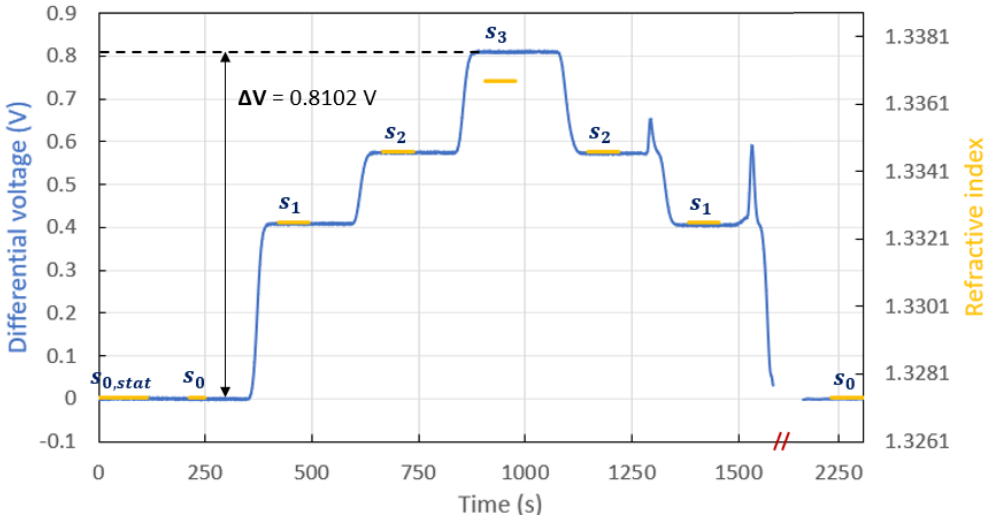

Figure 4.6: Differential measurement (blue curve) resulting from the power variations between the 0^{th} and the -1^{st} orders of the diffraction grating interrogated by a p-polarized beam at free-space wavelength $\lambda_0 = 850$ nm at right working point, θ_r. The yellow lines represent the RI of the solution injected during the measurements. The solution denoted $s_{0,stat}$ at the beginning of the sensorgram is associated to the measurement of the differential output signal under static conditions (pump turned off) with the flow cell filled by the solution s_0. The double red dash indicates a time break in the time axis.

Solution	RI ($\lambda_0 = 850$ nm)	Mean (V)	Standard deviation (mV)
$s_{0,stat}$	1.3274	0.00062	0.18
s_0	1.3274	0.00083	0.15
s_1	1.3326	0.40162	0.14
s_2	1.3347	0.56299	0.11
s_3	1.3368	0.79070	0.14
s_2	1.3347	0.56193	0.14
s_1	1.3326	0.40099	0.24
s_0	1.3274	0.00037	0.39

Table 4.1: RI at $\lambda_0 = 850$ nm, mean (time-averaged) differential output voltage, and standard deviation over time of the differential output voltage for each solution injected, as measured at the angle of incidence θ_l (left working point). The solution denoted $s_{0,stat}$ at the beginning of the sensorgram is associated to the measurement of the differential output signal under static conditions (pump turned off) with the flow cell filled with the solution s_0.

The slight mismatch observed for the solution s_3 between the differential output voltage and its RI at both working points is also likely due to an error in the weight of glycerol or the volume of DI used to prepare this solution, as the agreement for the other solutions between their RI

Solution	RI (λ_0 = 850 nm)	Mean (V)	Standard deviation (mV)
$s_{0,stat}$	1.3274	0.00059	0.30
s_0	1.3274	-0.00025	0.27
s_1	1.3326	0.40876	0.25
s_2	1.3347	0.57487	0.28
s_3	1.3368	0.81001	0.26
s_2	1.3347	0.57303	0.26
s_1	1.3326	0.40529	0.31
s_0	1.3274	-0.00245	0.60

Table 4.2: RI at λ_0 = 850 nm, mean (time-averaged) differential output voltage, and standard deviation over time of the differential output voltage for each solution injected, as measured at the angle of incidence θ_r (right working point). The solution denoted $s_{0,stat}$ at the beginning of the sensorgram is associated to the measurement of the differential output signal under static conditions (pump turned off) with the flow cell filled with the solution s_0.

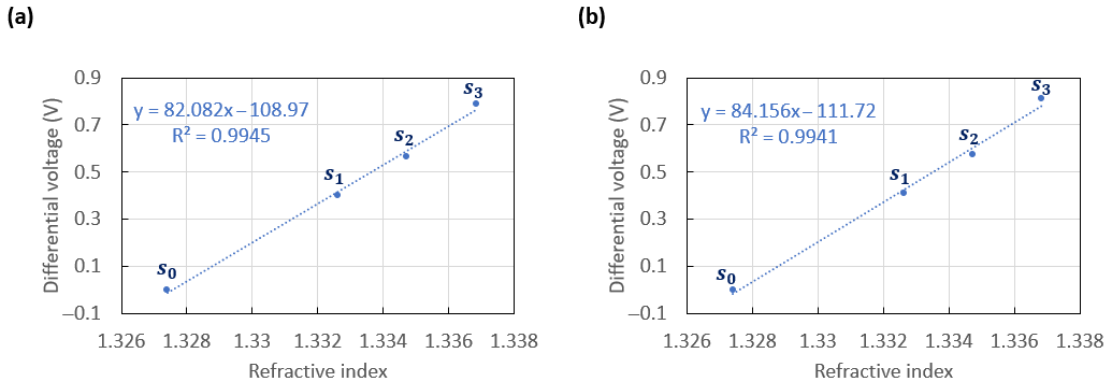

Figure 4.7: Linear correlation at (a) the left and (b) the right working points between the differential output voltage and the RI of the injected solution given in Figure 4.5 for (a) and in Figure 4.6 for (b). This Figure is extracted from [149]. Reprinted with permission from https://doi.org/10.3390/s23031188. Copyright © 2023 by the authors. Licensee MDPI, Basel, Switzerland. The Authors, licensed under a Creative Commons Attribution (CC BY) license.

and the differential signal is excellent.

The sensorgrams given in Figures 4.5 and 4.6 were obtained with the circular flow cell presented in subsection 4.2.1. We believe that the larger transient variations at the end of the second injections of the solutions s_2 and s_1 are due to dead volumes which were set into motion by the repeated turn on and off of the pump. Indeed, these variations resulted in an increase

in the differential measurement. Yet, an increase in the differential output signal indicates an increase in the RI of the sensing medium. These larger transient variations can also have been induced by residual solutions with higher RI previously injected.

A similar but longer effect was observed at the beginning of the last injection of the solution s_0 for the sensorgram given in Figure 4.6. This noisy portion of signal was removed by a break in the time axis (double red dash) because it was not representative of the system noise. Yet, this instability is reflected in the standard deviation of the differential output voltage measured, which is at least 2-fold above those of the other injections, as shown in Table 4.2.

A similar but weaker effect was observed for the last injection of the solution s_0 in the sensorgram given in Figure 4.5. That resulted as well in a standard deviation more than 2-fold above those of the previous injections. This observation motivated the change of the circular flow cell into an oval channel shape to improve flow of the fluids and the stability of the signal. In addition, a poor exchange of fluids can introduce errors into biosensing measurements by causing unexpected interactions between biomolecules that are sequentially injected.

Thus, except for this injection, the differential signal was quite steady at 0.1 mV for the measurements at θ_l and at 0.3 mV at θ_r, as shown in Tables 4.1 and 4.2. The average of the standard deviations, δ_a, was also equal to 1.88 $\times 10^{-1}$ mV for the differential signal presented in Figure 4.5 and 3.17 $\times 10^{-1}$ mV for that in Figure 4.6.

The largest changes in the differential signal, ΔV, reached between the solutions s_0 and s_3 were quite similar in both Figures 4.5 and 4.6. They were equal to 0.7898 V and 0.8102 V at θ_l and θ_r.

Assuming that the minimum SNR required for reliable detection would be equal to two, LOD respectively equal to 4.48 $\times$ 10^{-6} RIU at θ_l and 7.37 $\times$ 10^{-6} RIU at θ_r were achieved, as defined

below:

$$LOD = 2 \cdot \frac{\delta_a}{\Delta V} \cdot (RI_{s_3} - RI_{s_0}) \tag{4.2}$$

where RI_{s_3} and RI_{s_0} represent the RI of the solutions s_3 and s_0. The performance achieved at each working point was similar although the LOD reached for the sensorgram measured at θ_r was slightly worse. This is mostly due to the average of the standard deviations being slightly higher (3.17 mV) compared to that obtained at θ_l (1.18 mV). These performances are sufficiently competitive for disease detection in complex fluids [104, 121].

Similar sensorgrams (Figure 7.1 in Appendix) were initially performed with grating masters inside the same flow cell, but the performances achieved were 10-fold lower than those presented above, which supported interest in the nanoimprinting process to enhance the performance of the sensors as smoother and more resistant samples.

4.3.3 Noise and differential measurement

The optical switch configuration allows a differential measurement between the power of two diffracted orders monitored by a couple of photodiodes. The main interest in this specific configuration, compared to the conventional ones described in subsection 2.2.2, is the cancellation of the drift and noise common to both monitored orders. Figure 4.8 shows the time traces of the powers measured for the 0^{th} (bright blue curve) and -1^{st} (orange curve) orders and the differential output signal (dark blue curve). This sensorgram was obtained during four sequential injections of buffer comprised of phosphate buffer saline (PBS) and DI (preparation detailed in subsection 5.3.3 in the next chapter). Contrary to the differential signal, the 0^{th} and -1^{st} orders show an obvious drift. This observation is supported by data reported in Table 4.3. Indeed, the standard deviation of the differential signal is 1.47- to 2-fold lower than that of the 0^{th} and -1^{st} orders. This demonstrates that differential measurements improve the performance of the detection system by reducing the common drift between both monitored orders.

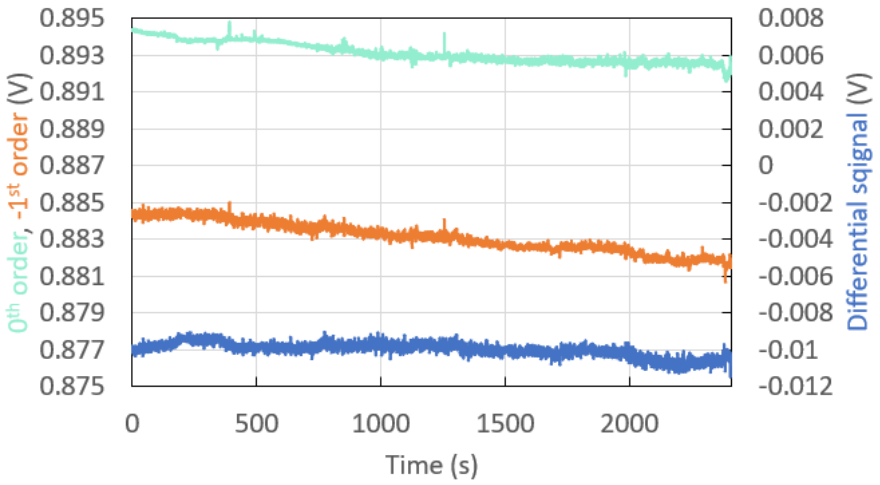

Figure 4.8: Time traces of the 0^{th} (green) and -1^{st} (orange curve) orders and the differential output signal (dark blue curve) obtained during four sequential injections of a buffer solution.

Signal	Mean (V)	Standard deviation (mV)
0^{th} order	0.88557	0.82
-1^{st} order	0.88989	0.56
Differential	-0.00432	0.38

Table 4.3: Mean (time-averaged) and standard deviation over time of both 0^{th} and -1^{st} diffracted orders and the differential output signal during four sequential injections of a buffer solution, shown in Figure 4.8.

Signal	Mean (V)	Standard deviation (mV)
0^{th} order	2.81716	88.09
-1^{st} order	2.14836	75.60
Differential	0.66880	13.86

Table 4.4: Mean (time-averaged) and standard deviation over time of both 0^{th} and -1^{st} diffracted orders and the differential output signal during injection of the solution s_1, shown in Figure 4.9.

Yet, the interest in differential measurements becomes clearer with the introduction of artificial noise into the detection system. Figure 4.9 shows time traces of the powers measured for both 0^{th} and -1^{st} diffracted orders and the differential output signal, while the fluidic system was manipulating during the injection of the solution s_1. The traces associated with the 0^{th} and -1^{st} orders present obvious variations over time, while the differential signal remains quite steady. These observations are supported by table 4.4. Indeed, the standard deviation associated to the

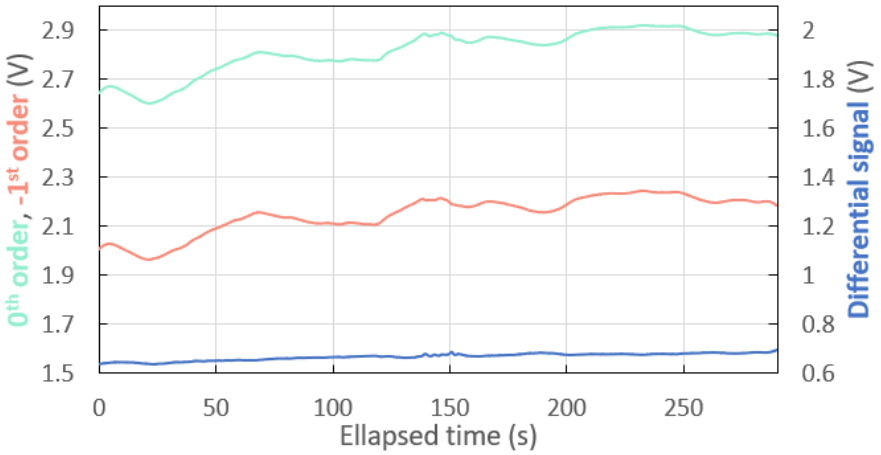

Figure 4.9: Time traces of the 0^{th} (green) and -1^{st} (orange curve) orders and the differential output signal (dark blue curve) obtained during injection of the solution s_1 with artificial noise affecting the system. The colours of the traces were modified. This Figure is adapted from [149]. Adapted with permission from https://doi.org/10.3390/s23031188. Copyright © 2023 by the authors. Licensee MDPI, Basel, Switzerland. The Authors, licensed under a Creative Commons Attribution (CC BY) license.

differential signal was approximately 8-fold lower than those of the 0^{th} and -1^{st} orders. This shows that the differential measurement enables a non-negligible decrease of the drift and the noise by the cancellation of those common to both monitored orders, resulting in a better SNR and so in improved performance.

4.4 Conclusion

In this fourth chapter, differential sensing was successfully performed with replicated plasmonic gratings interrogated in the optical switch configuration for the detection of small RI variations in the bulk. The repeatability of the measurements and the linear correlation between the RI of the injected solutions and the differential output signal measured at both working points were demonstrated. A similar LOD in the range of 10^{-6} RIU was achieved at each working point.

The differential measurements were demonstrated as enhancing the performance of the detection

system by reducing the common drift affecting both monitored orders. This interest was especially highlighted with the introduction of artificial noise into the detection system. In addition, the interest in the nanoimprinting process for improving the performance was highlighted by the comparison of sensorgrams performed with grating replicas and grating masters (presented in section 7.3 of the Appendix). Thus, high performances were achieved with a simple and low-cost setup, which can be a competitive tool of detection.

Yet, punctual large transient variations were observed in the sensorgrams obtained. They were certainly due to the shape and the volume of the flow cell.

In the next chapter, preliminary biological assays were implemented and investigated with the same setup, but with a new flow cell design modified to minimise dead volumes.

Chapter 5

Biosensing

5.1 Introduction

In the previous chapter, the optical switch configuration was demonstrated as a method of detection. Yet, the final goal of this thesis was to propose a new plasmonic sensor for the detection of biological species. This last chapter presents and discusses the preliminary assays of biosensing performed with routinely used biospecific pairs in the same interrogation system as that presented in section 4.2 in the previous chapter.

The preliminary assays presented in this chapter are based on immunosensing. In other words, antibodies and their associated antigens are used as biorecognition agents and targeted analytes. Such biospecies react selectively. Thus, either of them can be used to functionalize the detection surface and selectively immobilize the other.

This approach was preferred to aptamers [165] or DNA [166, 167] due to closer resemblance to ELISA and draw a clearer parallel with this technique of detection. The assays presented in this chapter are also based on interactions between bovine serum albumin (BSA), human serum albumin (HSA), anti-BSA and anti-HSA. These biospecies correspond to two antigens (BSA,

HSA) and two antibodies (anti-BSA, anti-BSA), which are routinely used to demonstrate detection devices in clinical and industrial fields. The BSA (resp. HSA) and the anti-BSA (resp. anti-HSA) form a biospecific pair. Thus, a biorecognition layer of anti-BSA immobilizes BSA but not HSA. Analogous principle of detection can be used with anti-HSA and HSA. This specific detection of the targeted analyte will be demonstrated along with negative controls. Additionally, the change in flow cell geometry to minimise dead volumes will also be discussed based on experimental results.

5.2 Sensing platform

As mentioned in subsection 4.3.2 in the previous chapter, punctual large transient variations were observed in the sensorgrams performed with the fluidic integrated system described in section 4.2.1. We assumed that they mainly resulted from the combination of three factors:

- the high volume of the flow cell
- the high flow rate (160 μL/min) required to renew the whole solution volume inside the flow cell each minute
- the setting into motion of dead volumes located on the right and the left from the central fluidic stream inside the circular flow cell induced by the sequential turn on and off of the pump

To prevent this effect, the height and the inner diameter of the flow cell were first reduced to 0.10 mm and 10 mm.

This reduction of the flow cell dimensions was also motivated by a second reason: the high cost of biological products. Indeed, biological products such as antibodies and antigens are very expensive, especially if they are bought in complex matrices such as physiological fluids. The biodetection applications such as the diagnosis of infectious diseases also require detection devices with a low-volume flow cell to avoid both the waste of these products and the need for

collecting high volumes of physiological fluids from patients to perform the relevant analysis, and to remain cost-effective.

In addition, this reduction of the flow cell dimensions was in part supported by theoretical and experimental studies led by Lynn's team, which demonstrated that the geometry of the flow cell of such a detection system had an effect on their performance [168]. They showed that a simple reduction of the flow cell height induced a decrease by a factor of 4 in the LOD.

Despite this improvement, a few large transient variations of signal were still observed, as it will be shown in section 5.4. We assumed that they were due to the circular geometry of the flow cell, which may further the dead volumes. To reduce them, the circular flow cell was then replaced by a more elongated shape more similar to a channel, as shown in Figures 5.1(a) and (b). That resulted in smoother sensorgrams, as it will be shown in section 5.4.

Yet, based on Deng's study on a curved top-wall flow cell [169], this latter flow cell design could still be optimized. Indeed, this study demonstrated that the uniformity of analytes binding on a sensing surface could be improved by a curve top-wall flow cell. This avenue could be interesting to explore since the fabrication of such a flow cell is based on elastomer replica molding technique, which is cost-effective and easy to implement.

Another possibility for this sensing platform would be to design a PETG window with several channels, as used in Dostalek's work [90]. In this way, several sensing channels could be simultaneously interrogated with grating areas functionalized with different probes. This would enable multiplexing, and could help to mitigate non-specific binding on the detection surface and improve the accuracy of the detection system.

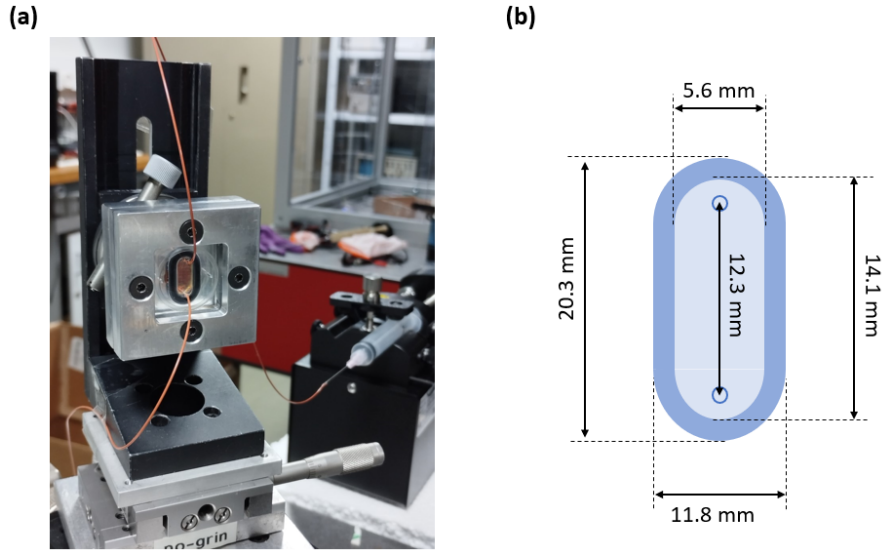

Figure 5.1: (a) Picture and (b) sketch of the flow cell with an elongated channel shape. In the sketch, the dark blue contour represents the groove inside which the O-ring was placed to seal the flow cell. The holes on the top and the bottom of the flow cell were drilled to thread and glue the PEEK tubing used as the inlet and the outlet for the injection of the fluids inside the flow cell.

5.3 Solution preparation and functionalization

5.3.1 Coupler cleaning

Before performing the biosensing assays, the grating replicas were thoroughly cleaned. First, they were placed in sequential baths of acetone for 30 minutes, then in 2-isopropanol (IPA) and DI, both for 5 minutes. Next, the replicas were placed in a UV Ozone cleaner (Novascan Technologies) with the lamp on for 30 minutes to remove any organic residue.

5.3.2 Static pre-functionalization

To perform biosensing with the setup described in section 4.2.2 working in the optical switch configuration, the surface of the grating replicas needed to be functionalized with biorecognition agents (proteins). To avoid the denaturation of these proteins on the gold detection surface, a self-assembled monolayer (SAM) was first formed by an overnight incubation of the grating

replicas in an alkanethiol solution, as sketched in Figure 5.2(a). This solution was prepared by dissolving 1mM of 16-mercaptohexadecanoic acid (16-MHA) into IPA.

5.3.3 Dynamic functionalization

The next part of the functionalization was performed with the grating replica placed inside the first sensing platform (with a circular flow cell) described in section 5.2. First, a buffer solution was injected through the detection device as the reference solution to establish the baseline in the sensorgrams (given in the next section). Phosphate buffer saline 0.01 M, pH 7.4 (PBS) was obtained from Sigma-Aldrich. PBS solution was prepared from the package by dissolving containing salts in 1 L of DI producing a buffer of the following constitution: 0.01 M phosphate buffer saline, 0.138 M NaCl, and 0.0027 M KCl (according to the manufacturer).

Then, a (1:1) solution of N-(3-Dimethylaminopropyl)-N'-ethylcarbodiimide hydrochloride (EDC)/N-Hydroxysuccinimide (NHS) from Sigma-Aldrich was injected through the sensing platform for

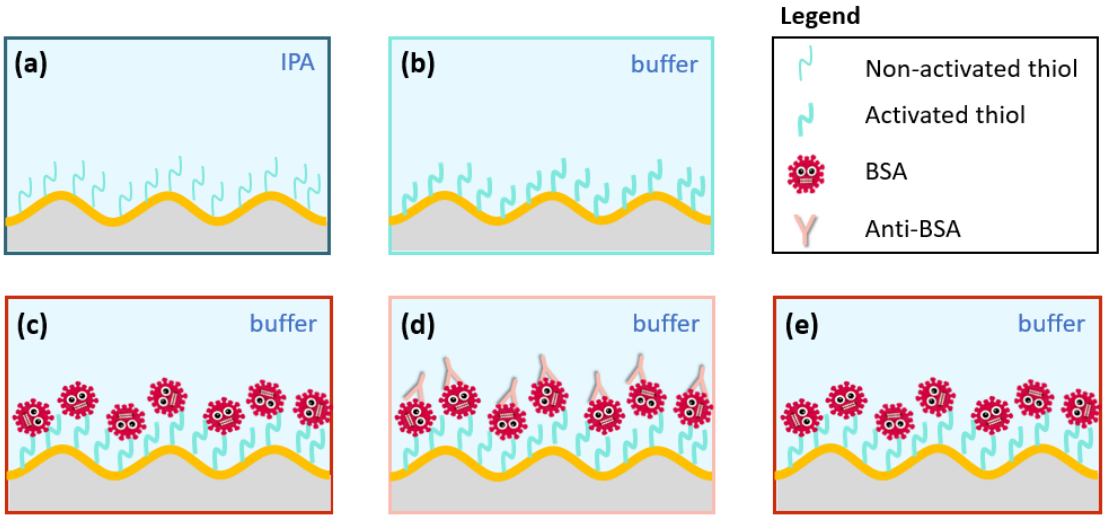

Figure 5.2: Sketches of (a) the incubation of the grating replica in a 16-MHA solution, (b) the activation of the carboxylic groups terminating the SAM layer, (c) the functionalization of the grating replica surface with BSA, (d) the immobilization of the anti-BSA and (e) the regeneration of the detection surface. All these sketches are not to scale.

10 minutes, followed by incubation for 10 minutes to activate the carboxylic groups (COOH) terminating the SAM layer on the surface of the grating replica, as sketched in Figure 5.2(b).

After a flush of buffer, the detection surface was functionalized by an injection of buffer carrying BSA proteins (Abcam) for 10 minutes, followed by an incubation for 10 minutes, as sketched in Figure 5.2(c).

After another injection of buffer to flush non-reacted proteins, a solution of buffer carrying anti-BSA (Abcam) antibodies was injected through the sensing platform. The anti-BSA were immobilized on the BSA layer, as sketched in Figure 5.2(d), and detected by the interrogation setup (as shown in the sensorgram given in the next section).

Finally, regeneration of the detection surface was carried out by an injection of a 1% sulfate dodecyl sodium (SDS) for 10 minutes followed by incubation for 10 minutes, as sketched in Figure 5.2(e). The details (reference, manufacturer) relative to the bioassays products mentioned above and their preparation are summarized in tables in section 7.4 (Appendix chapter).

5.4 Preliminary assays

To demonstrate operation of the optical switch configuration for biosensing, preliminary assays were performed at a continuous flow rate of 50 μL/min with BSA used as the biorecognition agent and anti-BSA as the targeted analyte. The BSA and anti-BSA solutions were prepared with a concentration of 30.5 μg/mL and 25 μg/mL. The protocol of functionalization, described in section 5.3, was applied over the same grating replica used to perform the sensorgrams presented in the previous chapter for bulk sensing inside the circular flow cell with reduced dimensions (an inner diameter of 10 mm instead of 20 mm) described in section 5.2.

Figure 5.3 shows the sensorgram measured with the setup working in the switch configuration

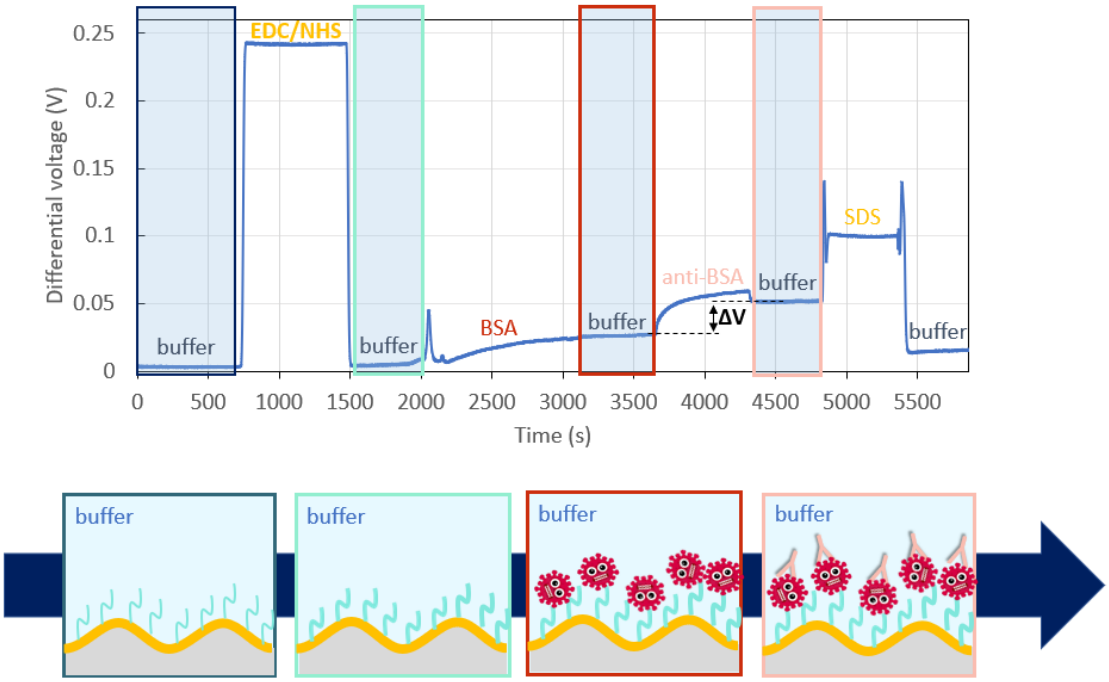

Figure 5.3: Complete cycle for the direct detection of anti-BSA by BSA immobilized on a gold-coated sinusoidal grating of period 770 nm and depth 228 nm. The grating was interrogated by a laser diode emitting at the free-space wavelength of $\lambda_0 = 850$ nm. The vertical axis plots the differential voltage measured from two amplified photodiodes capturing the 0^{th} and the -1^{st} diffracted orders. The sketches given at the bottom are not to scale.

at the left working point. This working point was arbitrarily chosen since the performances were demonstrated as similar at both working points in the previous chapter.

After the functionalization of the detection surface with BSA, the injection of the anti-BSA solution through the flow cell resulted in an increase, ΔV, of 25.6 mV in the differential output signal. This signal increase was due to anti-BSA binding to the immobilized BSA layer. This demonstrates that plasmonic gratings operating in an optical switch configuration are suitable for protein detection. Figure 7.4 in section 7.5 (Appendix chapter) shows a similar study using anti-BSA for detecting BSA with a sandwich assay.

However, Figure 5.3 corresponds to a drift-corrected sensorgram. Indeed, the initial sensorgram presented a slight drift in the differential output signal fitting a linear model over time, as shown by the time trace given in Figure 5.4. This Figure compares the baseline (first injection of buffer) measured before the drift correction applied in Figure 5.3 with a linear model. The drift in the differential output signal was eliminated by fitting the responses to linear models and subtracting them from the raw data. We believe that this drift was caused by mechanical drift in one of the stages in the interrogation setup that we used to fix the angle of incidence at one of the working points and to collect the power of the 0^{th} and the -1^{st} orders via two photodiodes. To overcome this issue, an interrogation setup with fewer mechanical items, such as that shown in section 7.6 in the appendix could be used.

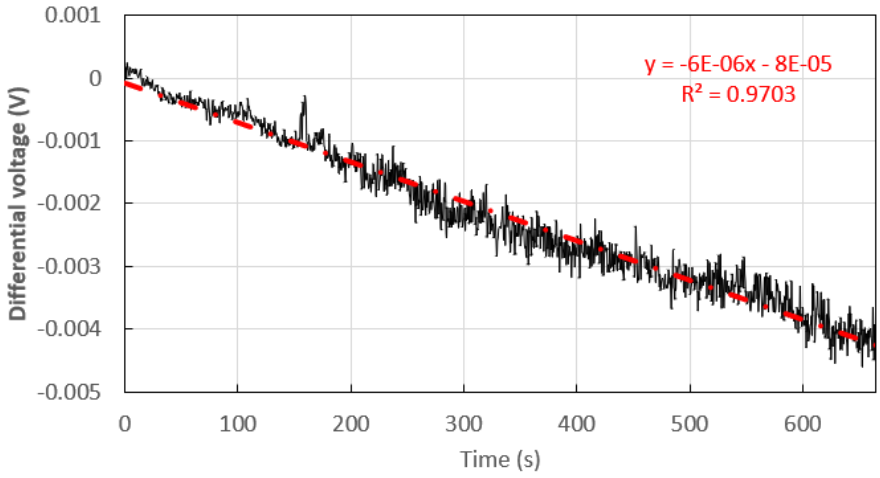

Figure 5.4: Time traces (black solid curve) associated with the injection of the first buffer solution in the sensorgram given in Figure 5.3 before the correction of the drift. The red dashed line corresponds to the best fitting linear model. Equations and R^2 goodness of fit are given on the top of the traces.

In addition, Figure 5.3 shows an abrupt transient variation in the differential output signal between the second injection of buffer and the injection of BSA solution. We believe that this punctual variation resulted from fluidic disturbances due to dead volumes of residual EDC/NHS solution. Indeed, this variation is similar to those observed in the sensorgrams for bulk sensing

given in the previous chapter. Moreover, it occurs after the sequential injection of two solutions with high contrast between their RI. Indeed, as shown in Figure 5.3, the EDC/NHS solution induced a strong increase in the differential output voltage compared to the buffer. As explained in the previous chapter, that implies that the RI of the EDC/NHS solution was higher than that of the buffer. Thus, residual EDC/NHS solution could have induced an increase in the differential output voltage because of it was set into motion due to the turn off and on of the pump.

To overcome this second issue, the second flow cell design having an elongated shape (described in section 5.2) was used to perform the next bio-assays. Figure 5.5 shows a complete cycle for the detection of HSA (100 μg/mL) with anti-HSA performed in this channel flow cell. It does not present any larger transient variation. That suggests that the channel flow cell design prevents dead volumes compared to the circular flow cell.

In these measurements, a high concentration (40 μg/mL) of anti-HSA was injected to functionalise the surface and ensure its saturation. Yet, binding with the SAM layer induced a lower increase in the differential output voltage than expected and does not agree well with an exponential model typical for these interactions [170], as shown in Figure 5.5. Indeed, the anti-HSA solution used was prepared with products that were delivered under poor transport conditions, such that denatured anti-HSA was suspected.

Next, BSA (100 μg/mL) was injected over the gold-coated grating replica as a negative control and also as a blocking agent of unreacted sites, as shown in the fourth sketch of Figure 5.5. This injection resulted in a slight increase of $\Delta V_{BSA} = 4.10$ mV in the differential output signal. This suggests that the SAM layer was not covered by a perfectly uniform anti-HSA layer and presented unreacted sites, on which some BSA proteins were non-specifically immobilized.

However, the injection of HSA at the same concentration (100 μg/mL) induced an increase,

ΔV_{HSA}, 12-fold higher in the differential output voltage than the BSA injection. This demonstrates selectivity in the binding between the biorecognition layer on the detection surface (anti-HSA) and the targeted analyte (HSA), despite the poor response observed at the beginning of the detection cycle during the injection and immobilisation of anti-HSA.

The sensorgram of Figure 5.5 was drift corrected in the same way as the sensorgram presented in Figure 5.3. Indeed the change of the flow cell design did not reduce the drift. As previously mentioned, a setup with fewer mechanical items such as that presented in section 7.6 in the Appendix could help in overcoming this issue. The detailed protocol applied to lead this experiment is summarized in Table 7.28 (Appendix chapter).

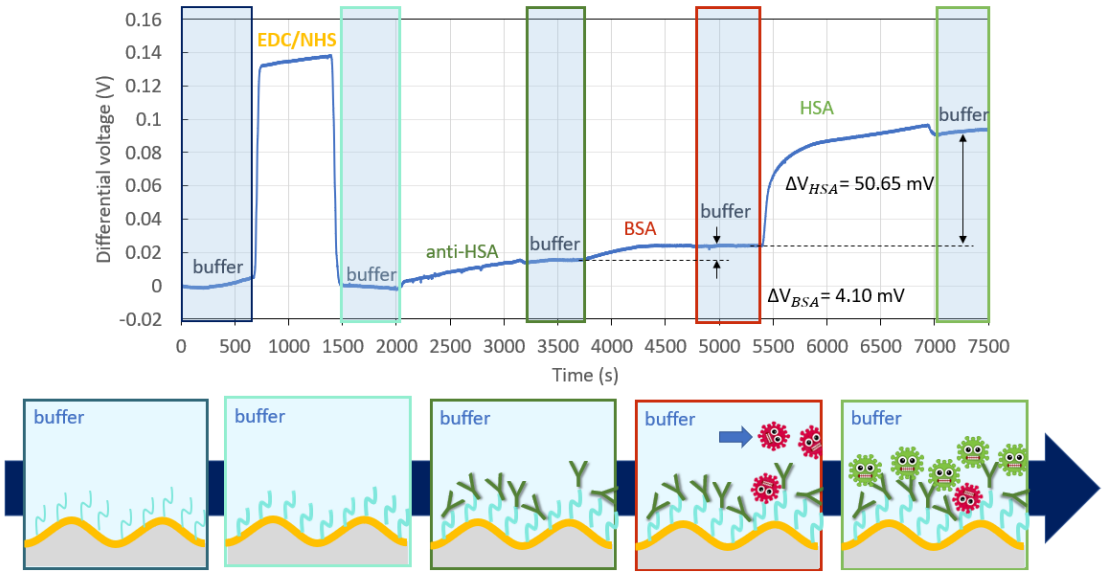

Figure 5.5: Complete cycle for the direct detection of HSA by anti-HSA immobilized on a gold-coated sinusoidal grating of period 770 nm and depth 247 nm. The grating was interrogated by a laser diode emitting at the free-space wavelength of $\lambda_0 = 850$ nm. The vertical axis plots the differential voltage measured from two amplified photodiodes capturing the 0^{th} and the -1^{st} diffracted orders. The sketches given at the bottom are not to scale.

5.5 Conclusion

In this chapter, the proposed device working in the optical switch configuration was demonstrated for biosensing via the binding of anti-BSA to a BSA-functionalized grating surface. An anti-BSA concentration of 25 μg/mL was successfully detected. The selectivity in the immobilization of the targeted analytes was shown via a negative control with BSA during a cycle of HSA detection with anti-HSA.

The plasmonic configuration based on the optical switch effect was shown as a promising detection tool for proteins via the differential detection of two diffracted orders, which enables the suppression of common noise and a robust interrogation.

However, the assays presented in this chapter were performed with clean fluids, which carried on only antibodies and antigens. Experiments should be carried out in complex physiological fluids such as blood and saliva to demonstrate their potential for POC applications. Thus, this configuration of detection could be used for the detection of infectious diseases such as COVID-19 by using specific antigens of the COVID-19 virus as agents of biorecognition to functionalize the grating surface. With this approach, the antibodies produced by the infected patients as an immune response to the virus and circulating in their blood could be detected and would enable their diagnostic. In addition, their quantification would help in the identification of the stage of the infection.

Chapter 6

General conclusion

6.1 Highlights

The COVID-19 pandemic highlighted the need for competitive and cost-effective biosensors. This thesis proposes and demonstrates the optical switch configuration using plasmonic gratings for biosensing applications, potentially addressing this need. In chapter 1, an overview of the biosensors currently used in the clinical and industrial fields was given. It highlighted the main issues of these detection devices (including the PCR tests) such as their cumbersome procedures to prepare and analyze the samples collected from patients with specific and expensive equipment.

In Chapter 2, the plasmonic biosensors were presented as a promising alternative to overcome the drawbacks mentioned above. The most conventional methods of coupling based on the SPR were detailed and their respective performance discussed. The combination of a grating coupler and a configuration based on a differential measurement was suggested as promising by highlighting the advantages of the conventional grating-coupler configuration (portable, easy-to-integrate into a fluidic system, tunable, ...) and those relative to the plasmonic interferometers (high performances) without their drawbacks (bulky arrangement).

In Chapter 3, the concept of the optical switch effect was introduced and a new biosensor configuration using this effect was presented. This specific configuration based on differential measurements between two diffracted orders was suggested as promising for large-scale sensing with a design of grating couplers fabricated by a low-cost mass-manufacturing technique. The detailed LIL and nanoimprint protocols developed to fabricate the sinusoidal gratings used in this configuration, having a high depth/period ratio, in a material resistant to prolonged exposure to fluids, were described. Next, the numerical method used to optimize the theoretical parameters of the grating design based on their computed switch pattern in water was described. The effects of the main design parameters (period, depth, profile) on the optical switch pattern were theoretically and experimentally studied. Thus, quasi-sinusoidal grating replicas were produced with a period of 770 nm and a depth of 228 nm. The switch patterns of these gold-coated grating replicas agreed well with the theory.

In chapter 4, the optical switch configuration was successfully demonstrated with a simple setup for the detection of small RI variations in the bulk. A LOD in the range of 10^{-6} RIU was achieved for bulk sensing in solution (comprised of water and glycerol) at both working points. Differential measurements between both monitored diffracted orders were highlighted as effective to cancel common perturbations to both monitored orders, especially in the case of artificial and parasitic noise.

In chapter 5, bio-assays in clean solutions (antigen or antibody in buffer) were used with the optical switch biosensors to demonstrate the potential of this configuration for biosensing applications. A concentration of 25 μg/mL of anti-BSA was successfully detected via direct detection using BSA as the biorecognition agent immobilized on the grating surface. Additionally, the selectivity in the immobilization of the targeted analytes on the biorecognition layer was demonstrated via a negative control with BSA during a cycle of HSA detection with anti-HSA. Finally, the effect of the flow cell geometry was also discussed based on the experimental results.

6.2 Thesis contributions

The following publications have emerged from the work carried out in this thesis:

[1] Laffont, E., Crespo-Monteiro, N., Berini, P., and Jourlin, Y. (2022, May). Development of a new plasmonic transducer for the detection of biological species. In Optical Sensing and Detection VII (Vol. 12139, pp. 97-105). SPIE.

[2] Laffont, E., Crespo-Monteiro, N., Valour, A., Berini, P., and Jourlin, Y. (2023). Differential Sensing with Replicated Plasmonic Gratings Interrogated in the Optical Switch Configuration. Sensors, 23(3), 1188.

[3] Bruhier, H., Dutems, J., Laffont, E., Crespo-Monteiro, N., Verrier, I., Parriaux, O., Berini, P. and Jourlin, Y. (2023). Common-mode plasmon sensing scheme as a high sensitivity compact SPR sensor. Optics Letters.

[4] Laffont, E., Crespo-Monteiro, N., Valour, A., Berini, P., and Jourlin, Y. (2023, August) SPR biosensor based on a grating coupler operating in the optical switch configuration. In Bio Sensing. Optica Sensing Congress.

[5] Laffont, E., Crespo-Monteiro, N., Valour, A., Berini, P., and Jourlin, Y., (accepted 11/03/2023) Performance of grating couplers used in the optical switch configuration. Sensors, MDPI.

6.3 Future work

In this thesis, the optical switch pattern configuration was demonstrated as a highly promising approach for biosensing. Yet, the preliminary bio-assays presented were performed with the most basic strategy of functionalization termed as "direct" and with clean solutions, only comprising one analyte in buffer. Thus, before being used in POC for testing and screening, new assays with complex matrices (saliva, blood, urine, ...) should be performed to show high enough performance to work with complex samples collected from patients. In addition, supplementary steps in the functionalization protocol could be required such as the injection of blocking agents to

prevent non-specific binding, as described in the articles [171, 172] for the detection of leukemia markers in leukemic patient sera and the detection of the NS1 dengue antigen in blood plasma. Besides, more elaborated strategies of functionalization (sandwich, inhibition, competitive) could be explored to enhance the performance currently achieved, as demonstrated on long-range surface plasmon waveguide biosensors in the article [173].

This thesis also highlighted the non-negligible effect of the flow cell geometry on the performance achieved with the proposed configuration. Indeed, based on the experimental results given in chapters 4 and 5, the shape and the dimensions of the flow cell have an effect on the potential fluidic perturbations. As mentioned in these chapters, a recent study [169] demonstrated that a design consisting of a curved top wall fluidic cell improved the uniformity of analyte bindings and so the performance of similar detection devices. A deeper study on the geometry of the flow cell could enhance the performance currently achieved, further miniaturize the sensing platform, and reduce the volume of solution required for detection. This work [169] led by Deng *etal*. is encouraging, since it suggests a low-cost protocol to produce the design of the lid mentioned above.

In further investigations, the flow cell could be straighter in order to fabricate several flow channels parallel to each other on the same lid. Thus, non-specific binding could be assessed by using some of the channels as references. In addition, multi-sensing could be performed simultaneously, as demonstrated in the article [90]. Such a design of flow cell could be especially interesting for biosensing in complex matrices such as saliva, blood, urine...

Moreover, the sensing surface in this thesis was frontside illuminated through the transparent lid and sensing fluid, resulting in collisions with the fluidic tubing and possibly additional noise. Furthermore, the pressures applied to the lid of the sensing platform during the injection of the solutions, could have induced a slight deformation of the lid. Backside illumination combined with the dielectric switch configuration could overcome this problem. Such a configu-

ration could consist of a binary grating fabricated in a high RI material illuminated through its backside. Theoretical studies were initiated for this configuration [174, 175], but it has not yet been experimentally demonstrated. That could be an interesting avenue to explore to enhance the performance currently achieved.

Moreover, it would avoid probing directly the biomolecules immobilized on the surface of the sample with a light source. That would widen the light source wavelength choice, which would no longer be conditioned by the biocompatibility with bioproducts and their potential spectrum of absorption.

Finally, a two-dimensional grating design could be developed for dual interrogation, enabling simultaneous probing of two different structures with a simple change in polarization. Such structures were studied, for example, in 2018, by Nair *et al.* demonstrated who demonstrated a new portable SPR biosensor based on 2D grating coupler for the detection of uropathegonic *E.coli* [176]. Yet, the main drawback of such a system of detection is the correlation between its performance and the resolution of its USB spectrophotometer. This kind of drawback could be overcome with the optical switch configuration based on intensity interrogation rather than spectral interrogation. Indeed, photodiodes are less cumbersome and less expensive than a spectrophotometer. Thus, this configuration could present a high potential to advance biosensing challenges, especially into POC applications. This could especially help to identify antibodies reacting with the same antigent but having different masses, like IgG *vs.* IgM antibodies (which react with the same antigen but have different mass). The ratio between these antibodies can give information about the state of an infectious disease because of their different evolution over time, as explained in the case of COVID-19 in [51].

To summarize, this thesis paves the way for the use of the optical switch configuration for biosensing applications. Yet, several avenues, such as those mentioned above, have still to be explored to make this configuration usable in POC for large-scale testing and screening.

Chapter 7

Appendix

7.1 Detailed protocols and references of each product used for producing grating masters and replicas

Product reference	**Manufacturer**
26 x 26 mm^2 glass substrate, NEGS1	Neyco
SurPass^{TM} 4000	Dischem
Positive photoresist Shipley S1828	MICROPOSIT
Plastic micropipettes	Fisher scientific

Table 7.1: Reference and manufacturer of each product used to fabricate the grating masters.

Solution	Technique	Time
Acetone	Ultrasonic bath	10 min
Ethanol	Ultrasonic bath	10 min
De-ionized water	Static incubation	10 min
Nitrogen gas	Drying	Until no water remains on the sample

Table 7.2: Sequential steps for cleaning and drying the glass substrates.

Volume	Technique	Speed, time
A few milliliters (enough to cover the surface of the glass substrate)	Static dispense with a single-use plastic micropipette	NA
NA	Spin coating	3000 rpm (acceleration), 10 s
NA	Spin-coating	5000 rpm, 50 s

Table 7.3: Sequential steps for $Surpass^{TM}$ deposition on the glass substrates.

Volume	Technique	Speed, time
A few milliliters (enough to cover the surface of the glass substrate)	Static dispense with a single-use plastic micropipette	NA
NA	Spin coating	3000 rpm (acceleration), 10 s
NA	Spin-coating	5000 rpm, 50 s

Table 7.4: Sequential steps for S1828 deposition on the glass substrates.

Hot plate	Temperature	Time
No longer produced, Karl Suss Microtech	60°C	1 min

Table 7.5: Parameters applied for soft-baking the S1828 coated sample.

Light source, wavelength	Beam number	Power density at sample holder	Exposure time
Laser He-Cd, 442 nm	1	204 µW/cm^2	115 s
Laser He-Cd, 442 nm	2 balanced	408 µW/cm^2	115 s

Table 7.6: Parameters applied for LIL.

Solution, Manufacturer	Technique	Time
Developer MF319, MICROPOSIT	Handly dip	9 s

Table 7.7: Parameters applied for the development of the S1828 coated sample.

PDMS category	Mixture	Manufacturer
Hard	3:1 ratio (by weight) RTV615 silicone rubber compound with a curing agent	Momentive^{TM}
Soft	9:1 ratio (by weight) RTV615 silicone rubber compound with a curing agent	Momentive^{TM}

Table 7.8: Composition and manufacturer of the products used for preparing hard and soft PDMS.

Volume	Technique	Speed, time
A few milliliters (enough to cover the surface of the glass substrate)	Static dispense with a single-use plastic micropipette	NA
NA	Spin coating	3000 rpm (acceleration), 10 s
NA	Spin-coating	5000 rpm, 50 s

Table 7.9: Sequential steps applied for depositing hard PDMS on a grating master.

RTA oven	Temperature	Time
AS-One 100, Annealsys	50°C	30 min
AS-One 100, Annealsys	70°C	1 h

Table 7.10: Sequential steps applied for soft-baking the hard PDMS coated grating master.

Volume	Technique	Speed, time
A few milliliters (enough to cover the surface of the glass substrate)	Static dispense with a single-use plastic micropipette	NA

Table 7.11: Soft PDMS deposition on the hard PDMS coated grating master.

RTA oven	Temperature	Time
AS-One 100, Annealsys	70°C	2 h

Table 7.12: Parameters applied for soft-baking the soft PDMS coated grating master.

Product reference	**Manufacturer**
26 x 26 mm^2 glass substrate, NEGS1	Neyco
Amoprime	AMO
Amonil MMS1	AMO

Table 7.13: Reference and manufacturer of each product used for fabricating grating replica.

Volume	**Technique**	**Speed, time**
A few milliliters (enough to cover the surface of the glass substrate)	Static dispense with a single-use plastic micropipette	NA
NA	Spin coating	3000 rpm (acceleration), 10 s
NA	Spin-coating	5000 rpm, 50 s

Table 7.14: Sequential steps carried out for depositing Amoprime.

Volume	**Technique**	**Speed, time**
A few milliliters (enough to cover the surface of the glass substrate)	Static dispense with a single-use plastic micropipette	NA
NA	Spin coating	3000 rpm (acceleration), 10 s
NA	Spin-coating	5000 rpm, 50 s

Table 7.15: Sequential steps carried out for depositing Amonil MMS1.

Printing press, manufacturer	**Applied pressure**	**Time**
REV 3S, Transmatic	1 mbar	30 s

Table 7.16: Parameters of the printing process applied on the PDMS stamp covering the Amonil deposition.

UV light source, manufacturer	Time
Ucube 365-100-2, Uwave	10 s

Table 7.17: Parameters of the UV illumination applied on the PDMS stamp covering the Amonil deposition.

Hot plate	Temperature	Time
No longer produced, Karl Suss Microtech	60°C	1 min

Table 7.18: Parameters applied for soft-baking the PDMS stamp coated sample.

Metal	Technique	Pressure	Deposition rate	Final thickness
Chromium	Thermal evaporation	10^{-6} mbar	3-4 Å/s	6-7 nm
Gold	Thermal evaporation	10^{-6} mbar	13-14 Å/s	120-121 nm

Table 7.19: Parameters applied for the sequential metal layers (chromium and gold) deposition by thermal evaporation.

7.2 Features of the items, products and solutions used for bulk sensing

Item	Features and reference	Manufacturer
Laser diode	1 mW, 850nm Alignment Laser Diode, **#37-038**	Edmund Optics

Polariser	LPVIS050-MP2, Mounted VIS Linear Polarizer, 12.5mm OD	Thorlabs
Aperture	ID8/M - Mounted Standard Iris, Ø8.0 mm Max Aperture, TR75/M Post	Thorlabs
Photodiodes (x2)	BPW 34 FA	OSRAM DIL
PEGT lid	Colorless, 1200 mm x 620 mm x 1mm	RS PRO
O-ring	EPDM (ethylene propylene diene monomer), product number NG0201023095	Paul
PEEK Tubing	1/32 in. O.D., 10 ft, Catalog number 03-350-523, by Trajan Scientific and Medical 130102000410F, Color: Orange, Diameter (English) Inner: 0.020 in.	Fisher scientific
Syringes	BD Luer-Lok™ Syringe sterile, single-use, 10 mL	Fisher scientific
Needles	BD General Use and PrecisionGlide Hypodermic Needles, BD 305196	Fisher scientific
DAQ	±10 V, 1 MS/s, 16-Bit, Simultaneous Input, 4-Channel C Series Voltage Input Module, NI-9223	NI, Emerson

Table 7.20: Features, reference, and manufacturer of each item used in the setup.

Reference	**Features**	**Manufacturer**
Glycerol	BioUltra, for molecular biology, anhydrous, 99.5% (GC), ref 49767	Sigma-Aldrich

Table 7.21: Reference and features of the glycerol used for preparing the bulk sensing solutions.

Solution number	**Glycerol mass**	**Final volume**	**Average RI measured by METRICON at = 1312 nm**	**Standard deviation (4 sequential measurements) assessed by METRICON at = 1312 nm**	**RI ($_0$ = 850 nm) calculated based on Sellmeier relation**
S0	0 g	10 mL	1.3211	0	1.3274
S1	0.4666 g	10 mL	1.3265	0	1.3326
S2	0.6652 g	10 mL	1.3283	0.0001	1.3347
S3	0.8721 g	10 mL	1.3311	0.0002	1.3368

Table 7.22: Composition and features of each bulk sensing solution.

Injection or incubation	**Time**	**Flow-rate**	**Solution**	**Comment**
Injection Incubation	4 min 4 min	160 µL/min NA	S0 (water)	It establishes the baseline. It ensures that no pressure constraints induce variations in the differential signal compared to the previous injection step.
Injection Incubation Injection Incubation Injection Incubation	4 min 4 min 4 min 4 min 4 min 4 min	160 µL/min NA 160 µL/min NA 160 µL/min NA	S1 S2 S3	It demonstrates the linearity correlation between the differential signal measured and the RI of the injected solutions
Injection Incubation Injection Incubation Injection Incubation	4 min 4 min 4 min 4 min 4 min 4 min	160 µL/min NA 160 µL/min NA 160 µL/min NA	S2 S1 S0 (water)	It demonstrates the repeatability of the measurements. The differential signal must be recovered for the injection of the same solution.

Table 7.23: Sequential steps carried out for each bulk sensing assay.

7.3 Bulk sensing

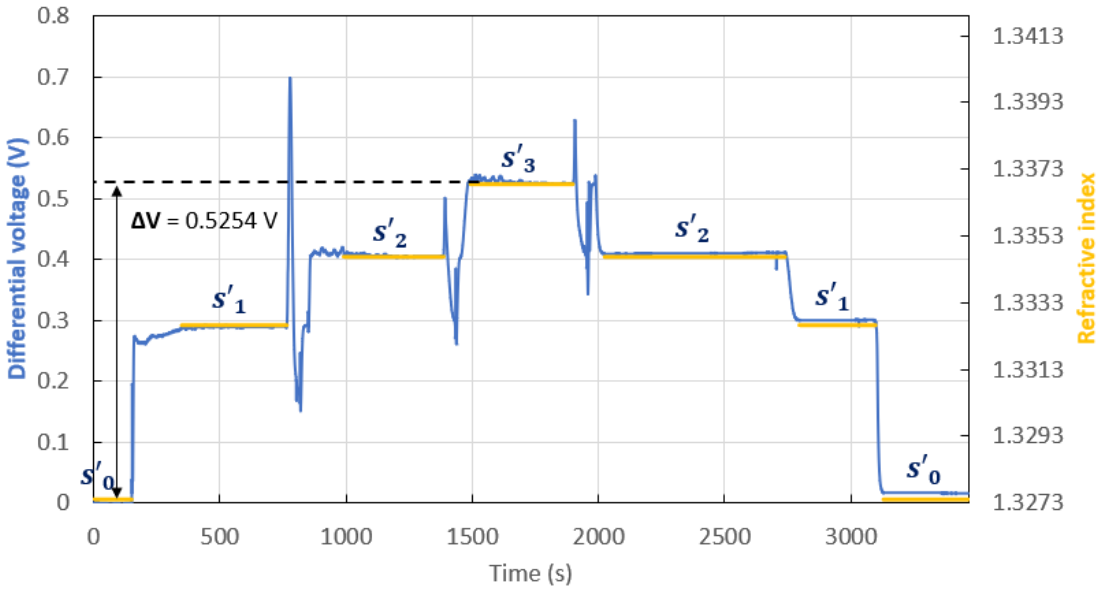

Figure 7.1: Differential measurement (blue curve) resulting from the power variations between the 0^{th} and the -1^{st} orders of the diffraction grating master interrogated by a p-polarized beam at free-space wavelength $\lambda_0 = 850$ nm at left working point, θ_l. The yellow lines represent the RI of the solution injected at $\lambda_0 = 850$ nm. This Figure is adapted from [177]. The colour of the differential voltage trace was changed.

Figure 7.1 shows a sensorgram performed at the left working point by probing the surface of a grating master during the sequential injections of the solutions s'_0, s'_1, s'_2 and s'_3. The RI of these solutions are reported in Table 7.24. They were measured using an instrument at $\lambda_0 = 1312$ nm based on a prism coupler (Metricon, Model 2010, Prism 200-P1) and calculated at $\lambda_0 = 850$ nm with Sellmeier dispersion equation 4.1 mentioned in chapter 4. The profile of the grating master interrogated, given in Figure 7.2, agrees obviously less with a sinusoid and is rougher (especially on the valleys and the peaks) than that associated with the grating replica used to perform the sensorgrams given in chapter 4. That certainly contributed to the worst performance reached despite a higher period of the grating ($\Lambda = 790$ nm), which should have resulted in higher performance than the 770 nm periodic grating replica used in chapter 4, as explained in section 3.4.2.

Indeed, Figure 7.3 shows a perfect linear correlation between the RI of the injected solutions and the differential output voltage measured in sensorgram given in Figure 7.1. That supports that there was an error of measurement in the mass of glycerol weighted to prepare the solution s_3 used to perform the sensorgram in subsection 4.3.2. Yet, the slope of the fitting linear model curve is lower (55.934 V/RIU) than that associated with the sensorgrams performed with the replica (82.082 V/RIU and 84.156 V/RIU at θ_l and θ_r) in subsection 4.3.2.

Solution	RI (λ_0 = 1312 nm)	RI (λ_0 = 850 nm)
s'_0	1.3274	1.3202
s'_1	1.3326	1.3253
s'_2	1.3346	1.3278
s'_3	1.3368	1.3295

Table 7.24: RI at $\lambda_0 = 850$ nm and $\lambda_0 = 1312$ nm for each solution injected during the sensorgram given in Figure 7.1.

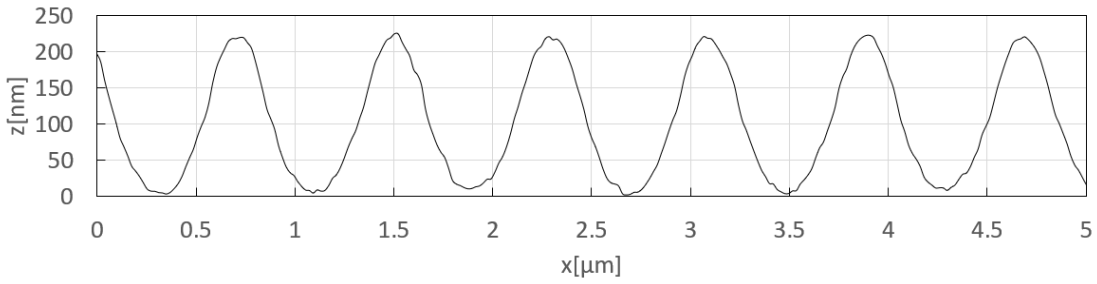

Figure 7.2: AFM profile of the corrugated gold-coated grating master used to perform the sensorgram in Figure 7.1.

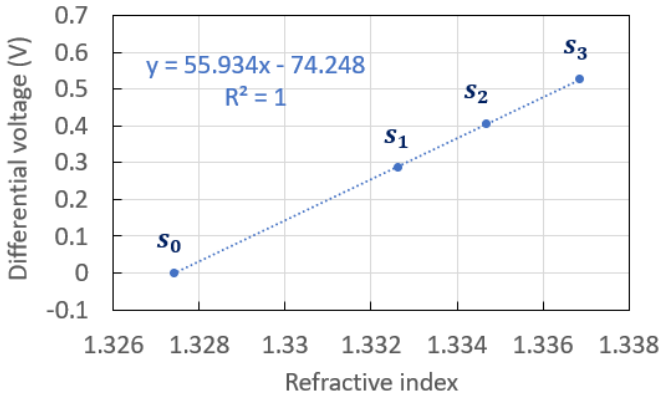

Figure 7.3: Linear correlation at the left working point between the differential output voltage and the RI of the injected solution given in Figure 7.1.

In addition, the differential output voltage shown in Figure 7.1 is obviously noisier than those shown in subsection 4.3.2, especially just after the injection of each solution.

Finally, the higher roughness of the grating master can be a serious drawback for a uniform immobilization of the biological species in the case of bio-assays.

7.4 Features and preparation of the products and solutions used for biosensing

Reference	**Features**	**Manufacturer**
16-MHA	16-MERCAPTOHEXADECANOIC ACID 98%, ref 674435-250MG	Merck
Buffer	PHOSPHATE BUFFERED SALINE, POWDER, PH 7., ref P3813-10PAK	Merck
EDC	N-(3-DIMETHYLAMINOPROPYL)-N'- ETHYL- &, ref 03449-5G	Merck

NHS	N-HYDROXYSUCCINIMIDE, 98%	Merck
BSA	Native Cow Bovine Serum Albumin protein, 50 g, ref ab64009	Abcam
Anti-BSA	Mouse monoclonal [1C12] to Bovine Serum Albumin, 100 µg, ref ab79827	Abcam
HSA	Native Human Serum Albumin protein (HRP), 1 mg, ref ab8032	Abcam
Anti-HSA	Mouse monoclonal [15C7] to Human Serum Albumin, 250 µg, ref ab10241	Abcam
SDS	DODECYL SULFATE, SODIUM SALT, 99+%, A.C., ref 436143-25G	Merck

Table 7.25: Reference, features, and manufacturer of each product used for preparing the solutions used during a complete bioassay.

Solution name	**Powder mass**	**Name of the solution used to dilute the powder**	**Volume of the solution used to dilute the powder**
16-MHA	144 mg	IPA	500 mL
Buffer	One packet	DI	500 mL
EDC/NHS	31 mg/31 mg	Buffer	2.5 mL
BSA (or HSA)	NA as depends on the targeted concentration (10 mg for a final concentration of 1 mg/mL)	Buffer	NA as depends on the targeted concentration (10 mL for a final concentration of 1 mg/mL)
SDS	55.6 mg	DI	5 mL

Table 7.26: Composition of solutions based on a powder product used in a bioassay.

Solution name	**Name, mass and concentration of the first solution mixed**	**Name and volume of the second solution mixed**
Anti-BSA	Mouse monoclonal [1C12] to Bovine Serum Albumin, 100 µg, 1mg/mL	Buffer, NA as depends on the targeted concentration (2.5 mL for a final concentration of 40 µg/mL)
Anti-HSA	Mouse monoclonal [15C7] to Human Serum Albumin, 250 µg, 2mg/mL	Buffer, NA as depends on the targeted concentration (9.875 mL for a final concentration of 25 µg/mL)

Table 7.27: Composition of solutions based on a liquid product used in a bioassay.

7.5 Sandwich assay

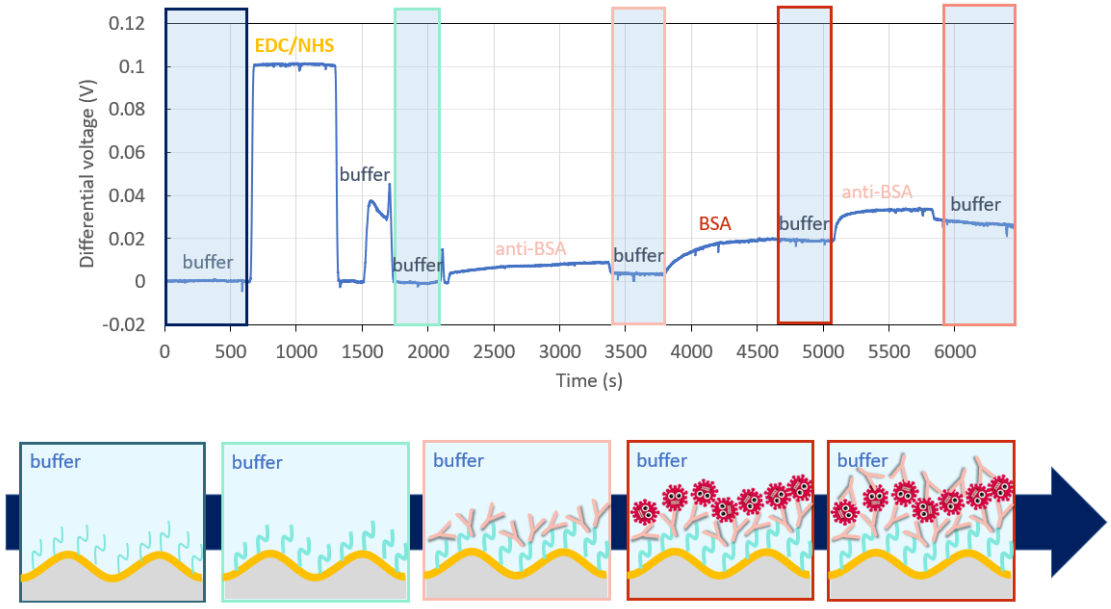

Figure 7.4: Complete cycle for the sandwich detection of BSA (40 μg/mL) by anti-BSA (40 μg/mL) immobilized on a gold-coated sinusoidal grating of period 770 nm and depth 228 nm. The grating was interrogated by a laser diode emitting at the free-space wavelength of $\lambda_0 = 850$ nm. The vertical axis plots the differential voltage measured from two amplified photodiodes capturing the 0^{th} and the -1^{st} diffracted orders. The sketches given at the bottom are not to scale.

7.6 Arch setup

As explained in Chapter 5, a part of the drift in the 0^{th} and -1^{st} orders was not eliminated by the differential measurements. To cancel it, a drift correction was applied to our data based on the linear model fitting with the baseline traces for each bio-assay. We assume that the rotation stage used in our setup could partially explain this drift.

To overcome this issue a setup with fewer mechanical items such as that presented in Figure 7.5 could be used. In the case of Figure 7.5 was used for pressure and gas detection. In the case

of biodetection in fluid, a similar system could be used but horizontally oriented with a flat angle bracket to further the elimination of potential air bubbles inside the flow cell. Indeed, after many fluidic tests, the fluidic system horizontally oriented demonstrated better performance, certainly correlated with the elimination of the air inside the flow cell than those oriented vertically.

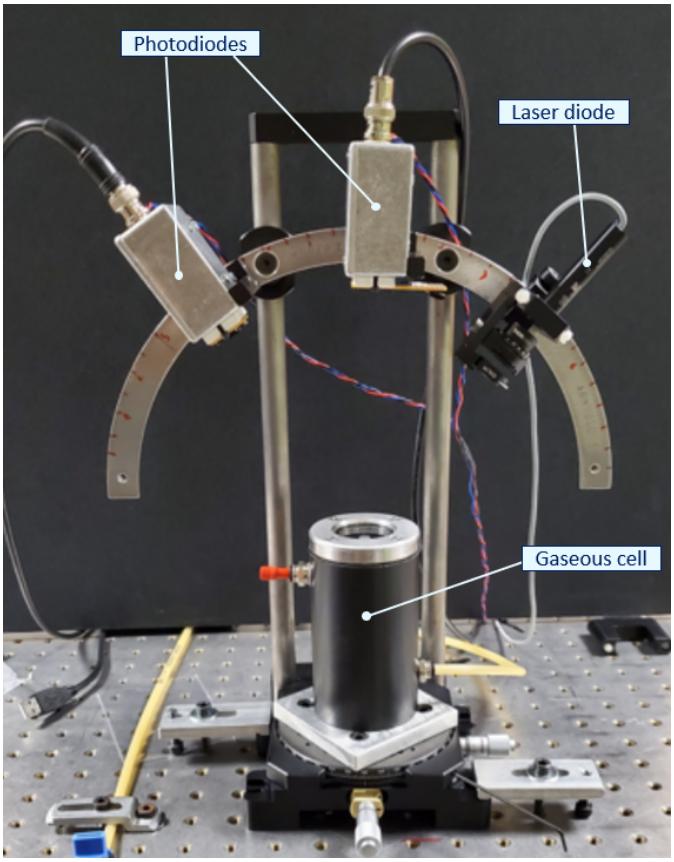

Figure 7.5: Picture of an arch setup used in the optical switch configuration.

7.7 Protocol applied for a direct bioassay with a negative control

Injection or incubation	**Time**	**Flow-rate**	**Solution**	**Comment**
Injection Incubation	6 min 6 min	50 µL/min NA	Buffer	Baseline establishment
Injection Incubation	7 min 7 min	50 µL/min NA	EDC/NHS	Activation of the carboxyle groups of the self-assembled monolayer
Injection Incubation	6 min 6 min	50 µL/min NA	Buffer	Re-establishment of the baseline
Injection Incubation	10 min Until the differential signal stagnates	50 µL/min NA	Biorecognition agent (e.g anti-HSA)	Functionalisation of grating surface
Injection Incubation	6 min 6 min	50 µL/min NA	Buffer	Re-establishment of the baseline
Injection Incubation	10 min Until the differential signal stagnates	50 µL/min NA	Negative control (e.g BSA)	Ensuring the selectivity of the detection
Injection Incubation	6 min 6 min	50 µL/min NA	Buffer	Re-establishment of the baseline, which can be slightly higher than after the previous injection of buffer if the self-assembled monolayer is not perfectly uniform

Injection Incubation	10 min Until the differential signal stagnates	50 µL/min NA	Targeted biomolecules (e.g HSA)	Selective detection
Injection Incubation	6 min 6 min	50 µL/min NA	Buffer	Re-establishment of the baseline, which should be higher than the that measured after the previous injection of buffer due to the selective interaction between the bio-recognition layer and the targeted analytes
Injection Incubation	7 min 7 min	50 µL/min NA	SDS	Regeneration of the grating surface
Injection Incubation	6 min 6 min	50 µL/min NA	Buffer	Re-establishment of the baseline, which should be recovered at the same value as that measured after the injection of buffer performed after the injection of the bio-recognition agents

Table 7.28: Sequential steps for performing a direct bioassay with a negative control.

Bibliography

[1] Claes Nylander, Bo Liedberg, and Tommy Lind. Gas detection by means of surface plasmon resonance. *Sensors and Actuators*, 3:79–88, 1982.

[2] Ibrahim Abdulhalim, Mohammad Zourob, and Akhlesh Lakhtakia. Surface plasmon resonance for biosensing: a mini-review. *Electromagnetics*, 28(3):214–242, 2008.

[3] Jiří Homola. Surface plasmon resonance sensors for detection of chemical and biological species. *Chemical reviews*, 108(2):462–493, 2008.

[4] Mohga E Hamza, Muhammad A Othman, and Mohamed A Swillam. Plasmonic biosensors. *Biology*, 11(5):621, 2022.

[5] Onur Tokel, Fatih Inci, and Utkan Demirci. Advances in plasmonic technologies for point of care applications. *Chemical reviews*, 114(11):5728–5752, 2014.

[6] Barbora Špačková, Piotr Wrobel, Markéta Bocková, and Jiří Homola. Optical biosensors based on plasmonic nanostructures: a review. *Proceedings of the IEEE*, 104(12):2380–2408, 2016.

[7] Maria Soler, Cesar S Huertas, and Laura M Lechuga. Label-free plasmonic biosensors for point-of-care diagnostics: A review. *Expert review of molecular diagnostics*, 19(1):71–81, 2019.

[8] Karishma Shah and Panagiotis Maghsoudlou. Enzyme-linked immunosorbent assay (elisa): the basics. *British journal of hospital medicine*, 77(7):C98–C101, 2016.

[9] Melanie A MacMullan, Albina Ibrayeva, Kylie Trettner, Laura Deming, Sudipta Das, Frances Tran, Jose Ricardo Moreno, Joseph G Casian, Prithivi Chellamuthu, Jeffrey Kraft, et al. Elisa detection of sars-cov-2 antibodies in saliva. *Scientific Reports*, 10(1):20818, 2020.

[10] J Huggett, K Dheda, S Bustin, and A Zumla. Real-time rt-pcr normalisation; strategies and considerations. *Genes & Immunity*, 6(4):279–284, 2005.

[11] Yoon-Seok Chung, Nam-Joo Lee, Sang Hee Woo, Jeong-Min Kim, Heui Man Kim, Hye Jun Jo, Ye Eun Park, and Myung-Guk Han. Validation of real-time rt-pcr for detection of sars-cov-2 in the early stages of the covid-19 outbreak in the republic of korea. *Scientific Reports*, 11(1):1–8, 2021.

[12] C Siaka, L Rugeri, C Caron, and J Goudemand. A new elisa assay for diagnosis of acquired von willebrand syndrome. *Haemophilia*, 9(3):303–308, 2003.

[13] Shamala Devi Sekaran, Ew Cheng Lan, Kanthesh Basalingappa Mahesawarappa, Ramapraba Appanna, and Geetha Subramaniam. Evaluation of a dengue ns1 capture elisa assay for the rapid detection of dengue. *J Infect Developing Countries*, 1(2):182–188, 2007.

[14] Sean X Leng, Janet E McElhaney, Jeremy D Walston, Dongxu Xie, Neal S Fedarko, and George A Kuchel. Elisa and multiplex technologies for cytokine measurement in inflammation and aging research. *The Journals of Gerontology Series A: Biological Sciences and Medical Sciences*, 63(8):879–884, 2008.

[15] Kanako Iha, Mikio Inada, Naoki Kawada, Kazunari Nakaishi, Satoshi Watabe, Yong Hong Tan, Chieh Shen, Liang-Yin Ke, Teruki Yoshimura, and Etsuro Ito. Ultrasensitive elisa developed for diagnosis. *Diagnostics*, 9(3):78, 2019.

[16] Yaghoub Yazdani, Azam Roohi, Jalal Khoshnoodi, and Fazel Shokri. Development of a sensitive enzyme-linked immunosorbent assay for detection of hepatitis b surface antigen using novel monoclonal antibodies. *Avicenna journal of medical biotechnology*, 2(4):207, 2010.

[17] Marianne T Werner, Christiane K Fæste, and Eliann Egaas. Quantitative sandwich elisa for the determination of tropomyosin from crustaceans in foods. *Journal of agricultural and food chemistry*, 55(20):8025–8032, 2007.

[18] Mary Sekiya, Annetta Zintl, and Michael L Doherty. Bulk milk elisa and the diagnosis of parasite infections in dairy herds: a review. *Irish veterinary journal*, 66(1):1–12, 2013.

[19] Long Wu, Guanghui Li, Xin Xu, Lin Zhu, Riming Huang, and Xiaoqiang Chen. Application of nano-elisa in food analysis: Recent advances and challenges. *TrAC Trends in Analytical Chemistry*, 113:140–156, 2019.

[20] Luigino G Apollonio, Ian R Whittall, Dennis J Pianca, Jennelle M Kyd, and William A Maher. Matrix effect and cross-reactivity of select amphetamine-type substances, designer analogues, and putrefactive amines using the bio-quant direct elisa presumptive assays for amphetamine and methamphetamine. *Journal of analytical toxicology*, 31(4):208–213, 2007.

[21] Marleen Laloup, Gaëlle Tilman, Viviane Maes, Gert De Boeck, Pierre Wallemacq, Jan Ramaekers, and Nele Samyn. Validation of an elisa-based screening assay for the detection of amphetamine, mdma and mda in blood and oral fluid. *Forensic science international*, 153(1):29–37, 2005.

[22] Lei Ma, Yousef Abugalyon, and XiuJun Li. Multicolorimetric elisa biosensors on a paper/polymer hybrid analytical device for visual point-of-care detection of infection diseases. *Analytical and bioanalytical chemistry*, 413(18):4655–4663, 2021.

[23] Jim CE Odekerken, Dorien MW Logister, Loubna Assabre, Jacobus JC Arts, Geert HIM Walenkamp, and Tim JM Welting. Elisa-based detection of gentamicin and vancomycin in protein-containing samples. *SpringerPlus*, 4:1–8, 2015.

[24] Hamidreza Yadegari, Mehdi Mohammadi, Faezeh Maghsood, Ahmad Ghorbani, Tannaz Bahadori, Forough Golsaz-Shirazi, Amir-Hassan Zarnani, Vahid Salimi, Mahmood Jeddi-

Tehrani, Mohammad Mehdi Amiri, et al. Diagnostic performance of a novel antigen-capture elisa for the detection of sars-cov-2. *Analytical Biochemistry*, 666:115079, 2023.

[25] Sai Wang, Shuai Zhao, Xiao Wei, Shan Zhang, Jiahui Liu, and Yiyang Dong. An improved label-free indirect competitive spr immunosensor and its comparison with conventional elisa for ractopamine detection in swine urine. *Sensors*, 17(3):604, 2017.

[26] Yew Joon Tam, Nazariah Allaudin Zeenathul, Morvarid Akhavan Rezaei, Nor Hidayah Mustafa, Mohd Lila Mohd Azmi, Abdul Rani Bahaman, Sewn Cen Lo, Joo Shun Tan, Homayoun Hani, and Abdullah Rasedee. Wide dynamic range of surface-plasmon-resonance-based assay for hepatitis b surface antigen antibody optimal detection in comparison with elisa. *Biotechnology and applied biochemistry*, 64(5):735–744, 2017.

[27] Marten Beeg, Alessandro Nobili, Barbara Orsini, Francesca Rogai, Daniela Gilardi, Gionata Fiorino, Silvio Danese, Mario Salmona, Silvio Garattini, and Marco Gobbi. A surface plasmon resonance-based assay to measure serum concentrations of therapeutic antibodies and anti-drug antibodies. *Scientific Reports*, 9(1):2064, 2019.

[28] Fátima Fernández, Kateřina Hegnerová, Marek Piliarik, Francisco Sanchez-Baeza, Jiří Homola, and M-Pilar Marco. A label-free and portable multichannel surface plasmon resonance immunosensor for on site analysis of antibiotics in milk samples. *Biosensors and Bioelectronics*, 26(4):1231–1238, 2010.

[29] Sulieman M El Sanousi, Zakia A Osman, A Mohamed, MS Al Awfi, Yaser H Babair, and Maher H Babair. Comparison of real-time pcr versus elisa in the diagnosis of cytomegalovirus infection in pregnant women. *Clin Microbiol Infect Dis*, 1(3):67–9, 2016.

[30] Mahsa Lari Baghal, Mansour Mayahi, Nader Mosavari, and Zahra Boroomand. Comparison of pcr and designed elisa methods to detect avian tuberculosis in suspected pigeons. *Iran Vet J*, 16:29–37, 2020.

[31] Masoumeh Mardani-Kataki, Molouk Beiromvand, Ali Teimoori, Afshin Amari, and Mehdi

Tavalla. Is immuno-pcr better than elisa test for detection of toxoplasma gondii igg antibody? *Acta Parasitologica*, 67(2):904–911, 2022.

[32] Amjad Hayat Khan and Esmaeil Sadroddiny. Application of immuno-pcr for the detection of early stage cancer. *Molecular and cellular probes*, 30(2):106–112, 2016.

[33] Samuel Yang and Richard E Rothman. Pcr-based diagnostics for infectious diseases: uses, limitations, and future applications in acute-care settings. *The Lancet infectious diseases*, 4(6):337–348, 2004.

[34] Promod K Mehta, Ankush Raj, Netrapal Singh, and Gopal K Khuller. Diagnosis of extrapulmonary tuberculosis by pcr. *FEMS Immunology & Medical Microbiology*, 66(1):20–36, 2012.

[35] Guido Cordoni, Adele Williams, Andy Durham, Daniela Florio, Renato Giulio Zanoni, and Roberto M La Ragione. Rapid diagnosis of strangles (streptococcus equi subspecies equi) using pcr. *Research in Veterinary Science*, 102:162–166, 2015.

[36] Chenglong Zhou, Xiaohong Zhang, Wei Zhang, Junxia Duan, and Feijun Zhao. Pcr detection for syphilis diagnosis: Status and prospects. *Journal of clinical laboratory analysis*, 33(5):e22890, 2019.

[37] Waidi Folorunso Sule and Daniel Oladimeji Oluwayelu. Real-time rt-pcr for covid-19 diagnosis: challenges and prospects. *The Pan African Medical Journal*, 35(Suppl 2), 2020.

[38] Chantal BF Vogels, Mallery I Breban, Isabel M Ott, Tara Alpert, Mary E Petrone, Anne E Watkins, Chaney C Kalinich, Rebecca Earnest, Jessica E Rothman, Jaqueline Goes de Jesus, et al. Multiplex qpcr discriminates variants of concern to enhance global surveillance of sars-cov-2. *PLoS biology*, 19(5):e3001236, 2021.

[39] Mohini Joshi and JD Deshpande. Polymerase chain reaction: methods, principles and application. *International Journal of Biomedical Research*, 2(1):81–97, 2010.

[40] Ibon Santiago. Trends and innovations in biosensors for covid-19 mass testing. *ChemBioChem*, 21(20):2880–2889, 2020.

[41] Yunying Zhou, Fengyan Pei, Mingyu Ji, Li Wang, Huailong Zhao, Huanjie Li, Weihua Yang, Qingxi Wang, Qianqian Zhao, and Yunshan Wang. Sensitivity evaluation of 2019 novel coronavirus (sars-cov-2) rt-pcr detection kits and strategy to reduce false negative. *PLoS One*, 15(11):e0241469, 2020.

[42] Erika Varkonyi-Gasic, Rongmei Wu, Marion Wood, Eric F Walton, and Roger P Hellens. Protocol: a highly sensitive rt-pcr method for detection and quantification of microrna. *Plant methods*, 3(1):1–12, 2007.

[43] Xueliang Wang, Hangping Yao, Xing Xu, Pengyin Zhang, Minmin Zhang, Junbin Shao, Yanqun Xiao, and Hualiang Wang. Limits of detection of 6 approved rt–pcr kits for the novel sars-coronavirus-2 (sars-cov-2). *Clinical chemistry*, 66(7):977–979, 2020.

[44] Soo Ji Kang, Chan Song Jang, Ji Min Son, and Kwang Won Hong. Comparison of seven commercial taqman master mixes and two real-time pcr platforms regarding the rapid detection of porcine dna. *Food Science of Animal Resources*, 41(1):85, 2021.

[45] Kerstin Wernike, Markus Keller, Franz J Conraths, Thomas C Mettenleiter, Martin H Groschup, and Martin Beer. Pitfalls in sars-cov-2 pcr diagnostics. *Transboundary and emerging diseases*, 68(2):253–257, 2021.

[46] Alireza Tahamtan and Abdollah Ardebili. Real-time rt-pcr in covid-19 detection: issues affecting the results. *Expert review of molecular diagnostics*, 20(5):453–454, 2020.

[47] César MJA Metzger, Reto Lienhard, Helena MB Seth-Smith, Tim Roloff, Fanny Wegner, Jonas Sieber, Michael Bel, Gilbert Greub, and Adrian Egli. Pcr performance in the sars-cov-2 omicron variant of concern? *Swiss medical weekly*, 151(4950):w30120–w30120, 2021.

[48] Devendra T Mourya, Pragya D Yadav, Rajeev Mehla, Pradip V Barde, Prasanna N Yergolkar, Sandeep RP Kumar, Jyotsna P Thakare, and Akhilesh C Mishra. Diagnosis of

kyasanur forest disease by nested rt-pcr, real-time rt-pcr and igm capture elisa. *Journal of virological methods*, 186(1-2):49–54, 2012.

[49] Carlos Palomares-Reyes, Wilmer Silva-Caso, Luis J Del Valle, Miguel Angel Aguilar-Luis, Claudia Weilg, Johanna Martins-Luna, Adriana Viñas-Ospino, Luciana Stimmler, Naysha Mallqui Espinoza, Ronald Aquino Ortega, et al. Dengue diagnosis in an endemic area of peru: Clinical characteristics and positive frequencies by rt-pcr and serology for ns1, igm, and igg. *International Journal of infectious diseases*, 81:31–37, 2019.

[50] Zihan Li, Luca Leustean, Fatih Inci, Min Zheng, Utkan Demirci, and Shuqi Wang. Plasmonic-based platforms for diagnosis of infectious diseases at the point-of-care. *Biotechnology advances*, 37(8):107440, 2019.

[51] Isabela A Mattioli, Ayaz Hassan, Osvaldo N Oliveira Jr, and Frank N Crespilho. On the challenges for the diagnosis of sars-cov-2 based on a review of current methodologies. *ACS sensors*, 5(12):3655–3677, 2020.

[52] Alexander N Baker, Sarah-Jane Richards, Collette S Guy, Thomas R Congdon, Muhammad Hasan, Alexander J Zwetsloot, Angelo Gallo, Jozef R Lewandowski, Phillip J Stansfeld, Anne Straube, et al. The sars-cov-2 spike protein binds sialic acids and enables rapid detection in a lateral flow point of care diagnostic device. *ACS central science*, 6(11):2046–2052, 2020.

[53] Aldo Roda, Simone Cavalera, Fabio Di Nardo, Donato Calabria, Sergio Rosati, Patrizia Simoni, Barbara Colitti, Claudio Baggiani, Matilde Roda, and Laura Anfossi. Dual lateral flow optical/chemiluminescence immunosensors for the rapid detection of salivary and serum iga in patients with covid-19 disease. *Biosensors and Bioelectronics*, 172:112765, 2021.

[54] Tao Peng, Xiangpei Liu, L Garry Adams, Girish Agarwal, Bruce Akey, Jeffrey Cirillo, Volker Deckert, Sahar Delfan, Edward Fry, Zehua Han, et al. Enhancing sensitivity of lateral flow assay with application to sars-cov-2. *Applied Physics Letters*, 117(12), 2020.

[55] Sharda Kotru, Martin Klimuntowski, Hashim Ridha, Zakir Uddin, Ali A Askhar, Gurmit Singh, and Matiar MR Howlader. Electrochemical sensing: A prognostic tool in the fight against covid-19. *TrAC Trends in Analytical Chemistry*, 136:116198, 2021.

[56] Jiri Kudr, Petr Michalek, Lada Ilieva, Vojtech Adam, and Ondrej Zitka. Covid-19: A challenge for electrochemical biosensors. *TrAC Trends in Analytical Chemistry*, 136:116192, 2021.

[57] Neeraj Kumar, Nagaraj P Shetti, Somanath Jagannath, and Tejraj M Aminabhavi. Electrochemical sensors for the detection of sars-cov-2 virus. *Chemical Engineering Journal*, 430:132966, 2022.

[58] Jack Ferguson, Steven Dunn, Angus Best, Jeremy Mirza, Benita Percival, Megan Mayhew, Oliver Megram, Fiona Ashford, Thomas White, Emma Moles-Garcia, et al. Validation testing to determine the sensitivity of lateral flow testing for asymptomatic sars-cov-2 detection in low prevalence settings: Testing frequency and public health messaging is key. *PLoS Biology*, 19(4):e3001216, 2021.

[59] Dylan A Mistry, Jenny Y Wang, Mika-Erik Moeser, Thomas Starkey, and Lennard YW Lee. A systematic review of the sensitivity and specificity of lateral flow devices in the detection of sars-cov-2. *BMC infectious diseases*, 21(1):1–14, 2021.

[60] Hui Zhao, Feng Liu, Wei Xie, Tai-Cheng Zhou, Jun OuYang, Lian Jin, Hui Li, Chun-Yan Zhao, Liang Zhang, Jia Wei, et al. Ultrasensitive supersandwich-type electrochemical sensor for sars-cov-2 from the infected covid-19 patients using a smartphone. *Sensors and Actuators B: Chemical*, 327:128899, 2021.

[61] G Balkourani, A Brouzgou, M Archonti, N Papandrianos, S Song, and P Tsiakaras. Emerging materials for the electrochemical detection of covid-19. *Journal of Electroanalytical Chemistry*, 893:115289, 2021.

[62] Jiang Xu, Liam Kerr, Yue Jiang, Wenhao Suo, Lei Zhang, Taotao Lao, Yuxin Chen, and

Yan Zhang. Rapid antigen diagnostics as frontline testing in the covid-19 pandemic. *Small Science*, 2(8):2200009, 2022.

[63] Carly Tymm, Junhu Zhou, Amogha Tadimety, Alison Burklund, and John XJ Zhang. Scalable covid-19 detection enabled by lab-on-chip biosensors. *Cellular and Molecular Bioengineering*, 13:313–329, 2020.

[64] Anna Meneghello, Agnese Sonato, Gianluca Ruffato, Gabriele Zacco, and Filippo Romanato. A novel high sensitive surface plasmon resonance legionella pneumophila sensing platform. *Sensors and Actuators B: Chemical*, 250:351–355, 2017.

[65] Jinling Zhang, Imran Khan, Qingwen Zhang, Xiaohu Liu, Jakub Dostalek, Bo Liedberg, and Yi Wang. Lipopolysaccharides detection on a grating-coupled surface plasmon resonance smartphone biosensor. *Biosensors and Bioelectronics*, 99:312–317, 2018.

[66] Gaurav Pal Singh and Neha Sardana. Smartphone-based surface plasmon resonance sensors: a review. *Plasmonics*, 17(5):1869–1888, 2022.

[67] Hana Sipova, Shile Zhang, Aimee M Dudley, David Galas, Kai Wang, and Jiri Homola. Surface plasmon resonance biosensor for rapid label-free detection of microribonucleic acid at subfemtomole level. *Analytical chemistry*, 82(24):10110–10115, 2010.

[68] Jiřı Homola, Sinclair S Yee, and Günter Gauglitz. Surface plasmon resonance sensors. *Sensors and actuators B: Chemical*, 54(1-2):3–15, 1999.

[69] Atef Shalabney and Ibrahim Abdulhalim. Sensitivity-enhancement methods for surface plasmon sensors. *Laser & Photonics Reviews*, 5(4):571–606, 2011.

[70] Robert Williams Wood. Xlii. on a remarkable case of uneven distribution of light in a diffraction grating spectrum. *The London, Edinburgh, and Dublin Philosophical Magazine and Journal of Science*, 4(21):396–402, 1902.

[71] Bo Liedberg, Claes Nylander, and Ingemar Lunström. Surface plasmon resonance for gas detection and biosensing. *Sensors and actuators*, 4:299–304, 1983.

[72] Briliant Adhi Prabowo, Agnes Purwidyantri, and Kou-Chen Liu. Surface plasmon resonance optical sensor: A review on light source technology. *Biosensors*, 8(3):80, 2018.

[73] Stefano Rossi, Enrico Gazzola, Pietro Capaldo, Giulia Borile, and Filippo Romanato. Grating-coupled surface plasmon resonance (gc-spr) optimization for phase-interrogation biosensing in a microfluidic chamber. *Sensors*, 18(5):1621, 2018.

[74] Youjun Zeng, Xueliang Wang, Jie Zhou, Ruibiao Miyan, Junle Qu, Ho-Pui Ho, Kaiming Zhou, Bruce Zhi Gao, and Yonghong Shao. Phase interrogation spr sensing based on white light polarized interference for wide dynamic detection range. *Optics express*, 28(3):3442–3450, 2020.

[75] Erwin Kretschmann and Heinz Raether. Radiative decay of non radiative surface plasmons excited by light. *Zeitschrift für Naturforschung A*, 23(12):2135–2136, 1968.

[76] Celina M Miyazaki, Flávio M Shimizu, and Marystela Ferreira. Surface plasmon resonance (spr) for sensors and biosensors. In *Nanocharacterization techniques*, pages 183–200. Elsevier, 2017.

[77] Laure Jason-Moller, Michael Murphy, and JoAnne Bruno. Overview of biacore systems and their applications. *Current protocols in protein science*, 45(1):19–13, 2006.

[78] Subash CB Gopinath. Biosensing applications of surface plasmon resonance-based biacore technology. *Sensors and Actuators B: Chemical*, 150(2):722–733, 2010.

[79] P Susthitha Menon, Budi Mulyanti, Nur Akmar Jamil, Chandra Wulandari, Harbi Setyo Nugroho, Gan Siew Mei, Noor Faizah Zainul Abidin, Lilik Hasanah, Roer Eka Pawinanto, and Dilla Duryha Berhanuddin. Refractive index and sensing of glucose molarities determined using au-cr k-spr at 670/785 nm wavelength. *Sains Malaysiana*, 48(6):1259–1265, 2019.

[80] Jiřı Homola, Sinclair S Yee, and Günter Gauglitz. Surface plasmon resonance sensors. *Sensors and actuators B: Chemical*, 54(1-2):3–15, 1999.

[81] Maxime Couture, Ludovic S Live, Anuj Dhawan, and Jean-Francois Masson. Eot or kretschmann configuration? comparative study of the plasmonic modes in gold nanohole arrays. *Analyst*, 137(18):4162–4170, 2012.

[82] Chandreyee Manas Das, Yan Guo, Lixing Kang, Ho-pui Ho, and Ken-Tye Yong. Investigation of plasmonic detection of human respiratory virus. *Advanced theory and simulations*, 3(7):2000074, 2020.

[83] Sabine Szunerits, Atef Shalabney, Rabah Boukherroub, and Ibrahim Abdulhalim. Dielectric coated plasmonic interfaces: their interest for sensitive sensing of analyte-ligand interactions. *Reviews in Analytical Chemistry*, 31(1):15–28, 2012.

[84] SY Wu, HP Ho, Wing Cheung Law, Chinlon Lin, and SK Kong. Highly sensitive differential phase-sensitive surface plasmon resonance biosensor based on the mach–zehnder configuration. *Optics Letters*, 29(20):2378–2380, 2004.

[85] Giorgio Quaranta, Guillaume Basset, Olivier JF Martin, and Benjamin Gallinet. Recent advances in resonant waveguide gratings. *Laser & Photonics Reviews*, 12(9):1800017, 2018.

[86] N. Lyndin. Mc grating software. https://mcgrating.com/.

[87] Zeynab Sadeghi and Hossein Shirkani. Highly sensitive mid-infrared spr biosensor for a wide range of biomolecules and biological cells based on graphene-gold grating. *Physica E: Low-dimensional Systems and Nanostructures*, 119:114005, 2020.

[88] Tahir Iqbal, Saiqa Noureen, Sumera Afsheen, Muhammad Yaqoob Khan, and Mohsin Ijaz. Rectangular and sinusoidal au-grating as plasmonic sensor: a comparative study. *Optical Materials*, 99:109530, 2020.

[89] Armin Agharazy Dormeny, Parsoua Abedini Sohi, and Mojtaba Kahrizi. Design and simulation of a refractive index sensor based on spr and lspr using gold nanostructures. *Results in Physics*, 16:102869, 2020.

[90] Jakub Dostálek, Jiří Homola, and Miroslav Miler. Rich information format surface plasmon resonance biosensor based on array of diffraction gratings. *Sensors and Actuators B: Chemical*, 107(1):154–161, 2005.

[91] Hugo Bruhier, Isabelle Verrier, Thiaka Gueye, Christelle Varenne, Amadou Ndiaye, Olivier Parriaux, Colette Veillas, Stéphanie Reynaud, Jérôme Brunet, and Yves Jourlin. Effect of roughness on surface plasmons propagation along deep and shallow metallic diffraction gratings. *Optics Letters*, 47(2):349–352, 2022.

[92] Marek Piliarik, Milan Vala, Ivo Tichỳ, and Jiří Homola. Compact and low-cost biosensor based on novel approach to spectroscopy of surface plasmons. *Biosensors and Bioelectronics*, 24(12):3430–3435, 2009.

[93] KH Lee, F Romanato, HK Kang, and CC Wong. Polarization optimization for a full sensitivity in azimuthal grating coupled surface plasmon resonance. *Sensors and Actuators B: Chemical*, 148(1):181–185, 2010.

[94] Siqi Long, Erxi Wang, Meng Wu, Huaxin Zhu, Nianxi Xu, Yueke Wang, and Jianjun Cao. Sensing absorptive fluids with backside illuminated grating coupled spr sensor fabricated by nanoimprint technology. *Sensors and Actuators A: Physical*, 337:113416, 2022.

[95] Masaru Mitsushio and Morihide Higo. A gold-deposited surface plasmon resonance-based optical fiber sensor system using various light-emitting diodes. *Analytical Sciences*, 27(3):247–247, 2011.

[96] Radan Slavık, Jiři Homola, and Jiři Čtyrokỳ. Miniaturization of fiber optic surface plasmon resonance sensor. *Sensors and Actuators B: Chemical*, 51(1-3):311–315, 1998.

[97] Sung-Hoon Hong, Chang-Kyeng Kong, Bo-Soon Kim, Min-Woo Lee, Seung-Gol Lee, Se-Geun Park, El-Hang Lee, and O Beom-Hoan. Implementation of surface plasmon resonance planar waveguide sensor system. *Microelectronic engineering*, 87(5-8):1315–1318, 2010.

[98] Radan Slavık, Jiřı Homola, Jiřı Čtyrokỳ, and Eduard Brynda. Novel spectral fiber optic sensor based on surface plasmon resonance. *Sensors and Actuators B: Chemical*, 74(1-3):106–111, 2001.

[99] Marek Piliarik, Jirı Homola, Z Manıková, and J Čtyrokỳ. Surface plasmon resonance sensor based on a single-mode polarization-maintaining optical fiber. *Sensors and Actuators B: Chemical*, 90(1-3):236–242, 2003.

[100] Kyeong-Seok Lee, Ju Myeong Son, Dae-Yong Jeong, Taek Sung Lee, and Won Mok Kim. Resolution enhancement in surface plasmon resonance sensor based on waveguide coupled mode by combining a bimetallic approach. *Sensors*, 10(12):11390–11399, 2010.

[101] Pierre Berini. Bulk and surface sensitivities of surface plasmon waveguides. *New Journal of Physics*, 10(10):105010, 2008.

[102] Hocine Bahri, Souheil Mouetsi, Abdesselam Hocini, and Hocine Ben Salah. A high sensitive sensor using mim waveguide coupled with a rectangular cavity with fano resonance. *Optical and Quantum Electronics*, 53(6):1–12, 2021.

[103] Vinod K Sharma. Ultrahigh resolution integrated optic short range surface plasmon-polariton based sensor for aqueous environment. *Engineering Research Express*, 3(1):015017, 2021.

[104] Oleksiy Krupin, Hamoudi Asiri, Chen Wang, R Niall Tait, and Pierre Berini. Biosensing using straight long-range surface plasmon waveguides. *Optics Express*, 21(1):698–709, 2013.

[105] Qing Liu and Kin Seng Chiang. Refractive-index sensor based on long-range surface plasmon mode excitation with long-period waveguide grating. *Optics express*, 17(10):7933–7942, 2009.

[106] Yuhki Yanase, Atsunori Araki, Hidenori Suzuki, Tomoko Tsutsui, Tatsuo Kimura, Keishi Okamoto, Tatsuyuki Nakatani, Takaaki Hiragun, and Michihiro Hide. Development of an

optical fiber spr sensor for living cell activation. *Biosensors and Bioelectronics*, 25(5):1244–1247, 2010.

[107] Karim Vindas, Elodie Engel, Patrick Garrigue, Thierry Livache, Stéphane Arbault, Neso Sojic, and Loic Leroy. Nano-structured optical fiber bundles for remote spr detection: A first step toward in vivo biomolecular analysis. In *2017 25th Optical Fiber Sensors Conference (OFS)*, pages 1–4. IEEE, 2017.

[108] Shin Ae Kim, Sung June Kim, Hyowon Moon, and Sang Beom Jun. In vivo optical neural recording using fiber-based surface plasmon resonance. *Optics letters*, 37(4):614–616, 2012.

[109] Yongkang Gao, Qiaoqiang Gan, Zheming Xin, Xuanhong Cheng, and Filbert J Bartoli. Plasmonic mach–zehnder interferometer for ultrasensitive on-chip biosensing. *ACS nano*, 5(12):9836–9844, 2011.

[110] Hui Fan and Pierre Berini. Bulk sensing using a long-range surface-plasmon dual-output mach–zehnder interferometer. *Journal of Lightwave Technology*, 34(11):2631–2638, 2016.

[111] Melissa J Goodwin, Geert AJ Besselink, Floris Falke, Arnoud S Everhardt, Jeroen JLM Cornelissen, and Jurriaan Huskens. Highly sensitive protein detection by asymmetric mach–zehnder interferometry for biosensing applications. *ACS Applied Bio Materials*, 3(7):4566–4572, 2020.

[112] Xu Sun, Lars Thylén, and Lech Wosinski. Hollow hybrid plasmonic mach–zehnder sensor. *Optics letters*, 42(4):807–810, 2017.

[113] AV Kabashin and PI Nikitin. Surface plasmon resonance interferometer for bio-and chemical-sensors. *Optics communications*, 150(1-6):5–8, 1998.

[114] Muhammad Kashif, Mohd Hadri Hafiz Mokhtar, Nur Hidayah Azeman, Fazida Hanim Hashim, Norhana Arsad, Abdulfatah AG Abushagur, and Ahmad Ashrif A Bakar. Phase-interrogated surface plasmon resonance sensor based on laser feedback interferometry. *Optics and Lasers in Engineering*, 141:106564, 2021.

[115] Muhammad Kashif, A Ashrif A Bakar, and Fazida Hanim Hashim. Analysing surface plasmon resonance phase sensor based on mach-zehnder interferometer technique using glycerin. *Optics Communications*, 380:419–424, 2016.

[116] Muhammad Kashif, Ahmad Ashrif A Bakar, Norhana Arsad, and Sahbudin Shaari. Development of phase detection schemes based on surface plasmon resonance using interferometry. *Sensors*, 14(9):15914–15938, 2014.

[117] Qing Liu, Xiaoguang Tu, Kyung Woo Kim, Jack Sheng Kee, Yong Shin, Kyungsup Han, Yong-Jin Yoon, Guo-Qiang Lo, and Mi Kyoung Park. Highly sensitive mach–zehnder interferometer biosensor based on silicon nitride slot waveguide. *Sensors and Actuators B: Chemical*, 188:681–688, 2013.

[118] Hui Fan and Pierre Berini. Bulk sensing using a long-range surface-plasmon triple-output mach–zehnder interferometer. *JOSA B*, 33(6):1068–1074, 2016.

[119] Borja Sepúlveda, J Sanchez Del Rio, M Moreno, Francisco J Blanco, K Mayora, Carlos Domínguez, and Laura M Lechuga. Optical biosensor microsystems based on the integration of highly sensitive mach–zehnder interferometer devices. *Journal of Optics A: Pure and Applied Optics*, 8(7):S561, 2006.

[120] Francisco Prieto, Borja Sepúlveda, A Calle, Andreu Llobera, C Domınguez, and Laura M Lechuga. Integrated mach–zehnder interferometer based on arrow structures for biosensor applications. *Sensors and actuators B: Chemical*, 92(1-2):151–158, 2003.

[121] Wei Ru Wong, Oleksiy Krupin, Shamala Devi Sekaran, Faisal Rafiq Mahamd Adikan, and Pierre Berini. Serological diagnosis of dengue infection in blood plasma using long-range surface plasmon waveguides. *Analytical chemistry*, 86(3):1735–1743, 2014.

[122] Francisco Prieto, Borja Sepúlveda, A Calle, Andreu Llobera, Carlos Domínguez, Antonio Abad, A Montoya, and Laura M Lechuga. An integrated optical interferometric nanodevice based on silicon technology for biosensor applications. *Nanotechnology*, 14(8):907, 2003.

[123] Florian Vogelbacher, Tim Kothe, Paul Muellner, Eva Melnik, Martin Sagmeister, Jochen Kraft, and Rainer Hainberger. Waveguide mach-zehnder biosensor with laser diode pumped integrated single-mode silicon nitride organic hybrid solid-state laser. *Biosensors and Bioelectronics*, 197:113816, 2022.

[124] Tatevik Chalyan, Romain Guider, Laura Pasquardini, Manuela Zanetti, Floris Falke, Erik Schreuder, Rene G Heideman, Cecilia Pederzolli, and Lorenzo Pavesi. Asymmetric mach–zehnder interferometer based biosensors for aflatoxin m1 detection. *Biosensors*, 6(1):1, 2016.

[125] Qing Liu, Yong Shin, Jack Sheng Kee, Kyoung Woo Kim, Siti Rafeah Mohamed Rafei, Agampodi Promoda Perera, Xiaoguang Tu, Guo-Qiang Lo, Estelle Ricci, Marc Colombel, et al. Mach–zehnder interferometer (mzi) point-of-care system for rapid multiplexed detection of micrornas in human urine specimens. *Biosensors and Bioelectronics*, 71:365–372, 2015.

[126] Geert Besselink, Anke Schütz-Trilling, Janneke Veerbeek, Michelle Verbruggen, Adriaan van der Meer, Rens Schonenberg, Henk Dam, Kevin Evers, Ernst Lindhout, Anja Garritsen, et al. Asymmetric mach–zehnder interferometric biosensing for quantitative and sensitive multiplex detection of anti-sars-cov-2 antibodies in human plasma. *Biosensors*, 12(8):553, 2022.

[127] Michailia Angelopoulou, Dimitra Kourti, Konstantinos Misiakos, Anastasios Economou, Panagiota Petrou, and Sotirios Kakabakos. Mach-zehnder interferometric immunosensor for detection of aflatoxin m1 in milk, chocolate milk, and yogurt. *Biosensors*, 13(6):592, 2023.

[128] Adrian Fernandez-Gavela, Sonia Herranz, Blanca Chocarro, Floris Falke, Erik Schreuder, Henk Leeuwis, René G Heideman, and Laura M Lechuga. Full integration of photonic nanoimmunosensors in portable platforms for on-line monitoring of ocean pollutants. *Sensors and Actuators B: Chemical*, 297:126758, 2019.

[129] Daphne Duval, Johann Osmond, Stefania Dante, Carlos Dominguez, and Laura M Lechuga. Grating couplers integrated on mach-zehnder interferometric biosensors operating in the visible range. *IEEE Photonics Journal*, 5(2):3700108–3700108, 2013.

[130] Kouki Ichihashi, Yasuhiro Mizutani, and Tetsuo Iwata. Enhancement of the sensitivity of a diffraction-grating-based surface plasmon resonance sensor utilizing the first-and negative-second-order diffracted lights. *Optical Review*, 21:728–731, 2014.

[131] Matteo Altissimo. E-beam lithography for micro-/nanofabrication. *Biomicrofluidics*, 4(2):026503, 2010.

[132] Yifang Chen. Nanofabrication by electron beam lithography and its applications: A review. *Microelectronic Engineering*, 135:57–72, 2015.

[133] Hasan Kurt, Parsa Pishva, Zeki Semih Pehlivan, Elif Gül Arsoy, Qandeel Saleem, Mustafa Kemal Bayazıt, and Meral Yüce. Nanoplasmonic biosensors: Theory, structure, design, and review of recent applications. *Analytica Chimica Acta*, 1185:338842, 2021.

[134] Gerardo A López-Muñoz, M-Carmen Estevez, E Cristina Peláez-Gutierrez, Antoni Homs-Corbera, M Carmen García-Hernandez, J Ignacio Imbaud, and Laura M Lechuga. A label-free nanostructured plasmonic biosensor based on blu-ray discs with integrated microfluidics for sensitive biodetection. *Biosensors and Bioelectronics*, 96:260–267, 2017.

[135] Atefeh Chahkoutahi, Farzin Emami, and Esmat Rafiee. Sensitive hemoglobin concentration sensor based on graphene-plasmonic nano-structures. *Plasmonics*, pages 1–9, 2022.

[136] M Bianco, A Sonato, A De Girolamo, M Pascale, F Romanato, R Rinaldi, and V Arima. An aptamer-based spr-polarization platform for high sensitive ota detection. *Sensors and actuators B: chemical*, 241:314–320, 2017.

[137] Rakesh Singh Moirangthem, Mohammad Tariq Yaseen, Yia-Chung Chang, and Pei-Kuen Wei. Plasmonic biosensing with nanoimprint binary grating using ellipsometry. In *Biosensing and Nanomedicine IV*, volume 8099, pages 85–90. SPIE, 2011.

[138] Yanqiu Dai, Huimei Xu, Haoyu Wang, Yonghua Lu, and Pei Wang. Experimental demonstration of high sensitivity for silver rectangular grating-coupled surface plasmon resonance (spr) sensing. *Optics Communications*, 416:66–70, 2018.

[139] Jianjun Cao, Yuan Sun, Yan Kong, and Weiying Qian. The sensitivity of grating-based spr sensors with wavelength interrogation. *Sensors*, 19(2):405, 2019.

[140] Siqi Long, Jianjun Cao, Yueke Wang, Shumei Gao, Nianxi Xu, Jinsong Gao, and Wenjie Wan. Grating coupled spr sensors using off the shelf compact discs and sensitivity dependence on grating period. *Sensors and Actuators Reports*, 2(1):100016, 2020.

[141] RC Mc Phedran and D Maystre. Theoretical study of the diffraction anomalies of holographic gratings. *Nouvelle Revue d'Optique*, 5(4):241, 1974.

[142] Siqi Long, Jianjun Cao, Shannan Geng, Nianxi Xu, Weiying Qian, and Shumei Gao. Optimization of plasmonic sensors based on sinusoidal and rectangular gratings. *Optics Communications*, 476:126310, 2020.

[143] V Sukhotskiy, NC Cady, E Chou, IVAK Reddy, and EP Furlani. Numerical modelling of a sinusoidal grating-based surface plasmon coupled emission biosensor. *TechConnect Briefs*, 4:205–208, 2018.

[144] Uwe Bog, Klaus Huska, Frieder Maerkle, Alexander Nesterov-Mueller, Uli Lemmer, and Timo Mappes. Design of plasmonic grating structures towards optimum signal discrimination for biosensing applications. *Optics express*, 20(10):11357–11369, 2012.

[145] Changkui Hu and Deming Liu. High-performance grating coupled surface plasmon resonance sensor based on al-au bimetallic layer. *Modern Applied Science*, 4(6):8, 2010.

[146] Jean Sauvage-Vincent, Yves Jourlin, Valéry Petiton, AV Tishchenko, Isabelle Verrier, and Olivier Parriaux. Low-loss plasmon-triggered switching between reflected free-space diffraction orders. *Optics express*, 22(11):13314–13321, 2014.

[147] Alexandre V Tishchenko, Olivier M Parriaux, and Dieter Neuschafer. Waveguide grating coupling of 2d focused beam under normal incidence: a phenomenological approach. In *Optical Design and Engineering*, volume 5249, pages 546–556. SPIE, 2004.

[148] G Voirin, P Sixt, O Parriaux, and Li Yan. Digitized dual-frequency coupling grating for waveguide displacement interferometry. In *Conference on Lasers and Electro-Optics Europe*, pages 339–339. IEEE.

[149] Emilie Laffont, Nicolas Crespo-Monteiro, Arnaud Valour, Pierre Berini, and Yves Jourlin. Differential sensing with replicated plasmonic gratings interrogated in the optical switch configuration. *Sensors*, 23(3):1188, 2023.

[150] Alexandre V Tishchenko and Olivier Parriaux. Coupled-mode analysis of the low-loss plasmon-triggered switching between the 0 th and-1 st orders of a metal grating. *IEEE Photonics Journal*, 7(4):1–9, 2015.

[151] Cheng Lu and RH Lipson. Interference lithography: a powerful tool for fabricating periodic structures. *Laser & Photonics Reviews*, 4(4):568–580, 2010.

[152] AA Ushkov, Isabelle Verrier, T Kampfe, and Yves Jourlin. Subwavelength diffraction gratings with macroscopic moiré patterns generated via laser interference lithography. *Optics Express*, 28(11):16453–16468, 2020.

[153] Ratish Rao Nagaraj Rao, Florian Bienert, Michael Moeller, Danish Bashir, Alina Hamri, Frederic Celle, Emilie Gamet, Marwan Abdou Ahmed, and Yves Jourlin. Quantitative investigation on a period variation reduction method for the fabrication of large-area gratings using two-spherical-beam laser interference lithography. *Optics Express*, 31(1):371–380, 2023.

[154] Ren-Haw Chen and Chao-Min Cheng. Spin coating properties of su-8 thick-layer photoresist. In *Advances in Resist Technology and Processing XVIII*, volume 4345, pages 494–501. SPIE, 2001.

[155] Andrés Fabián Lasagni. Laser interference patterning methods: Possibilities for high-throughput fabrication of periodic surface patterns. *Advanced Optical Technologies*, 6(3-4):265–275, 2017.

[156] C. Anderson P. Klapetek, D. Nečas. One-dimensional roughness parameters - chapter 4. data processing and analysis. http://gwyddion.net/documentation/user-guide-en/roughness-iso.html.

[157] J Chandezon, G Raoult, and D Maystre. A new theoretical method for diffraction gratings and its numerical application. *Journal of Optics*, 11(4):235, 1980.

[158] Lifeng Li, Jean Chandezon, Gérard Granet, and Jean-Pierre Plumey. Rigorous and efficient grating-analysis method made easy for optical engineers. *Applied Optics*, 38(2):304–313, 1999.

[159] NP Van Der Aa. Diffraction grating theory with rcwa or the c method. In *Progress in Industrial Mathematics at ECMI 2004*, pages 99–103. Springer, 2006.

[160] TW Preist, NPK Cotter, and JR Sambles. Periodic multilayer gratings of arbitrary shape. *JOSA A*, 12(8):1740–1748, 1995.

[161] Shu-Cheng Lo, En-Hung Lin, Kuang-Li Lee, Ting-Tung Liang, Jen-Chang Liu, Pei-Kuen Wei, and Wan-Shao Tsai. A concave blazed-grating-based smartphone spectrometer for multichannel sensing. *IEEE Sensors Journal*, 19(23):11134–11141, 2019.

[162] Sheng-Hann Wang, Shu-Cheng Lo, Yung-Ju Tung, Chia-Wen Kuo, Yi-Hsin Tai, Shu-Yi Hsieh, Kuang-Li Lee, Shune-Rung Hsiao, Jenn-Feng Sheen, Ju-Chun Hsu, et al. Multichannel nanoplasmonic platform for imidacloprid and fipronil residues rapid screen detection. *Biosensors and Bioelectronics*, 170:112677, 2020.

[163] J Chandezon, A Gavaix, O Parriaux, and C Kneale. Application of heisenberg uncertainty relation for the optimal modeling of surface diffraction. *JOSA A*, 36(4):594–605, 2019.

[164] Y Sarov, S Sainov, I Kostic, V Sarova, and S Mitkov. Automatic vis-near ir laser refractometer. *Review of Scientific Instruments*, 75(10):3342–3344, 2004.

[165] Chia-Chen Chang. Recent advancements in aptamer-based surface plasmon resonance biosensing strategies. *Biosensors*, 11(7):233, 2021.

[166] Sreyashi Das, Ram Devireddy, and Manas Ranjan Gartia. Surface plasmon resonance (spr) sensor for cancer biomarker detection. *Biosensors*, 13(3):396, 2023.

[167] Amal Kasry, Andreas Nicol, and Wolfgang Knoll. Grating-coupled surface-plasmon fluorescence dna sensor. *Applied Physics B*, 127(5):68, 2021.

[168] N Scott Lynn, Hana Šípová, Pavel Adam, and Jiří Homola. Enhancement of affinity-based biosensors: effect of sensing chamber geometry on sensitivity. *Lab on a Chip*, 13(7):1413–1421, 2013.

[169] Shijie Deng, Peng Wang, Lili Ding, and Xinglong Yu. A curved top-wall flow cell for improvement of response consistency in surface plasmon resonance array detection. *Sensors and Actuators A: Physical*, 218:41–48, 2014.

[170] Maryam Khodami and Pierre Berini. Biomolecular kinetics analysis using long-range surface plasmon waveguides. *Sensors and Actuators B: Chemical*, 243:114–120, 2017.

[171] O Krupin, C Wang, and P Berini. Detection of leukemia markers using long-range surface plasmon waveguides functionalized with protein g. *Lab on a Chip*, 15(21):4156–4165, 2015.

[172] Wei Ru Wong, Shamala Devi Sekaran, Faisal Rafiq Mahamd Adikan, and Pierre Berini. Detection of dengue ns1 antigen using long-range surface plasmon waveguides. *Biosensors and Bioelectronics*, 78:132–139, 2016.

[173] Maryam Khodami and Pierre Berini. Low detection limits using sandwich and inhibition assays on long-range surface plasmon waveguide biosensors. *Sensors and Actuators B: Chemical*, 273:1156–1161, 2018.

[174] Olivier Parriaux. Guided-mode triggered switching between te orders of a metal-based grating-waveguide. *Journal of the European Optical Society-Rapid publications*, 10, 2015.

[175] Jean Sauvage-Vincent, S Tonchev, C Veillas, S Reynaud, and Y Jourlin. Optical security device for document protection using plasmon resonant transmission through a thin corrugated metallic film embedded in a plastic foil. *Journal of the European Optical Society-Rapid publications*, 8, 2013.

[176] Srijit Nair, Juan Gomez-Cruz, Ángel Manjarrez-Hernandez, Gabriel Ascanio, Ribal Georges Sabat, and Carlos Escobedo. Selective uropathogenic e. coli detection using crossed surface-relief gratings. *Sensors*, 18(11):3634, 2018.

[177] Emilie Laffont, Nicolas N Crespo-Monteiro, Pierre Berini, and Yves Jourlin. Development of a new plasmonic transducer for the detection of biological species. In *Optical Sensing and Detection VII*, volume 12139, pages 97–105. SPIE, 2022.